VARIABLE CROSS-SECTION FLOWS IN

POLYMER AND COMPOSITES PROCESSING

UNIVERSITY OF THESSALY

DEPARTMENT OF MECHANICAL ENGINEERING

Variable Cross-Section Flows in Polymer and Composites Processing

Nickolas D. Polychronopoulos

M. Sc., Mechanical Engineering

Department of Mechanical Engineering

University of Thessaly

A Dissertation Submitted to the School of Graduate Studies

In Partial Fulfillment of the Requirements for the Degree

Doctor of Philosophy

February 2016

The approval of the current dissertation by the Department of Mechanical Engineering of the University of Thessaly does not imply acceptance of the author's opinions (Law 5343/32 number 202 paragraph 2). Also, the views and opinions expressed herein do not necessarily reflect those of the European Commission.

Certified by the members of the Dissertation Committee:

1st member   Assoc. Prof. Thanasis D. Papathanasiou
(Supervisor)   Associate Professor in the Department of Mechanical Engineering
                    University of Thessaly

2nd member   Prof. Savvas G. Hatzikiriakos
                    Professor in the Department of Chemical and Biological Engineering
                    The University of British Columbia

3rd member   Prof. Nikolaos Pelekasis
                    Professor in the Department of Mechanical Engineering
                    University of Thessaly

4th member   Prof. Evan Mitsoulis
                    Professor in the School of Mining and Metallurgical Engineering
                    National Technical University of Athens

5th member   Prof. Vasilis Bontozoglou
                    Professor in the Department of Mechanical Engineering
                    University of Thessaly

6th member   Prof. Panagiotis Tsiakaras
                    Professor in the Department of Mechanical Engineering
                    University of Thessaly

7th member   Prof. Spyros Karamanos
                    Professor in the Department of Mechanical Engineering
                    University of Thessaly

ii

ACKNOWLEDGEMENTS

I would like to express my gratitude to my supervisor, Dr. Thanasis D. Papathanasiou for his mentorship, guidance, criticism and continuous support during my research in University of Thessaly. The boundless freedom Dr. Papathanasiou gave me for this thesis is tremendously appreciated, enriching my knowledge in both practical and theoretical sense. The limitless advice of Dr. Papathanasiou will have a profound influence in my career.

I am also grateful to my PhD committee members, Dr. Nikos Pelekasis and Dr. Savvas G. Hatzikiriakos (University of British Columbia), for their valuable advice and fruitful discussions during the research for this thesis.

Very special thanks go to Dr. Ioannis E. Sarris for his significant help in understanding the power of computational fluid mechanics.

I would like to thank my uncle, Professor Emeritus John Vlachopoulos, for his inspiring ideas and his valuable advice regarding how industry and academia work.

I am also grateful for the financial support from the Department of Mechanical Engineering.

I would also like to thank my family and all of my friends for their continuous support during this difficult task.

Last, but not least, I would like to thank Despina, for her patience and understanding that provided me the necessary peace and focus to carry out my work.

Ροές Μεταβλητής Διατομής κατά τη Μορφοποίηση Πολυμερών και Σύνθετων

Νικόλας Δ. Πολυχρονόπουλος
Πανεπιστήμιο Θεσσαλίας, Φεβρουάριος 2016
Επιβλέπων Καθηγητής: Δρ. Τ. Παπαθανασίου

Περίληψη

Ο σκοπός της παρούσας διατριβής είναι να επιλύσει μια σειρά προβλημάτων που συναντώνται στη παραγωγή φύλλων, υμενίων και ταινιών τα οποία κατασκευάζονται από πολυμερή και τα σύνθετα αυτών. Πλήρως 3D αριθμητικές προσομοιώσεις της κυλίνδρωσης (calendering) δείχνουν ότι η πλευρική εξάπλωση του φύλλου, που διέρχεται μεταξύ των δυο αντιπεριστρεφόμενων κυλίνδρων, επηρεάζεται από το πλάτος και το πάχος του φύλλου στην περιοχή τροφοδοσίας καθώς επίσης και από την ταχύτητα τροφοδοσίας. Τα αποτελέσματα αναδεικνύουν ότι η πλευρική εξάπλωση του φύλλου επιτυγχάνεται μέσω μιας σπειροειδούς κίνησης του ρευστού. Η μελέτη αυτού του ροϊκού πεδίου αποκαλύπτει μια αξιοσημείωτη αναδιάταξη του υλικού από την περιοχή τροφοδοσίας προς τις πλευρές. Για την περιγραφή της διαδικασίας χύτευσης φύλλου (film casting) ακολουθήθηκε αριθμητική επίλυση των εξισώσεων διατήρησης μάζας και ορμής χρησιμοποιώντας το Phan Thien-Tanner γραμμικό μοντέλο, ως καταστατική εξίσωση, που περιγράφει την ιξωδοελαστική συμπεριφορά του ρευστού. Τα αποτελέσματα αποδεικνύουν ότι η μέγιστη διόγκωση (maximum swelling) του υλικού στην έξοδο της κεφαλής μειώνεται ραγδαία με την αύξηση του λόγου τάνυσης (draw ratio) του φύλλου. Για την κατανόηση της διαδικασίας εκβολής με έλξη υποβοηθούμενη από κυλίνδρους (pin-assisted pultrusion), τα δυναμικά φαινόμενα εμποτισμού ενός πορώδους υποστρώματος με ρευστό διερευνήθηκαν υπολογιστικά. Προσδιορίστηκε ότι το βάθος εμποτισμού μιας σύνθετης διαπερατής ταινίας/ιστού που έλκεται πάνω από έναν μη περιστρεφόμενο κύλινδρο, προκαλείται λόγω ανάπτυξης πίεσης και επηρεάζεται από έναν μεγάλο αριθμό παραμέτρων που διέπουν τη διεργασία και το υλικό (π.χ. ακτίνα κυλίνδρου, ταχύτητα έλξης, ιξώδες ρευστού και διαπερατότητα της πορώδους ταινίας, ιστού). Μια απλοποιημένη ανάλυση κλίμακας, βασισμένη στη ροή του ρευστού διαμέσου του διαπερατού μέσου και στη ροή του διάκενου, υποδεικνύει ότι όλες οι σημαντικές

iv

παράμετροι της διεργασίας μπορούν να εκφραστούν μέσω ενός αδιάστατου αριθμού, ο οποίος εξαρτάται εκθετικά από το βάθος εμποτισμού. Χρησιμοποιώντας αυτή την εκθετική εξάρτηση για την μελέτη μιας διαδοχικής συστοιχίας κυλίνδρων, λήφθηκαν αποτελέσματα τα οποία βρίσκονται σε καλή συμφωνία με προγενέστερα πειραματικά αποτελέσματα. Υποκινούμενοι από την παραπάνω ανάλυση του βάθους εμποτισμού, ακολουθήθηκε μια γενικευμένη μελέτη για την περιγραφή και ποσοτικοποίηση του βάθους εμποτισμού που λαμβάνει χώρα σε ένα διαπερατό και παραμορφώσιμο υπόστρωμα υπό μορφής ιστού, που κινείται πάνω από ένα άκαμπτο, στερεό και μη περιστρεφόμενο κύλινδρο. Τα αποτελέσματα υποδεικνύουν ότι το υπόστρωμα έχει την τάση να κινείται μακριά από τον κύλινδρο καθώς τον πλησιάζει και προσπαθεί να έρθει πιο κοντά σε αυτόν καθώς απομακρύνεται. Αυτή η συμπεριφορά προκαλεί ένα μέγιστο βάθος εμποτισμού σε συγκεκριμένες καταστάσεις παραμόρφωσης και διαπερατότητας του πορώδους υποστρώματος. Τα αποτελέσματα που λαμβάνονται είναι χρήσιμα για σχεδιασμό και βελτιστοποίηση διεργασιών παραγωγής λεπτών ταινιών και ιστών καθώς και για άλλες συσχετιζόμενες διεργασίας όπως επικάλυψης (coating), κύλισης (rolling) και τύπωσης (printing).

Variable Cross-Section Flows in Polymer and Composites Processing

Nickolas Polychronopoulos
University of Thessaly, January 2016
Supervisor: Dr. T.D. Papathanasiou

Thesis Abstract

The present thesis is aimed at elucidating a number of problems encountered in the production of sheet, film and tape made from polymers and their composites. These problems share the common feature of flow in a variable cross-section. Fully 3D numerical simulation of calendering revealed that the spreading of the sheet, passing through two counter rotating rolls, is influenced by the entrance width and thickness of the sheet at the feed section as well as the sheet feeding speed. The lateral spreading of the sheet is accomplished via a spiral motion of the fluid towards the sides. Examination of this flow field reveals a remarkable material rearrangement from the feeding section to the exit. For the film casting process a numerical solution of the conservation of mass and momentum equations using the linear Phan Thien-Tanner (PTT) constitutive equation was performed. It was determined that the maximum swelling at the die exit due to viscoelasticity, rapidly decreases as the drawing speed increases. For understanding the pin-assisted pultrusion process, the fluid penetration dynamics of a porous substrate was analysed computationally. It was determined that the fluid penetration depth of a permeable composite tape/web pulled over a single non-rotating pin (cylinder) is pressure induced and influenced by a large number of material and process parameters (e.g. pin radius, pulling speed, fluid viscosity and tape/web permeability). A simple scaling analysis based on the fluid flow through the permeable tape and through the gap, indicates that all the important parameters of the process may be expressed in a single dimensionless number which exhibits a power-law type dependence on the penetration depth. Using this dependence for studying a sequential cylinder arrangement, results were obtained, which are in good agreement when compared with the limited number of earlier experimental studies. Motivated by the fluid penetration results for the pin-assisted pultrusion process, a

generalized study was carried out, for the description of the fluid penetration depth to a permeable and deformable web moving past a rigid stationary cylinder. The results indicate that the web has the tendency to move away from the cylinder as it approaches it and comes closer as it leaves. This behavior leads to a maximum penetration depth under specific deformability and permeability conditions. These results are useful for engineering design and optimization purposes for tape or web production and for other related processes such as coating, rolling and printing.

Contents

List of Tables

List of Figures

xiii

parameters for the theoretical predictions of Eq. 5.8: $K=10^{-9}$ m^2, $T=20$ N, $W=10$ mm and $\delta=500$ μm.

Figure-5.13. Infiltration degree D_f as a function of the contact time ($t=R/V$) of the porous substrate with the pin. Symbols are experimental results reproduced from Bates and Zou [9]. Continuous line corresponds to predictions by Eq. 5.8 for $N=2$ and dashed line for $N=7$. Pulling speed range $V=0.035$ m/s~0.5 m/s and $R=2$ mm~7 mm. Assumed values for the model (Eq. 5.8): $K=10^{-9}$ m^2, $T=20$ N, $\mu=100$ Pa·s and $\delta=500$ μm.

Figure-5.14. Infiltration degree D_f as a function of the pin radius for two pulling speeds V and different number of pins N. Symbols are experimental results reproduced from Bates and Zou [9] for $N=3$. Continuous lines correspond to predictions by Eq. 5.8 for $N=3$ and dashed lines for $N=9$. Assumed values for the model (Eq. 5.8): $K=10^{-9}$ m^2, $T=20$ N, $\mu=100$ Pa·s and $\delta=500$ μm.

Figure-5.15. Infiltration degree D_f as a function of the pulling speed V for different number of pins. Symbols are experimental results reproduced from Bates and Zou [9] for $R=5$ mm. Lines correspond to predictions by Eq. 5.8 for different numbers of pins. Assumed values for the model (Eq. 5.8): $K=10^{-9}$ m^2, $T=20$ N, $\mu=100$ Pa·s and $\delta=500$ μm.

Figure-6.1. Schematic representation of the problem geometry prior to the web deformation or of the problem corresponding to a rigid web. The web with thickness H, Young modulus E and permeability K moves to the right with velocity V in close proximity h_o with a rigid solid stationary cylinder of radius R. The fluid of viscosity μ penetrates the web with penetration velocity v (denoted with the small vertical arrows). Figure not to scale.

Figure-6.2. Schematic representation (near the region of minimum gap h_o) of the variation of the web/cylinder gap h(x). H is the web thickness and E and K its Young modulus and permeability respectively. The horizontal broken line corresponds to the web's surface in undeformed state (or rigid web, $E\rightarrow\infty$). The fluid of viscosity μ penetrates the web with penetration velocity v (denoted with the small vertical arrows). Figure not to scale.

Figure-6.3. Schematic representation (near the region of minimum gap h_o) of the fluid penetration depth $L(x)$ in the flexible web. The final penetration depth L_f corresponds to the accomplished depth of the penetrated fluid at some location away from the minimum gap h_o as the web moves to the right and leaves the cylinder behind. E Young modulus and K the permeability of the web.

Figure-6.4. (a) Dimensionless pressure and (b) dimensionless gap for different values of Ne. $S=0.01$, $\hat{K}=0$. The impermeable flexible web is assumed to move with velocity V to the right.

Figure-6.5. Dimensionless lift force per unit width $\hat{F}$ as a function of Ne for different S values for a non-permeable web ($\hat{K}=0$).

Chapter 1

Overview

1.1 Introduction

Mankind, since the beginning of history, has used natural polymeric materials such as leather and wool. Production of synthetic polymers became possible only after the development of rubber technology in the 1800s, with celluloid being practically the first synthetic polymer material invented by John Wesley Hyatt in 1869, from cellulose nitrate and camphor [1]. The rapid growth of polymer industry started just before the Second World War with the development of various synthetic polymers such as polyethylene (PE), polypropylene (PP), polyvinyl chrolide (PVC), acrylics, polyurethane and other polymers, aiming towards replacing conventional materials such as metals, wood, paper and natural fibers. Shortly thereafter and due to the constant search of materials able to combine low weight and sustain high strengths and stiffness, composite materials emerged. Strictly speaking, a composite consists of two or more types of materials the combination of which yields a product with unique properties. Polymer composites or fiber reinforced plastics, in a more popular usage, are a combination of a synthetic polymer and solid continuous or non-continuous inclusions (reinforcements). The applicability of polymers and polymer composites is enormous, ranging from household, to electronics, to automotive, to aerospace and to the health industry. The final product may have the form of sheets, films, textiles, tubes, pipes, profiles, composite tapes/webs and many more other and far more complex shapes.

Polymer processing in its generality, deals with the conversion of raw polymeric materials into "value added" finished products, involving not only shaping but also compounding and chemical reactions [2]. Of course, this can be extended to include also the processing of polymer composites. Several processes exist for the processing of polymer and polymer composites: extrusion, injection molding, blow molding, calendering, roll coating, film casting, fiber spinning, compression molding, rotational molding, pultrusion, tape lay-up, autoclave processing, liquid composite molding, and filament winding. A common characteristic in these processes is that the polymer is processed in a molten or liquid state, thus it *flows*. In these processes the flowing material

will undergo several variations in its cross-section. Generally, the cross-section may vary due to either the channel geometry (depth and width) of the parts comprising the production lines or due to the polymer partially elastic nature, which is exhibited by the higher cross-section area (swelling) of the material right after it emerges from a channel.

1.2 Polymers

1.2.1 Basic Classification

Synthetic polymers may be classified into two main categories. Thermoplastics (by far the largest volume with nearly 300 million tons produced annually) can be melted by heating, shaped by flowing through dies or filling for molds, and subsequently solidified into final useful products. In their molten state they are highly viscous materials and their viscosity can be more than a million times higher than that of water, under usual processing conditions. This type of polymers can be either amorphous (without regular structure) or semicrystalline (amorphous with embedded regular substructures). Major types are polyethylene (PE), polypropylene (PP), polyvinyl chloride (PVC), polycarbonate (PC), polymethyl methacrylate (PMMA) and polystyrene (PS). Thermosets can be hardened by applying heat or pressure, due to cross-linking, i.e. the creation of permanent three-dimensional networks. They cannot be softened by heating for reprocessing and they are roughly 50 to 500 times more viscous than water. Most common types of thermosets are bakelite, epoxies and many polyurethanes. Polymers are seldom processed in their own. They are often blended or compounded with other materials to produce pellets, powders or flakes to be used in subsequent processing operations [3]. The utilized compounds may involve fillers, colorants, other polymers, flame retardants, reinforcements, stabilizers and various processing aids. The compounded polymers are usually referred to as plastics.

1.2.2 Viscosity and Elasticity

Fluids are characterized by a viscosity, which is a quantitative measure of resistance to flow. In Newtonian fluids the viscosity is independent of the shear rate and depends only on temperature and pressure. In polymer solutions and melts the viscosity depends also on shear rate. One remarkable property of polymeric liquids is their *shear-thinning* behavior which is also known as *pseudo-plastic* behavior. As the shear rate increases the viscosity decreases due to molecular alignments and disentanglements of the polymer chains. The higher the shear rate, the easier is for the molten polymer to flow through

2

channels of the process equipment. The most frequently used models to express the shear-thinning behavior of the viscosity are: (i) power-law model, (ii) Cross model and (iii) Carreau-Yasuda model [4]. These models differ in the number of the parameters used to fit measured viscosity versus shear rate data. Temperature-viscosity dependence obeys the Arrhenius relation which can be simplified into a simple exponential form, that applies over a shorter temperature range but it is good enough for most extrusion calculations and simulations. Pressure-viscosity dependence may also follow an exponential dependence. It is usually not taken into account in extrusion, but it is necessary for calculations and simulations in injection molding.

Aside from their viscous behavior described above, molten polymers and polymer solutions behave as *elastic* materials, which means that they can exhibit a response resembling that of a rubber-like solid. Due to this dual nature, polymeric liquids are frequently referred to as *viscoelastic*. As Bird et al. [5] put it: "a fluid that is macromolecular is really quite weird, in particular the big normal stresses the fluid possesses give rise to effects quite spectacular". Among these effects is worth mentioning: (i) the rod-climbing effect observed by Weissenberg [6], (ii) the extrudate or die swell phenomenon [7] where the dimensions of the emerging melt from a shaping die are higher than the dimensions of the die and (iii) large vortex phenomena even in very low Reynolds number flows (creeping) [8].

The level of elasticity in a flow system is usually determined by one of the following three dimensionless numbers, which under certain conditions can de identical according to Denn [9]:

(i)   Deborah number (*De*), defined as *De=material time/process time*. The characteristic process time is usually chosen as the inverse of the wall shear rate $\dot{\gamma}_w$ in channel flows.

(ii)   Weissenberg number (*Wi*), defined as: $Wi = \lambda\dot{\gamma}_w$ where λ is the characteristic material time and $\dot{\gamma}_w$ the shear rate at the wall. In some publications, $\dot{\gamma}_w$ is defined simply as velocity scale divided by a length scale. The velocity scale is usually the flow average velocity and the length scale is a diameter or gap.

(iii) Stress ratio (S_R), defined as $S_R=(\tau_{11}-\tau_{22})/2\tau_{12}$, where τ is the stress tensor. Newtonian fluids are uniformly compressed in the three directions *1*, *2* and *3*. Viscoelastic fluids like polymer solutions and melts are extended in the flow direction *11*, and $\tau_{11}-\tau_{22}$ has a positive non-zero value.

3

1.2.3   Constitutive Equations

In rheology, the science of deformation and flow of matter, one of the general goals is to obtain appropriate relations between stresses and strains. These relations are referred to as *constitutive equations*. In purely viscous fluids the constitutive equation is relatively simple and the stresses are linearly related to the strain rates through a viscosity which may also be a function of the strain rates. Such a relation is frequently referred to as the Generalized Newtonian Fluid (GNF) in the rheological literature. For the description of viscoelastic behavior the constitutive equation is more complicated by far. The Maxwell viscoelastic model [4] is perhaps the simplest form of constitutive equation that expresses a combination of an elastic solid and a Newtonian fluid. An extension to this model is the White-Metzner model which allows shear-thinning. A more useful expression is the Phan Thien-Tanner (PTT) viscoelastic model [10], which is used in Chapter 3. More sophisticated models include the K-BKZ model inspired by the rubber elasticity theory [11] and the POM-POM model [12,13] inspired by the DeGennes reptation theory [14].

1.3   Polymer Composites

Polymer or plastics composites have been in use for a few decades now, offering advantages over other materials mainly for high performance and lightweight applications. The individual parts comprising a polymer composite are polymer resin, which is also called the matrix phase, and a solid reinforcing phase. The properties of plastics themselves can be excellent, but generally they are not suited for the construction of large, heavily loaded constructions or products. Adding reinforcement results in a composite material with superior properties compared to the properties of the individual reinforcement and the plastic.

1.3.1   Matrix Phase

The purpose of the polymer matrix is to integrally bind together the constituents of the reinforcing phase, give a nice surface appearance and provide good overall durability to the final product. The matrix phase can be either a thermoplastic or a thermoset polymer. Thermosets, due to their low viscosity they can readily fill (impregnate) the formed void spaces between the reinforcements. They do require an additional processing step which involves chemical reaction of cross-linking the polymer chains which is known as curing. On the other hand, thermoplastic matrices do not require this step, but,

4

impregnation of the empty regions between the solid inclusions is hindered due to the matrix high viscosity [15].

1.3.2 Reinforcing Phase

The role of the reinforcing phase is to carry the structural load, reduce thermal stresses and provide macroscopic stiffness and strength to the composite [16]. They can be in the form of particles, whiskers or fibers. Fibers are widely used in polymer composites manufacturing and they are usually spun from a solution or melt. Common fibers used for reinforcement are aramidic, boron, carbon and E-glass with diameters usually of the order of 7-20 μm [17]. The most widely used fiber is the E-glass fiber, primarily due to the low costs involved. Composites containing discontinuous fibers are called short fiber or long fiber composites, whereas composites with continuous fibers are known as advanced composites. For advanced composites, the fibers are used in the form of rovings, yarns, strands and tows or bundles [16]. These yarns or tows can be combined in various forms and in a multitude of directions in the composite part, creating usually a three dimensional network with pores. The spacing between the fiber tows or bundles is on the scale of millimeters while the spacing between the fibers inside the bundle is of the scale of microns. Based on this description many advanced composites are also frequently characterized as dual scale porous media.

1.3.3 Permeability and Porous Flow

The ease with which the polymer can flow through the fibrous network of the composite is expressed by permeability. It is a quantity (with units of cm^2 or m^2) that describes the fluid flow resistance in any porous medium, including geological materials (e.g. porous rocks). Permeability is a function of the composite's microstructural architecture and, as in geological materials, it is anisotropic (different flow resistance and consequently different permeability values in different directions). It was measured for the first time by Darcy in 1856 using a sand column subjected to constant pressure gradient of water. The porous medium was considered isotropic so one needed just one value of permeability for a given architecture of the porous media. Knowing the viscosity of water and measuring the flow rate, he calculated the permeability of the sand bed by using a simple equation, which is now known as Darcy's law and it can be found in virtually every book on transport in porous media (e.g. [18], [19]).

Generally, Darcy's law has found an enormous applicability in dual scale polymer composites mainly for numerical prediction of the composite's permeability. From modeling perspective, it may be regarded as an empirical equivalent of the Navier-Stokes equation averaged over a very large number of individual micropores [20]. The objective, when modeling approaches, for such dual scale porous media, are followed, is to develop a numerical scheme to predict the effective permeability by calculating the overall permeability in a representative periodic unit cell containing a porous fiber bundle of circular or elliptic cross-section (see Appendix B). Darcy's law, describing the flow inside the porous bundle, is solved simultaneously with the (Navier-) Stokes equation along with an interface condition between the porous region and the surrounding fluid (see Appendix B). However, a direct application of Darcy's law is not always preferred for this coupled formulation due to the presence of the surrounding fluid in motion, as the slip-flow or boundary layer effects cannot be described correctly [21], because there is no macroscopic shear term in this equation [22]. In this regard, the Brinkman equation is widely accepted to describe flows in the porous media coupled with a surrounding flowing fluid. The Brinkman equation can be considered as a modification of Darcy's law by addition of the macroscopic viscous diffusion term to attain the compatibility near the boundary layer, the effect of this term quickly vanishes, as one moves away from the boundary layer into the porous media. It is worthwhile to note that there have been alternative approaches that prefer the use of the Darcy equation with a proper interfacial slip condition rather than the use of the Brinkman equation [23]. Construction of proper interface conditions is itself a difficult issue. Among others, two interface conditions are widely used with the Brinkman equation: the continuous stress condition and the stress jump condition of Ochoa-Tapia and Whitaker [24,25].

1.4 Variable Cross-Section Processing Flows

Plastic films, sheets, narrow tapes, webs, textiles and thin composite tapes, strands or rovings, can be manufactured using a relatively large number of processes. Generally, in some of these processes the polymer melt flows between two rigid quasi-parabolic walls (e.g. cylinders) in relative motion and close proximity which are separated by a variable gap. The relative motion develops pressure in the gap which can push the polymer into (penetrate) the wall if permeable. Deformable and permeable walls may be also penetrated by a fluid and more importantly they have the tendency to dramatically alter the shape of the gap and thus the cross-section of the flowing melt. The separation forces can reach

6

very high values and in the process of calendering the minimum gap can be higher in the central portion due to roll deflection [26]. The cross-section may also change when a viscoelastic polymer exits from a channel, swells and subsequently stretched (drawn) by a rotating part, which is usually of cylindrical geometry. The most common polymer and polymer composites processes where the above types of flows are frequently met are briefly described below.

1.4.1 Calendering

Calendering is a continuous process, in which a molten polymer enters usually as a thick and wide or narrow sheet on one of the counter-rotating rolls (or calenders) and leaves the roll pair with a reduced thickness and increased width. This is due to pressure build-up in the cross-machine direction that essentially forces the material to become wider, the determination of which is vital for design purposes. The above were studied for the first time experimentally by Unkrüer [27], and till today this remains the only detailed experimental work on the fully 3D nature of the process. Several numerical methods followed after Unkrüer using the lubrication approximation and 2D approaches to describe the motion of a Newtonian or non-Newtonian fluid between the rollers, presenting calculations for the downstream pressure distribution in the gap, roll separation force and torque requirements. The only 3D numerical work carried out so far for the process description is by Luther and Mewes [28] revealing the spiral motion of the fluid, but without predicting how the material spreads nor giving estimation of pressure variation in the cross-machine direction.

1.4.2 Film Casting

Film casting can be conceptually regarded as an open-calender process. Instead of a roll pair a single roll rotates and draws (stretches) the molten polymer emerging from a wide slit or flat die (of very small uniform gap) for sheet or film production. The roll, which is thermally controlled for cooling purposes (also called chill roll) of the emerging thin and wide sheet or film, is located at some distance away from the die exit. Immediately after the film emerges from the flat die, its cross-sectional area is locally higher than the die's cross-section (die or extrudate swell phenomenon), which is associated with polymer elasticity. Although there are numerous studies in the open literature on narrowing of the film (necking), inclusion of extrudate swell in the process and how it is affected by the drawing speed of the roller has received little attention. In

7

fact, there is only one numerical study by Kwon [29], which suggests that studying the problem poses a challenging task.

1.4.3 Pin-Assisted Pultrusion

Pin-assisted pultrusion is a manufacturing process for the production of composite tapes, webs, strands or rovings [30,31]. In the process, a porous composite material is pulled over a sequential arrangement of cylinders fully immersed in a melt bath. The motion of the composite relative to the cylinder develops a pressure build-up in the non-uniform gap separating the surfaces that forces the melt to penetrate the composite to a certain extent. Estimation of the penetration depth is of primary importance for the process because it defines the final product properties. A high penetration depth (as compared to the thickness of the porous medium), is frequently desirable for the production of a high strength and durable product. A limited number of earlier numerical and experimental works for the process (e.g. [32-34]) has shown that penetration depth is affected by a large number of process and material parameters such as the pulling speed, melt viscosity, pulling tension, permeability (or porosity) of the composite, pressure in the gap and minimum distance between the composite and the cylinder surface. The penetration dynamics of the process has received only little attention in the past. Existence of a generic fluid penetration model able to combine the above-mentioned process parameters into a single dimensionless number and more importantly how it influences the level of penetration, has not yet been reported in the literature.

The permeable composite web or tape frequently used in the above process is also flexible. Generally, non-permeable and flexible layers, have received much attention in the past for processes very similar to the current, such as coating/rolling and printing of a moving deformable layer in the vicinity of a smooth or engraved cylinder [35,36]. Their main result is that the deformability of the layer significantly affects the gap shape formed by the layer and the cylinder, thus the cross-section of the flow, giving rise to some interesting effects, such as generation of lift forces [37]. Moving of a deformable and permeable web or tape over a cylinder has received a little attention [38,39]. Evidently, the fluid penetration dynamics are not fully understood. Thus, numerical approaches to understand the flow phenomena for processes where a permeable deformable web/sheet is in hydrodynamic interaction with a rigid wall, become important.

8

1.5 Thesis Objectives

The objective of this work is to study numerically certain flow phenomena in calendering, film casting and pin-assisted pultrusion for the production of thin film, sheet, composite tape and composite web. The specific objectives are to:

1. Investigate the 3D flow of Newtonian and shear-thinning melts in the calendering process by determining how the material conveys and spreads laterally between the calenders.

2. Investigate how the drawing speed imposed by the chill roll affects the extrudate swell of an emerging viscoelastic sheet from a wide rectangular die.

3. Investigate the fluid penetration dynamics in the process of pin-assisted pultrusion of a permeable substrate assuming a single cylinder and how the penetration depth is influenced by the process, fluid and substrate's parameters.

4. Investigate whether a generic correlation of the penetration depth, in the pin-assisted pultrusion with the more realistic sequential cylinders arrangement, with a dimensionless parameter that incorporates the large number of process and material parameters, can be established.

5. Investigate the fluid penetration dynamics, from a generalized perspective, of a flexible and permeable web/tape that moves in close proximity to a stationary rigid cylinder that may find applicability not only to pin-assisted pultrusion but also to the similar processes of coating/rolling and printing.

1.6 Thesis Outline

This is an article-based thesis and consists of five chapters corresponding to five papers published, accepted for publication or submitted in refereed journals. These are preceded by the present introductory chapter and followed by a chapter of general conclusions and four appendices. The appendices contain several comparisons of the thesis results with analytical or semi-analytical models, supplemented with results of mesh sensitivity analyses. The papers have been written by the author of the thesis and subsequently approved by the coauthor(s). The first four papers have been modified after receiving reviewers' comments. The fifth paper has been submitted in the form shown in the thesis without receiving any comments from external reviewers.

Chapter 2 is a paper by <u>Nickolas D. Polychronopoulos</u>, Ioannis E. Sarris and T.D. Papathanasiou published in *Polymer Engineering and Science*, 54 (7), 1712-1722 **(2014)**. This paper investigates the 3D features in the calendering process.

Chapter 3 is a paper by <u>Nickolas D. Polychronopoulos</u> and T.D. Papathanasiou published in *Applied Rheology*, 25, 42425 **(2015)**. This paper investigates the effect of drawing on extrudate swell in film casting.

Chapter 4 is a paper by <u>Nickolas D. Polychronopoulos</u> and T.D. Papathanasiou published in *Composites Part A: Applied Science and Manufacturing*, 71, 126-135 **(2015)**. This paper investigates resin infiltration of porous substrates in the pin-assisted pultrusion process.

Chapter 5 is a paper by <u>Nickolas D. Polychronopoulos</u> and T.D. Papathanasiou accepted in *Polymer Composites*, DOI: 10.1002/pc.23860 **(2015)**. This paper proposes a novel model involving a single dimensionless parameter for resin infiltration in pin-assisted pultrusion.

Chapter 6 is a paper by <u>Nickolas D. Polychronopoulos</u> and T.D. Papathanasiou submitted in *Transport in Porous Media*. This paper investigates the fluid penetration dynamics and the deformation of a flexible and permeable web moving in close proximity to a stationary rigid cylinder.

1.7 References

1. Vlachopoulos J., Strutt D., Polymer Processing, *Mat. Sci. Technol.* 19 (9), 1161-1169 (2003).
2. Tadmor Z., Gogos C.G., *Principles of Polymer Processing*, John Wiley & Sons, New York (2006).
3. Morton-Jones D.H., *Polymer Processing*, Chapman & Hall, London (1989).
4. Vlachopoulos J., Polychronopoulos N., Basic Concepts in Polymer Melt Rheology and their Importance in Processing, in *Applied Polymer Rheology: Polymeric Fluids with Industrial Applications*, ed. M. Kontopoulou, 1-27, John Wiley & Sons, New Jersey (2012).

5. Bird R.B., Armstrong R.C., Hassager O., *Dynamics of Polymeric Liquids*, Vol. 1, Wiley, New York (1987).

6. Weissenberg K., A Continuum Theory of Rheological Phenomena, *Nature*, 159, 310-311 (1947).

7. Vlachopoulos J., Extrudate Swell in Polymers, *Rev. Def. Beh. Mat.*, 3, 219-248 (1981).

8. Cable P.J., Boger D.V., A Comprehensive Experimental Investigation of Tubular Entry Flow of Viscoelastic Fluids: Part 1, Vortex Characteristics in Stable Flow, *AIChE J.*, 24, 869-879 (1978).

9. Denn M.M., *Polymer Melt Processing, Foundations in Fluid Mechanics and Heat Transfer*, Cambridge University Press, New York (2008).

10. Phan-Thien N., Tanner R.I., A New Constitutive Equation Derived from Network Thoery, *J. Non-Newtonian Fluid Mech.*, 2, 353-365 (1997).

11. Han C.D., *Rheology and Processing of Polymeric Material*, vols. 1–2, Oxford University Press, Oxford, UK (2007).

12. Dealy J.M., Larson R.G., *Structure and Rheology of Molten Polymers*, Hanser, Munich (2006).

13. McLeish T.C.B., Larson R.G., Molecular Constitutive Equations for a Class of Branched Polymers: The Pom-Pom Polymer, *J. Rheol.*, 42 (1), 81-110 (1998).

14. Macosko C.W., *Rheology: Principles, Measurements and Applications*, VCH Publishers, New York (1994).

15. Advani S.G., Murat Sozer E., Process Modeling in Composites Manufacturing, Marcel-Dekker, NewYork (2003).

16. Astrom T., *Manufacturing of Polymer Composites.* Chapman and Hall, London (1997).

17. Gutowski T.G., *Advanced Composites Manufacturing.* Wiley, 1997.

18. Dullien F.A.L., *Porous Media: Fluid Transport and Pore Structure*, Academic Press, San Diego (1992).

19. Bear J., *Dynamics of Fluids in Porous Media*, Dover, New York (1988).

20. Hwang W.R., Advani S.G., Numerical Simulations of Stokes-Brinkman Equations for Permeability Prediction of Dual Scale Fibrous Porous Media, *Phys. Fluids*, 22, 113101 (2010).

21. Beavers G.S., Joseph D.D., Boundary Conditions at Naturally Permeable Wall, *J. Fluid Mech.*, 30, 197-207 (1967).

22. Neale G., Nader W., Practical Significance of Brinkman's Extension of Dardy's law: Coupled Parallel Flows Within a Channel and a Bounding Porous Medium, *Can. J. Chem. Eng.*, 52, 475-478 (1974).

23. Nield D.A., The Beavers-Joseph Boundary Condition and Related Matter: A Historical and Critical Note, Transp. Porous Media, 78, 537-540 (2009).

24. Ochoa Tapia J.A., Whitaker S., Momentum Transfer at the Boundary Between a Porous Medium and a Homogeneous Fluis–I. Theoretical Development, *Int. J. Heat Mass Transfer*, 38, 2635-2636 (1995).

25. Ochoa Tapia J.A., Whitaker S., Momentum Transfer at the Boundary Between a Porous Medium and a Homogeneous Fluis–II. Comparison with Experiment, *Int. J. Heat Mass Transfer*, 38, 2647-2655 (1995).

26. Coaker A.W., Calendering in *Handbook of Plastic Materials and Technology*, ed. Rubin I.I., 1099-1116, Wiley, New York (1990).

27. Unkrüer W., Beitrag zur Ermittlung des Drucksverlaufes und der Fliessvorgänge im Walzspalt bei der Kalanderverarbeitung von PVC Hart zu Folien. PhD Thesis, IKV, TU Aachen (1970).

28. Luther S., Mewes D., Three Dimensional Polymer Flow in the Calender Bank. *Polym. Eng. Sci.*, 44, 1642–1647 (2004).

29. Kwon Y., One-dimensional Modeling of Flat Sheet Casting or Rectangular Fiber Spinning Process and the Effect of Normal Stresses, *Korea-Australia Rheol. J.* 11, 225–232 (1999).

30. Gibson A.G., Månson J-A, Impregnation Technology for Thermoplastic Matrix Composites, *Compos. Manuf.*, 3 (4), 223–233 (1992).

31. Bijsterbosch H, Gaymans RJ. Impregnation of Glass Rovings with a Polyamide Melt. Part 1: Impregnation Bath. *Compos. Manuf.*, 4 (2), 85–92 (1993).

32. Gaymans R.J., Wevers E., Impregnation of a glass fiber roving with a polypropylene melt in a pin assisted process, *Compos. Part A: Appl. Sci. Manuf.*, 29, 663–670 (1998).

33. Bates P.J., Charrier J.M., Effect of process parameters on melt impregnation of glass roving, *J. Thermoplast. Compos. Mater.*, 12 (4) 276–296 (1999).

34. Bates P.J., Zou X.P., Polymer Melt Impregnation of Glass Roving, *Int. Polym. Process.*, 7 (4), 376–86 (2002).

35. Coyle D.J., Forward Roll Coating with Deformable Rolls: A Simple One Dimensional Elastohydrodynamic Model, *Chem. Eng. Sci.*, 43, 2673-2684 (1988).

36. Yin X., Kumar S., Lubrication Flow between a Cavity and a Flexible Wall, *Phys. Fluids* 17, 063101 (2005).

37. Skotheim J.M., Mahadevan L., Soft lubrication, *Phys. Rev. Lett.*, 92, 245509 (2004).

38. Chen K.S.A., Scriven L.E., Liquid Penetration into a Deformable Porous Substrate, *Tappi J.*, 73, 151-161 (1990).

39. Devisetti S.K., Bousfield D.W., Fluid Absorption During Forward Roll Coating on Porous Webs, *Chem. Eng. Sci.*, 65, 3528-3537 (2010).

Chapter 2

3D Features in the Calendering of Thermoplastics:
A Computational Investigation

Abstract

We present results of a fully three-dimensional computational study of the calendering process of thermoplastics using the fluid dynamics software *OpenFOAM*. Our aim is to elucidate unique 3D features of the process, such as spreading and melt flow. We assume that the material is fed in the form of a sheet of finite thickness and detaches from the cylinders at a prescribed thickness. The rotational motion of the cylinders, the consequent pressure build-up (both in the machine and the transverse directions) and the presence of the free surfaces (sides) of the calendered sheet − both deformable and at ambient pressure − forces the thermoplastic melt to spread in the transverse direction. A decoupled iterative procedure is used to predict the shape of the spreading side surfaces under different conditions. A spiraling transverse flow pattern in the melt feeding section is shown to exist, which determines the actual flow path of the calendered material in a non-intuitive way. We show that insofar as the material redistribution (from the fed sheet to the produced film) during the process is concerned, the results of the present analysis predict a 3D spiral flow pattern and a redistribution of the fed material from the central region of the fed sheet to the sides of the calendered product.

2.1 Introduction

Calendering is a widely used manufacturing process which involves a set of usually four corotating heated calenders (rolls) for the production of thin plastic sheets and films. The thermoplastic melt is fed behind the nip region of the two calenders, the rotational movement of which forces the material to flow in the machine direction, with subsequent detachment from the rollers surface at a specific thickness. Simultaneously the material flows and spreads in the lateral direction. Two-roll calendering lines are usually used for rubber processing whereas four-roll calenders are generally employed for the production of double-coated products meeting strict surface quality requirements.

14

Gaskell [1] presented a theoretical analysis of the calendering process based on the assumption that the diameter of the rolls is large compared to the gap between the calenders and as a result the flow in the machine direction can be approximated as one-dimensional. He considered Newtonian fluids as well as Bingham plastics and derived the relevant equations to predict the pressure drop in the machine direction, that being of primary interest in design. McKelvey [2] and Middleman [3] extended the study of Gaskell [1] to power-law fluids. A theoretical approach to study the calendering of power-law fluids was also shown by Brazinsky et al. [4]. Alston and Astill [5] presented a unidirectional analysis for the calendering process of non-Newtonian fluids described by a hyperbolic tangent viscosity model, exhibiting Newtonian behavior at high and low shear rates and a shear-thinning behavior at intermediate shear rates. Vlachopoulos and Hrymak [6] studied (theoretically and experimentally) the calendering of rigid PVC (polyvinyl chloride) employing a non-isothermal power-law model based on lubrication theory. More recently numerical studies were carried out by Sofou and Mitsoulis [7,8] for the calendering of viscoplastic and pseudoplastic materials using the lubrication approximation with no-slip and slip at the calender's surfaces. Kiparissides and Vlachopoulos [9] studied computationally the pressure distribution in the machine direction for symmetric and asymmetric calendering of Newtonian and non-Newtonian fluids using the finite element method. The same authors [10] used a finite-difference non-isothermal model to study the temperature distribution in the calender gap, including the effect of viscous dissipation; they predicted local temperature maxima near the surfaces of the calenders - regions associated with high shear - but only a small rise in the temperature of the calendered product. Agassant and Espy [11] and Agassant [12] studied the flow between the calenders computationally using a 2D finite element method and complemented computational results with calendering experiments using rigid PVC; they observed the formation of a melt bank showing a large recirculation zone, with smaller vortices developing near the entry region. Mitsoulis et al. [13] performed 2D non-isothermal analyses for Newtonian and power-law fluids by means of the finite element method in which they included the melt bank shape determination among other results.

Incidentally, calendering is not confined to thermoplastics. The process of rolling is used extensively in the production of metal sheets as well as in the forming of ceramic pastes [14-22]. In the context of the production of a metal strip from the molten state, Matsumiya and Flemmings [23] studied the spreading of the material using the lubrication approximation. The authors describe the rheological behavior of the alloy as a power-law

15

fluid and assume that the pressure does not vary in the machine direction; the only non-zero velocity is therefore the one in the transverse direction. Johnson [24] studied small-scale spreading of metals undergoing plastic deformation during metal sheet rolling - employing an asymptotic formulation with the spreading sides treated as free surfaces - as well as the pressure distribution along the cylinder axis. Sezek et al. [25] studied cold and hot metal plate rolling using a three-dimensional mathematical model considering lateral spreading of the plate based on the minimization of power consumption during the process; a third order polynomial approximation was used to describe the shape of the free side surfaces. Considering two-dimensional flow (in the machine and in the transverse directions) and using gap-averaged quantities, Levine et al. [26] developed a 2D model for the pressure field in the region between the rotating cylinders using the essential tenets of the lubrication approximation. Use of this approach allowed for the determination of the shape of the spreading sheet as well as of the two-dimensional variation of pressure both in the machine and the transverse directions.

Study of three-dimensional effects in the calendering of thermoplastics has been limited. Unkrüer [27] carried out experiments using a calender having two rolls of 80 mm diameter and 1600 mm length, using PVC and PS (polystyrene) as calendered materials. His conclusions were that (*i*) the calendered sheet spreads and (*ii*) three vortices are formed in and near the melt bank and (*iii*) the material in the melt bank conveys to the sides through a spiral motion. He also observed and measured the pressure drop in the transverse direction. A 3D simulation of the calendering process was carried out by Luther and Mewes [28], with their results also predicting the spiral motion of the material in the melt bank. The authors however did not include a prediction for the spreading of the calendered sheet or of the existence of a pressure profile in the direction of the calender axes (transverse direction).

Given the state-of-the-art outlined above, the scope and contribution of the present work is to solve the fully 3D Stokes equations in geometries realistically relevant to the calendering process and predict the spreading of the sheet, as well as the fully 3D pressure and flow patterns occurring as the material passes through the calenders. The study is performed under isothermal conditions, as explained and justified in subsequent section. We employ the Generalized Newtonian Fluid (GNF) constitutive model for the calendered material, with material and processing parameters relevant to plastics calendering e.g. calender radius 125 mm, final thickness of the sheet approximately 1.25 mm and a polymer melt such as PVC. It is also assumed that the material behaves as a purely viscous

fluid, thus any elastic effects caused by a second stage calender pair (i.e. pulling tension) are neglected. In our analysis, the spreading sides of the calendered sheet are deformable free surfaces the shape of which is unknown and determined in the course of the computation. This determination is carried out by means of a decoupled numerical procedure, as outlined in subsequent section. The results are validated by comparing the predicted pressure distribution in the machine direction to existing analytical solution [3, 6].

2.2 Model Equations

The governing equations for isothermal incompressible steady state flows of polymer melts are the continuity equation

$$\nabla \cdot \mathbf{u} = 0 \tag{2.1}$$

where $\mathbf{u}$ is the velocity vector, and the equation for the conservation of momentum in the absence of fluid inertia (Stokes equations)

$$0 = -\nabla p + \nabla \cdot \mathbf{T} \tag{2.2}$$

where p is the pressure and $\mathbf{T}$ is the deviatoric stress tensor. For purely viscous (inelastic) fluids, the rheological constitutive equation that relates the stresses to the velocity gradients is the GNF model

$$\mathbf{T} = \eta(II_{\mathbf{D}}) \cdot \mathbf{D} \tag{2.3}$$

where $\mathbf{D}$ is the rate of strain tensor

$$\mathbf{D} = \nabla \mathbf{u} + \nabla \mathbf{u}^T = \frac{\partial u_i}{\partial x_j} + \frac{\partial u_j}{\partial x_i} \tag{2.4}$$

and $II_{\mathbf{D}}$ is the second invariant of the rate of strain tensor given by

$$II_{\mathbf{D}} = \mathbf{D} : \mathbf{D} \tag{2.5}$$

For fluids with Newtonian behavior $\eta = \mu$, where μ is the Newtonian viscosity. The non-Newtonian rheological model used in the present work is the power-law in which the viscosity is a function of the second invariant ($II_{\mathbf{D}}$) of the rate of strain tensor $\mathbf{D}$. The power-law viscosity model is given by

$$\eta(II_{\mathbf{D}}) = m \left| \frac{1}{2} II_{\mathbf{D}} \right|^{\frac{n-1}{2}} \quad \text{for} \quad \eta(II_{\mathbf{D}}) < m \tag{2.6}$$

$$\eta(II_{\mathbf{D}}) = \eta_T \quad \text{for} \quad \eta(II_{\mathbf{D}}) > m \tag{2.7}$$

where m the consistency index, n the power-law exponent and η_T a truncation viscosity. A schematic of a typical geometry at the mid-plane of a spreading calendered sheet is shown

17

in Fig. 2.1. The machine, thickness and transverse directions correspond to the x, y and z axes, respectively, of a Cartesian coordinate system. The size of the gap $H(x)$ between the calenders is found through the following simple equation

$$H(x) = H_o + R - \sqrt{R^2 - x^2} \qquad (2.8)$$

where R is the radius of the calenders and H_o is the half gap at the nip region ($x=0$) (see Fig. 2.1). The equation above (Eq. 2.8) treats the surface of the calenders as cylindrical, in
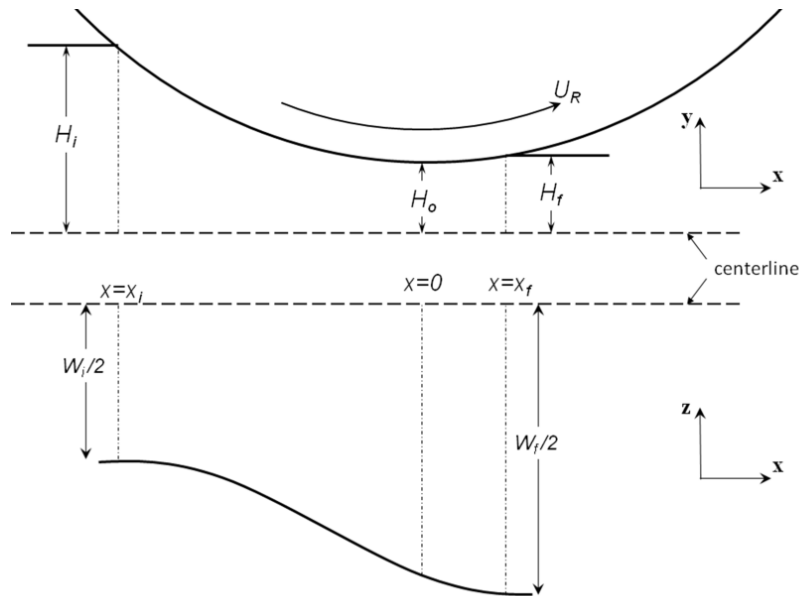
Figure. 2-1: Schematic representation of the half-geometry. $W_i/2$ is half the sheet width at the entrance point x_i with sheet half-thickness H_i. $W_f/2$ is the half-width of the sheet at the detachment point x_f, at which point its half-thickness is H_f. H_o is the half-gap at the nip region ($x=0$). Top: view in the thickness direction (x-y plane); Bottom: view in the transverse direction (x-z plane). The x-direction is the direction of bulk flow (machine direction), while z is the direction along the axis of the calendar (transverse direction).

contrast to earlier formulations (e.g. Gaskell [1], McKelvey [2], Middleman [3]) that assumes parabolic calender surfaces (a reasonable approximation for flow fields extending only a small distance from the nip region). Applying the approximation of Middleman [3] with $H_f/H_o=1.226$ to Eq. 2.8 and solving with respect to x, yields the detachment point x_f (the point where the sheet leaves off the calenders surface). In the same way, for a given initial thickness $2H_i$, substitution into Eq. 2.8 yields the biting position x_i of the sheet. An actual computational model of the full 3D geometry we consider, including a curved side (free) surface (as determined at the end of the solution procedure) is shown in Fig. 2.2. The model equations are non-dimensionalized using

$$x' = \frac{x}{\sqrt{2RH_o}} \, , \; z' = \frac{z}{W_i} \; \text{and} \quad p' = \frac{p}{m}\left(\frac{H_o}{U_R}\right)^n \tag{2.9}$$

where instead of the consistency index (m) the Newtonian viscosity (μ) is used when $n=1$ and U_R is the velocity at the cylinder surfaces. The following boundary conditions for the velocity apply (see Fig. 2.1):

a) No-slip at both cylinders surface (wall conditions).

b) Fixed value for the volumetric flow rate (q_{in}) at the entrance boundary ($x=x_i$) (inlet condition), given by $q_{in}=2H_iU_iW_i$, where H_i the half-gap, U_i the feeding sheet speed and W_i the sheet width at the entrance boundary.

c) At the exit boundary ($x=x_f$) a Neumann condition is used (fully-developed outlet condition), namely $\frac{\partial \mathbf{u}}{\partial \mathbf{n}} = 0$, where $\mathbf{n}$ is the unit vector normal to the outflow boundary.

d) At the side (free) surface $z=z(x)$ boundaries free surface conditions apply, namely $\mathbf{u}\cdot\mathbf{n}=0$ (no flow passes across these surfaces) and $\mathbf{T}\cdot\mathbf{n}=0$ (shear-free condition on the side spreading surfaces, or, equivalently, zero values for the components of the traction vector). The boundary conditions for the Stokes equation (Eq. 2.2) include also the value of pressure at the boundaries, which was set to a fixed (ambient) value ($p=0$) for the entrance ($x=x_i$), exit ($x=x_f$) and side (free) surface ($z=z(x)$) boundaries.

2.3 Numerical Procedure

For the solution of the continuity equation (Eq. 2.1) and the Stokes equations (Eq. 2.2) we use the OpenFOAM (Open Source Field Operation and Manipulation) package, employing the Finite Volume Method (FVM). The FVM subdivides the flow domain into a finite number of smaller control volumes (cells) (see Fig. 2.2 in which the same flow domain is shown from three different view angles). The size of the flow domain in Fig. 2.2 (8×10^5 cells) was determined based on the aspect ratio of the cells filling the domain. In all cases the maximum allowed cell aspect ratio for the Newtonian fluid was set to 30. For the cases with small spreading (e.g. $W_i/2H_o=200$) of the sheet the maximum aspect ratio of the cell was set to 10. Concerning the cases with higher sheet spreading (e.g. $W_i/2H_o=80$), filling the domain with 8×10^5 cells would give a maximum allowed cell aspect ratio of 30. For the non-Newtonian simulations, a more dense mesh arrangement was employed with 2.4×10^6 cells which gave a maximum cell aspect ratio of 20 for both the lower (e.g. $W_i/2H_o=200$) and higher (e.g. $W_i/2H_o=80$) sheet spreading. The continuity and the Stokes equations are then discretised and integrated over each control volume by properly

19

approximating the variation of flow properties between computational nodes. The steady-state incompressible solver uses the SIMPLE algorithm (Semi-Implicit Method for Pressure Linked Equations) introduced by Patankar and Spalding [29].
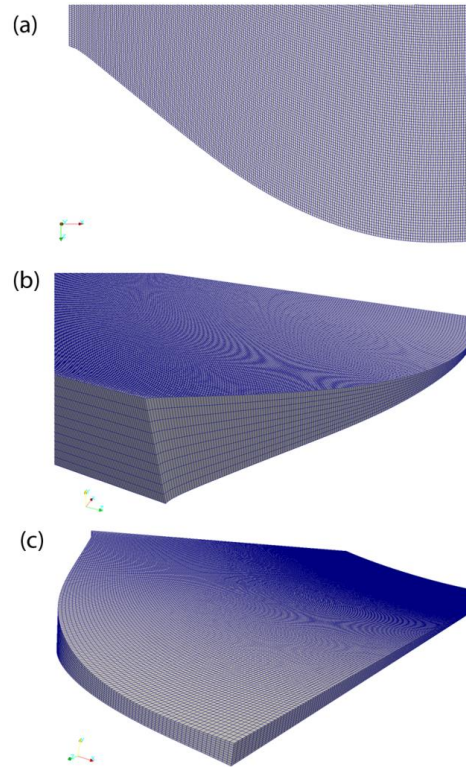
Figure 2-2: 3D discretised computational flow domain (8×10^5 cells) for $W_i/2H_o$=100 from three different view angles, (a) half-geometry view from the top, (b) side view near the inlet and (c) same side view near the outlet.

2.3.1   Validation

The results of the 3D model were validated against the analytical solution as derived from the lubrication approximation theory (Middleman [3]) for a power-law fluid. In dimensionless form, the analytical solution for the pressure drop in the machine direction is

$$\frac{dp'}{dx'} = -\left(\frac{2n+1}{n}\right)^n \sqrt{\frac{2R}{H_o}} \frac{\left(x_f'^{\,2} - x'^2\right)\left|x_f'^{\,2} - x'^2\right|^{n-1}}{\left(1 + x'^2\right)^{2n+1}} \qquad (2.10)$$

The material utilized (PVC with m=46120Pa·s^n and n=0.34) and the geometry for the construction of the 3D computational flow domain for the simulations (R=125mm, H_o=0.3mm, U_R=73.83 mm/s, H_f =0.3765 mm) were those used by Vlachopoulos and Hrymak [6]. The validation is based on the comparison of the computed pressure

20

distribution in the machine direction (x–direction) to the result obtained by integrating Eq. 2.10 using a fourth-order Runge-Kutta algorithm. For this comparison to be relevant, it is
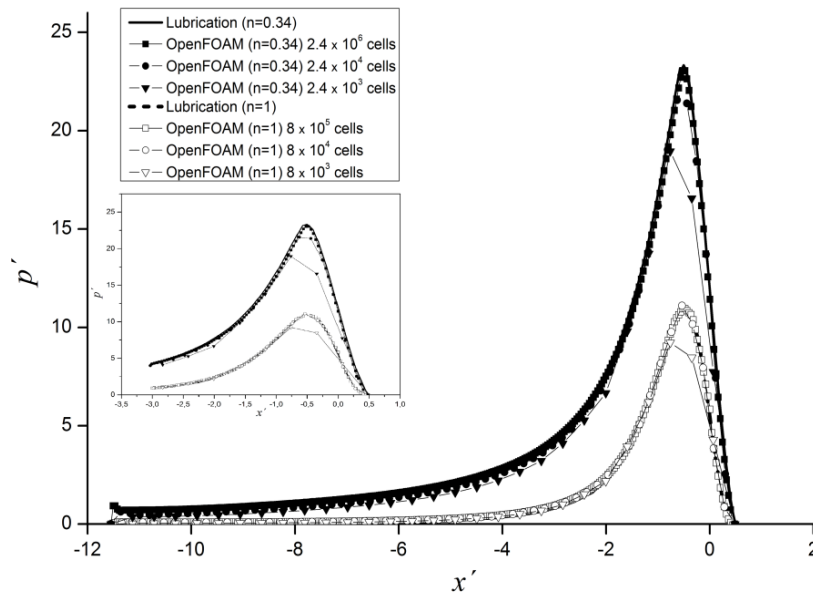
Figure 2-3: Comparison between 3D numerical results (OpenFOAM) and results from Lubrication Approximation for the pressure distribution in the x-direction for a power-law fluid (Eq. 2.9 with m=46120 Pa·s^n and n=0.34 [6]) and a Newtonian (Eq. 2.9 with μ=4612 Pa·s and n=1) fluid under three different mesh arrangements. The insert is a magnified view of the pressure distribution near the nip region x'=0.

assumed that the material is fed from an infinite reservoir located far behind the nip region and that no spreading of the calendered sheet takes place; specifically, the boundary conditions at the vertical surfaces of the sheet sides were a zero pressure gradient and a zero velocity gradient in the transverse direction (z-direction) thus simulating a calender of infinite width. Fig. 2.3 illustrates the calculated pressure distribution in the machine direction for three different mesh densities and for a power-law fluid. It is clear that for 2.4×10^6 cells the pressure distribution is in excellent agreement with the analytical solution (Eq. 2.10). Decreasing mesh density to 2.4×10^4 cells a relatively small underestimation of the pressure distribution is observed while further lowering of mesh density leads to increased underestimation of pressure. Comparison of the pressure distributions for a Newtonian fluid, using the same geometry and assuming Newtonian material with μ=4612 Pa·s are also shown at Fig. 2.3 to be in excellent agreement with the analytical solution. The insert in Fig. 2.3 represents a magnified view of the pressure distribution for a small region around the nip (x'=0).

21

Concerning the effect of non-isothermality, Kiparissides and Vlachopoulos [10] presented results of non-isothermal 2D calendering simulations for Newtonian and power-law fluids. They showed that viscous dissipation is small and that under usual operating conditions (e.g. for R=150 mm, U_R=0.4 m/s, H_o=0.25 mm and a power-law fluid with m=2.5×10^4 Pa·s^n and n=0.25) the temperature rise in the produced film is less than 2^oC. This was also investigated in the present work for the geometry shown in Fig. 2.2 (R=125 mm, U_R=0.1 m/s, H_o=0.5 mm) and a power-law material (n=0.34) with temperature dependent consistency index m given by an Arrhenius expression $m=m_o\exp[-b(T-T_{ref.})]$ where m_o=5×10^4 Pa·s^n is the consistency index at the reference temperature ($T_{ref.}$=180^oC) and b=0.07 ^{o}C^{-1} is the temperature sensitivity parameter. The material enters the flow domain at the same temperature as the calenders (T_{melt}=T_{wall}=180^oC) and the spreading sides are regarded as adiabatic. In this simulation, the maximum observed temperature rise was 3^oC and the effect on the sheet spreading and vortex formation, which are the main objectives of this paper, were non-discernible. In the following we present results of strictly isothermal simulations.

2.3.2   Prediction of Sheet Spreading

In calendering, the rotational movement of the calenders creates a drag flow which, due to the reduced flow gap in the machine direction (x-direction), results in a pressure build-up behind the nip region. This pressure not only affects the melt flow in the machine direction, but, since the sides of the calendered sheet are at ambient pressure, forces the melt to move (spread) in the transverse direction (z-direction) as well. It is this transverse pressure gradient that causes the polymer sheet to spread as it passes through the calenders. In this study, it is assumed that the material is fed as a sheet of uniform thickness and speed (e.g. from a conventional flat coat-hanger die attached to an extruder located behind the calenders). It is also assumed that the shape of the side (free) surfaces varies only in the x and z directions − no curvature is assumed in the y (thickness) direction. Computationally, the shape is determined based on the physical condition that the points of the free surface belong to a streamline, thus satisfying the following equation at each point on the side surface

$$\frac{dz}{dx} = \frac{\overline{w}}{\overline{u}} \qquad (2.11)$$

where dz/dx is the local slope of the free surface (see for example Fig. 2.1) and $\bar{u}$, $\bar{w}$ are the gap-averaged velocity components in the x and z directions respectively, at the same position. These gap-averaged velocities are calculated as

$$\bar{u} = \frac{1}{N_y} \sum_{i=1}^{N_y} u_i \tag{2.12}$$

$$\bar{w} = \frac{1}{N_y} \sum_{i=1}^{N_y} w_i \tag{2.13}$$

where N_y is the number of the gap-wise mesh nodes in the y direction. For the Newtonian simulations, we used N_y=11, while for the power-law simulations N_y=31. The total number of cells (control volumes) filling the computational flow domain was 8×10^5 for the Newtonian and 2.4×10^6 for the power-law simulations. Determination of the shape $z(x)$ of the sides of the calendered sheet is achieved through a decoupled iterative procedure, in which the continuity equation (Eq. 2.1) and the Stokes equations (Eq. 2.2) are solved (starting with initial (base) configuration of a sheet of uniform width) and in which the shape of the side surface $z=z(x)$ is adjusted, based on solution of Eq. 2.11. Following solution of Eqs. 2.1 and 2.2, the velocities u and w at each location of the side surface in the y direction are known and thus the corresponding gap-averaged values can be calculated from Eq. 2.12 and 2.13 at each nodal position on the side surfaces. A new shape of these side (free) surfaces is then obtained by integrating Eq. 2.11 utilizing the above-computed gap-averaged velocities. A simple integration formula such as

$$z_j^{s+1} = z_0^s + \sum_{j=1}^{N_x} \frac{\bar{w}_j^s}{\bar{u}_j^s} \left(x_j^s - x_{j-1}^s \right) \tag{2.14}$$

was found sufficient. In Eq. 2.14 z_j represents the updated z-coordinate at the corresponding point at the sth iteration, z_o is the z-coordinate of the corresponding point at the entrance ($x=x_i$) (equal to the half-width of the sheet at the entrance), x_j–x_{j-1} the distance between two successive surface nodes in the x-direction and N_x the number of positions in the x-direction (N_x=201 for typical Newtonian and power-law simulations). After the new z-coordinates are predicted (via Eq. 2.14) and thus a new shape of the side (free) surface is obtained, a new three-dimensional computational flow domain is constructed, the continuity and Stokes equations (Eqs. 2.1 and 2.2) are solved and the procedure is repeated until convergence. The speed of convergence to the final shape of the spreading sheet is improved by employing a relaxation procedure

$$\hat{z}_j^{s+1} = (1-\omega)z_j^{s+1} + \omega z_j^s \tag{2.15}$$

23

with relaxation factors ω $(0.3<\omega<0.8)$ where $\hat{z}^{s+1}$ is the z-coordinate at the sth iteration. Convergence is obtained when the gap-averaged velocities ($\bar{u}$, $\bar{w}$) and the obtained side (free) surface shape $z=z(x)$, satisfy Eq. 2.11 so that the sum of the squares of the errors is less than a prescribed tolerance ($\varepsilon=10^{-3}$), namely:

$$\frac{1}{N_x}\sqrt{\sum_{j=1}^{N_x}\left(\frac{z_j-z_{j-1}}{x_j-x_{j-1}}-\frac{\bar{w}_j}{\bar{u}_j}\right)^2}\leq\varepsilon \qquad (2.16)$$

2.4   Results and Discussion

2.4.1   Prediction of Sheet Spreading

Figure 2.4 illustrates the shape (geometry) of the side (free) surface for the dimensionless ratio $W_i/2H_o=80$ (Fig. 2.4a) and $W_i/2H_o=150$ (Fig. 2.4b) for a Newtonian fluid with $\mu=6500$ Pa·s and $\rho=1000$ kg/m^3. The feed flow rate is set at $q_{in}=100$ kg/hr. Most of the spreading is shown to occur before the material reaches the nip region. For the case with $W_i/2H_o=80$, nineteen iterations where sufficient to reach convergence according to the criterion described by Eq. 2.16, as shown in Fig. 2.4a. Even from the fifth iteration the geometry of the free surface assumes a shape which is very similar to the final convergent
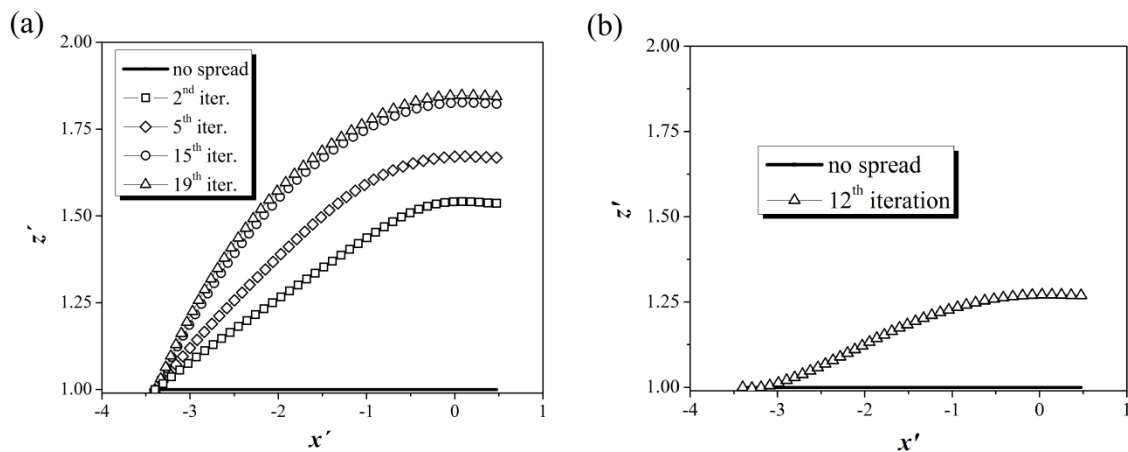
Figure 2-4: Free surface shape iterations for a Newtonian fluid with the filled points corresponding to the initial (base) configuration for no spreading, ($\mu=6500$ Pa·s) under a constant flow rate at the entrance ($q_{in}=100$ kg/hr) for (a) $W_i/2H_o=80$ (results of intermediate iterations shown, with the 19th iteration representing the final shape) and (b) $W_i/2H_o=150$ with the 12th iteration representing the final prediction of the side surface of the calendered sheet.

shape. In the case of a relatively narrow sheet ($W_i/2H_o=80$) (Fig. 2.4a) the sheet spreads by approximately 84%. Increasing the width of the entrance sheet so that $W_i/2H_o=150$ for

24

the same Newtonian material, the amount of spreading is reduced to about 27% as illustrated at Fig. 2.4b. The side (free) surface shape converges even faster and the tendency of the material to spread is less intense than the case of $W_i/2H_o$=80 (Fig. 2.4a). At a small region near the entrance, the sheet shows a small (see Fig. 2.4b), if any, tendency to spread ($dz/dx\sim0$) whereas in Fig. 2.4a the material starts spreading at the biting position (with reference to $x=x_i$ of Figure 1) of the calenders. The fact that the extent of spreading is a function of the width of the fed sheet has also been predicted by Levine et al. [26] using a 2D (x-z) lubrication analysis.
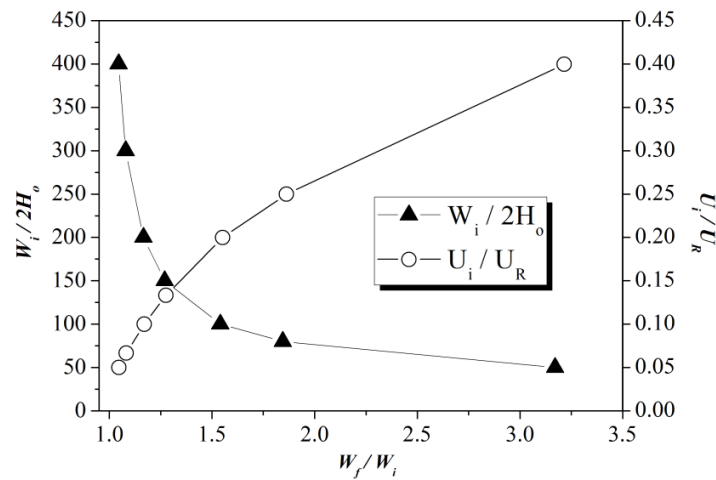
Figure 2-5: Effect of the sheet width and speed of the fed material (expressed by the ratios $W_i/2H_o$ and U_i/U_R), for a fixed value of q_{in}=100 kg/hr, on the spreading ratio W_f/W_i for $R/2H_o$=125, Newtonian fluid with μ=6500 Pa·s.

Figure 2.5 shows the effect of the entrance velocity (for a fixed flow rate at the entrance q_{in}=100 kg/hr), non-dimensionalized with the velocity of the calenders U_R, on the spreading ratio W_f/W_i for the Newtonian fluid. It can be seen that as the ratio U_i/U_R increases, implying a faster feeding of the melt, the spreading ratio W_f/W_i increases. At larger values of U_i/U_R the relationship becomes almost linear (the maximum spread for the studied Newtonian cases is obtained at $W_i/2H_o$=50 with U_i being 40% of the calenders velocity). At the same figure (Fig. 2.5) the effect of the entrance width of the sheet on the spreading ratio W_f/W_i is also illustrated. For large values of W_i the spreading ratio approaches asymptotically unity – for $W_i/2H_o$=400, W_f/W_i=1.05 (i.e. the unidirectional approach as described by the lubrication theory), while for smaller sheet width, the corresponding spreading is proportionally larger (e.g. for $W_i/2H_o$=50, W_f/W_i=3.17). Inversely, small values of the ratio U_i/U_R result in small spreading, while larger amounts of

25

spreading are associated with increased velocity of the fed sheet. Since in all cases the volumetric flow rate is kept constant, large U_i correspond to small W_i and vice-versa.

Figure 2.6 illustrates the effect of the thickness of the fed sheet (for a specific entrance flow rate q_{in}=100 kg/hr), expressed as a multiple of H_o, on the final spreading ratio W_f/W_i for the case of $W_i/2H_o$=100. An almost linear dependence is observed for H_i/H_o>4.
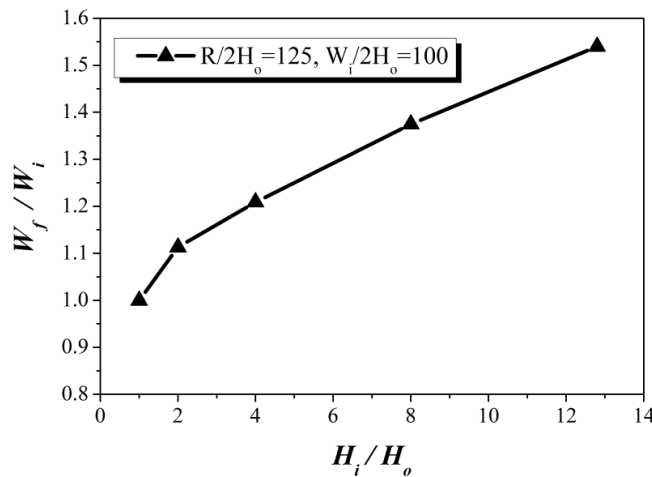
Figure 2-6: Effect of the ratio H_i/H_o on the spreading ratio W_f/W_i, for a fixed value of q_{in}=100 kg/hr, for $W_i/2H_o$=100 and $R/2H_o$=125, Newtonian fluid.
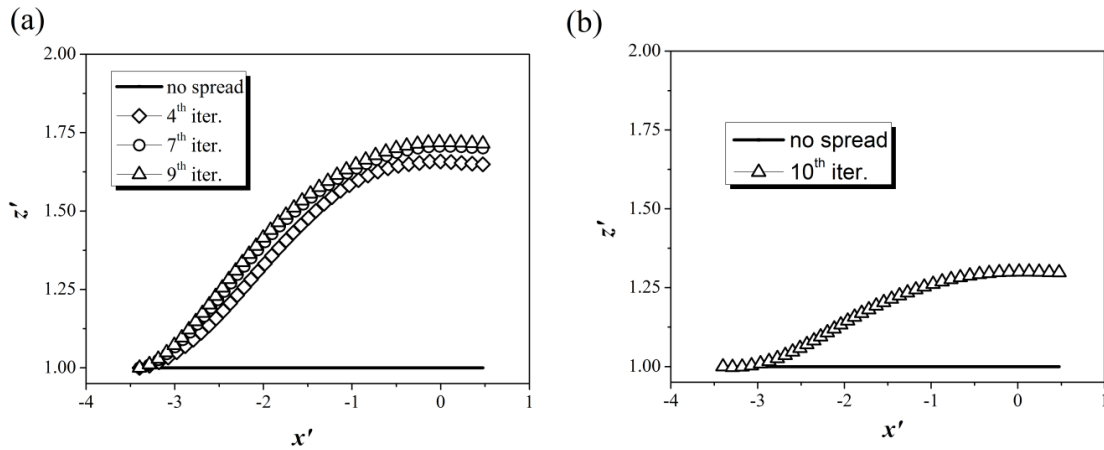
Figure 2-7: Free surface shape (iterations and final shape) for a power-law fluid with the filled points indicating the initial (base) configuration for no spreading (m=5×10^4 Pa·s^n, n=0.35) under a constant flow rate at the entrance (q_{in}=100 kg/hr). (a) $W_i/2H_o$=80 (with intermediate iterations) and (b) $W_i/2H_o$=150 (only the convergent shape shown).

Figure 2.7 illustrates the spreading of a non-Newtonian fluid for q_{in}=100 kg/hr, for $W_i/2H_o$=80 (Fig. 2.7a) and $W_i/2H_o$=150 (Fig. 2.7b) using the power-law model with

26

m=50000 Pa·s^n and n=0.35 (typical values for PVC). For $W_i/2H_o$=80 (Fig. 2.7a) and for a small region near the entrance (biting position), the geometry of the side (free) surface implies a negligible spreading tendency − probably affected by the relatively high melt viscosity in this low shear rate region. As the material progresses towards the exit, the prevailing shear rates increase as well as the pressure, and as a result the sheet begins to spread. The maximum extent of spreading achieved close to the nip region is due to the high pressure build up in this area. For $W_i/2H_o$=150 (Fig. 2.7b), and using the same m and n values, the side surface shape shown at Fig. 2.7b exhibits a lower spreading tendency than the case with $W_i/2H_o$=80 (Fig. 2.7a). Moreover, comparison of the final predicted side (free) surface shape for $W_i/2H_o$=150 between the Newtonian (Fig. 2.4b) and the power-law (Fig. 2.7b) fluid shows almost the same amount of final spreading. However, since the non-Newtonian material exhibits shear thinning behavior, near the entrance the spreading is less abrupt than the cases with Newtonian material (e.g. $W_i/2H_o$=80 with reference in Fig. 2.4a and Fig. 2.7a) due to the correspondingly higher viscosity. Although the volumetric flow rate at the entrance is held constant (q_{in}=100 kg/hr), the entrance velocity of the sheet changes when the width of the fed sheet changes. Since boundary conditions (d) (in section 2.2) ensure that the mass balance is maintained, reducing the entrance width sheet for the given volumetric flow rate, the entrance velocity becomes higher and vice versa resulting in different spreading ratios W_f/W_i.

2.4.2 Pressure profiles in the transverse direction

The predicted pressure profiles in the transverse direction for the case of $W_i/2H_o$=80 for a Newtonian fluid (μ=6500 Pa·s) are shown in Figure 2.8, at three different positions along the length of the sheet with x'=0 representing the position of the nip region and x'_f being the detachment point. At the nip region, the pressure distribution appears to have a fairly constant value for a large portion of the sheet width with rapid decrease near the two free surfaces (side edges) where the spreading takes place. At positions behind the nip region ($x'= -x'_f$ and $x'=-2x'_f$) the pressure profiles exhibit somewhat greater variability with the pressure being maximum at the central region of the sheet, and a sharp pressure gradient near the edges. The dimensionless pressure contours on the symmetry plane x-z (see Fig. 2.1) for the Newtonian fluid with $W_i/2H_o$=80 is shown in Fig. 2.9. Pressure profiles at the same x' positions as in the Newtonian fluid are obtained for the power-law
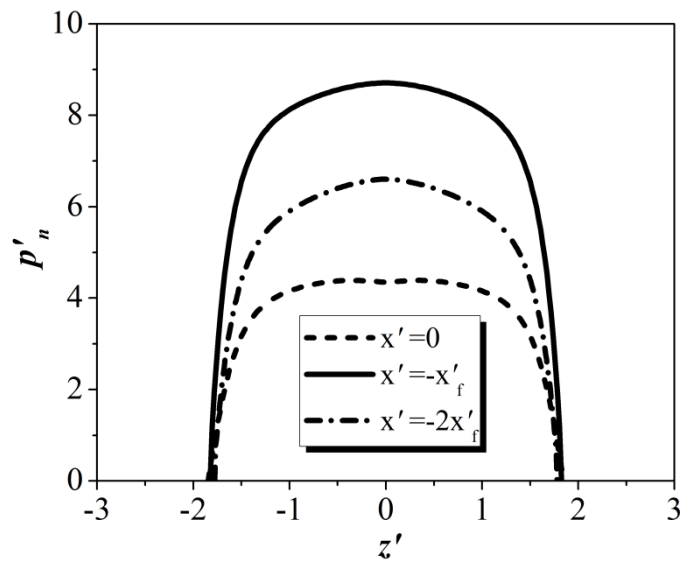
Figure 2-8: Dimensionless pressure distribution in the transverse direction (z–direction) of Newtonian fluid (μ=6500 Pa·s) for $W_i/2H_o$=80 with x'_f the dimensionless detachment point.
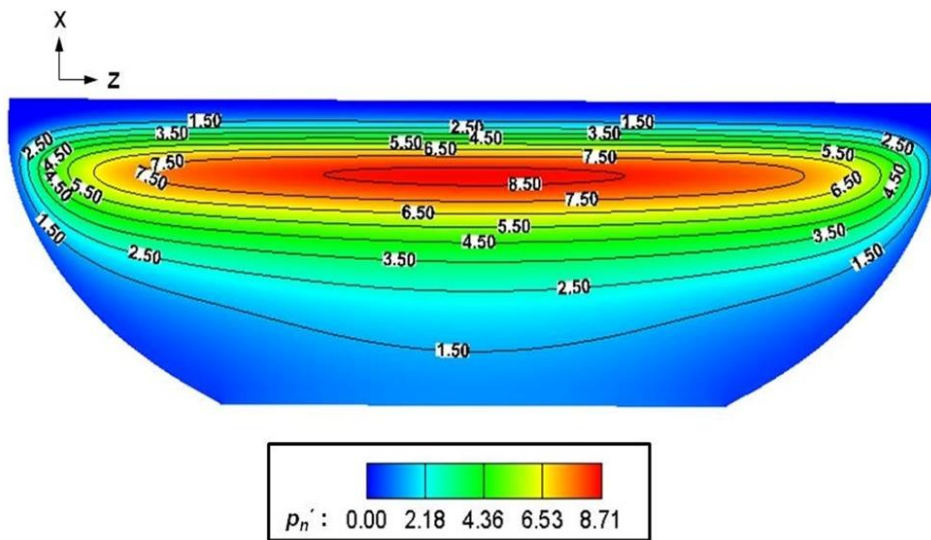
Figure 2-9: Dimensionless pressure contour plots on the x-z symmetry plane of the Newtonian fluid (μ=6500 Pa·s) for $W_i/2H_o$=80.

28
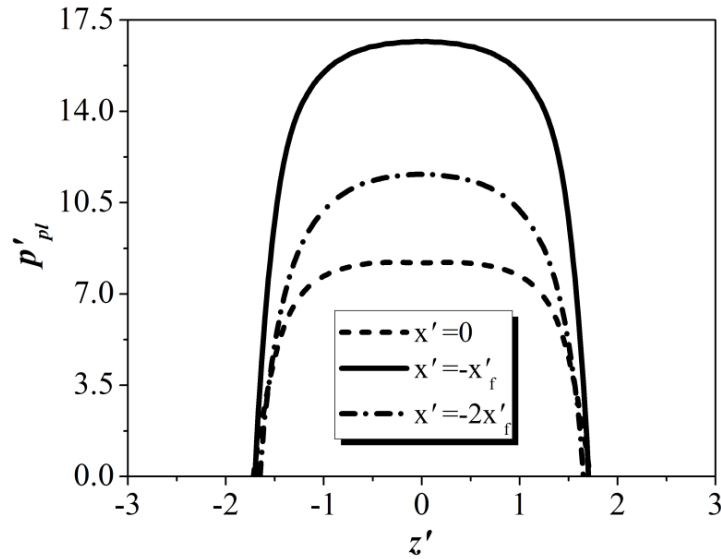
Figure 2-10: Dimensionless pressure distribution in the transverse direction (z-direction) of a power-law fluid ($m=5\times10^4$ Pa·s^n, $n=0.35$) for $W_i/2H_o=80$ with x'_f the dimensionless detachment point.
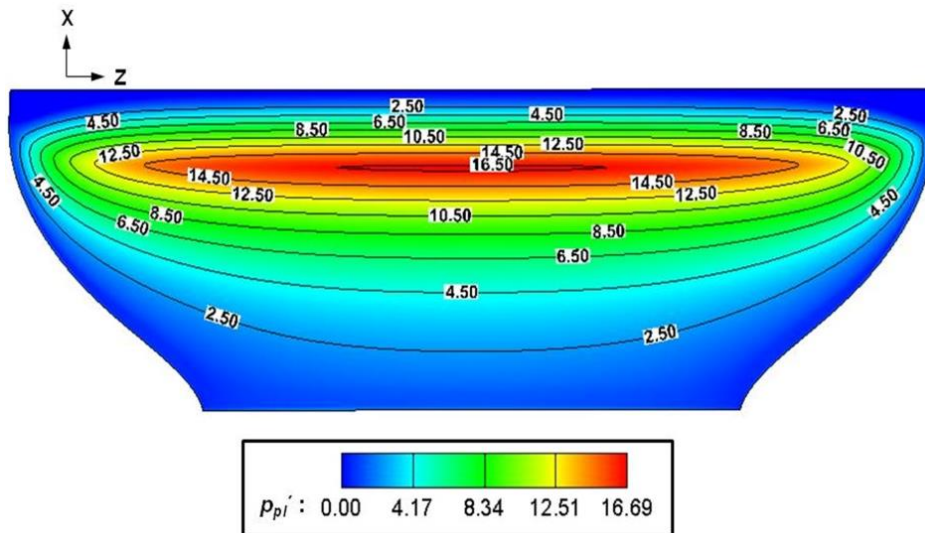
Figure 2-11: Dimensionless pressure contour plots on the x-z symmetry plane of the power-law fluid ($m=5\times10^4$ Pa·s^n, $n=0.35$) for $W_i/2H_o=80$.

fluid ($m=50000$ Pa·s^n, $n=0.35$) as shown in Fig. 2.10 for the case with $W_i/2H_o=80$ and in Fig. 2.11 pressure contours on the x-z symmetry plane are plotted. The pressure contour results presented by Levine et al. [26], show a similar transversal rapid decrease of

29

pressure near the edges. The predicted pressures are also in qualitative agreement with the experimentally measured pressure results reported by Unkrüer [27].

2.4.3 The spiral motion of the melt

In the following we study the motion of fluid particles as they move from the entry plane and through the calender gap to form the calendered sheet. Fig. 2.12 shows the streamlines for a Newtonian fluid (μ=6500 Pa·s). The material is entering the flow domain through line AB, which in Fig. 2.12a is located 5 mm off the *x-y* symmetry plane, whereas in Fig. 2.12b line AB is located 50 mm off the *x-y* symmetry plane (the length of line AB is equal to the entrance thickness of the sheet, $2H_i$). It is evident that material entering at the top and bottom segments of line AB (that is, nearest to the rotating rollers) is taken up by the drag flow and conveyed directly to the exit. However, material entering the domain
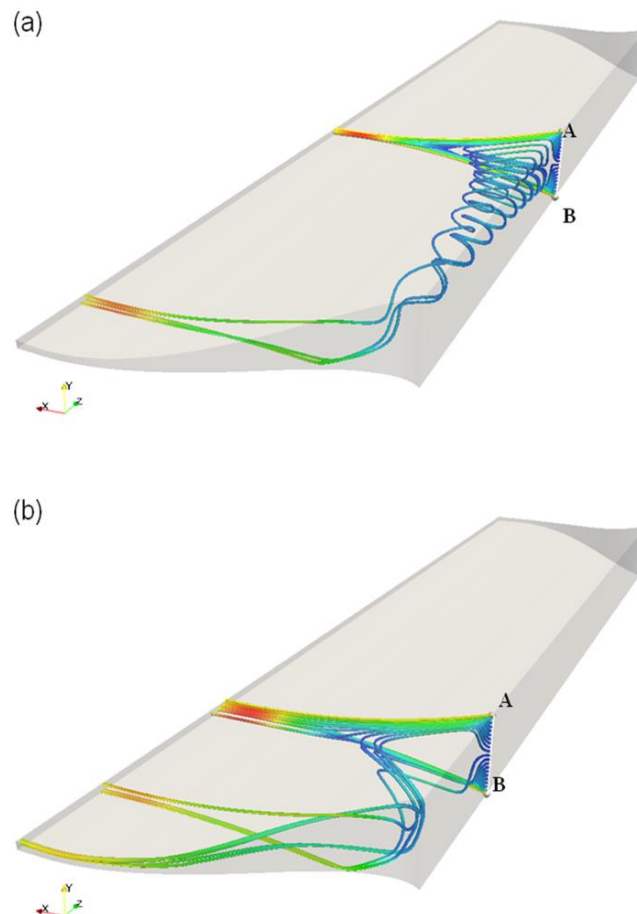
Figure 2-12.: Calculated streamlines for a Newtonian fluid (μ=6500 Pa·s and $W_i/2H_o$=150) starting from a line AB located at (a) 5mm off the *x-y* symmetry plane and (b) 50 mm off the *x-y* symmetry plane.

from the central portion of line AB (e.g. see Fig. 2.12a), appears to progress through a spiral motion in the transverse direction, and exit at the sides of the calendered sheet (see Figs. 2.12a and 2.12b). This spiral motion is evidently the result of the combined action of the recirculation forming behind the nip region and of the transverse pressure gradient discussed earlier, and is therefore a fully 3D motion.

Similar patterns are observed for material entering at other locations off the x–y symmetry plane such as at 15 mm, 30 mm and 50 mm from the symmetry plane (the half width of the sheet at the entrance is $W_i/2=75\text{mm}$). Similar streamlines patterns are observed for the power-law fluid. These results appear to be in qualitative agreement with the experimental observations by Unkrüer [27] for flow within the melt bank. The implications of the spiraling motion of the material from the entrance to the spreading sides could be significant vis-à-vis the prediction of molecular (or fiber) orientation in the calendered product. However, a more striking implication of the flow patterns revealed by Figs. 2.12 and 2.13 is the evident rearrangement of the calendered material. Material at the surface of the fed sheet follows the drag flow near the calender surfaces and ends-up at the corresponding (surface) positions of the produced sheet. This is intuitive and is shown in Fig. 2.13a for the middle section of the calenders (extending from the symmetry plane at $z=0$ to $z=W_f/6$) in which the outer layer of the final calendered sheet is shown to originate from the corresponding outer layer of the fed sheet. Material ending up at the inner layer of that section of the produced sheet ($0<z<W_f/6$) (streamlines marked as red in Fig. 2.13) originates from the feed section's inner layer – this material experiences a small lateral displacement due to the transverse pressure developed (Fig. 2.13a). The analogous streamlines for an intermediate region ($W_f/6 <z<W_f/3$) are shown in Fig. 2.13b. Here the material at the inner layer of the fed sheet experiences a higher lateral displacement than the corresponding material of Fig. 2.13a, but still ends up forming the inner layers of the corresponding section of the produced sheet – while, as in Fig. 2.13a, the surface layer still follows the drag flow and ends up forming the surface of the produced sheet. Examination of Fig. 2.13c however, shows that the material coming off the calenders at the edges of the calendered sheet has originated to a large extent at the inner region of the entire width-span of the fed sheet. It is also interesting to observe in Fig. 2.13c that this material (originating at points in the interior of the fed sheet) ends up predominantly at the surface of the calendered sheet. These results point to an as yet unreported rearrangement of the material during the calendering of a sheet and opens up potentially interesting applications, e.g in the case of the calendering of multi-layer extrusions. It should be noted that 2D

31

computational models (e.g Agassant and Espy [11], Mitsoulis et al. [13]) have demonstrated the existence and extent of the recirculation flow occurring behind the nip
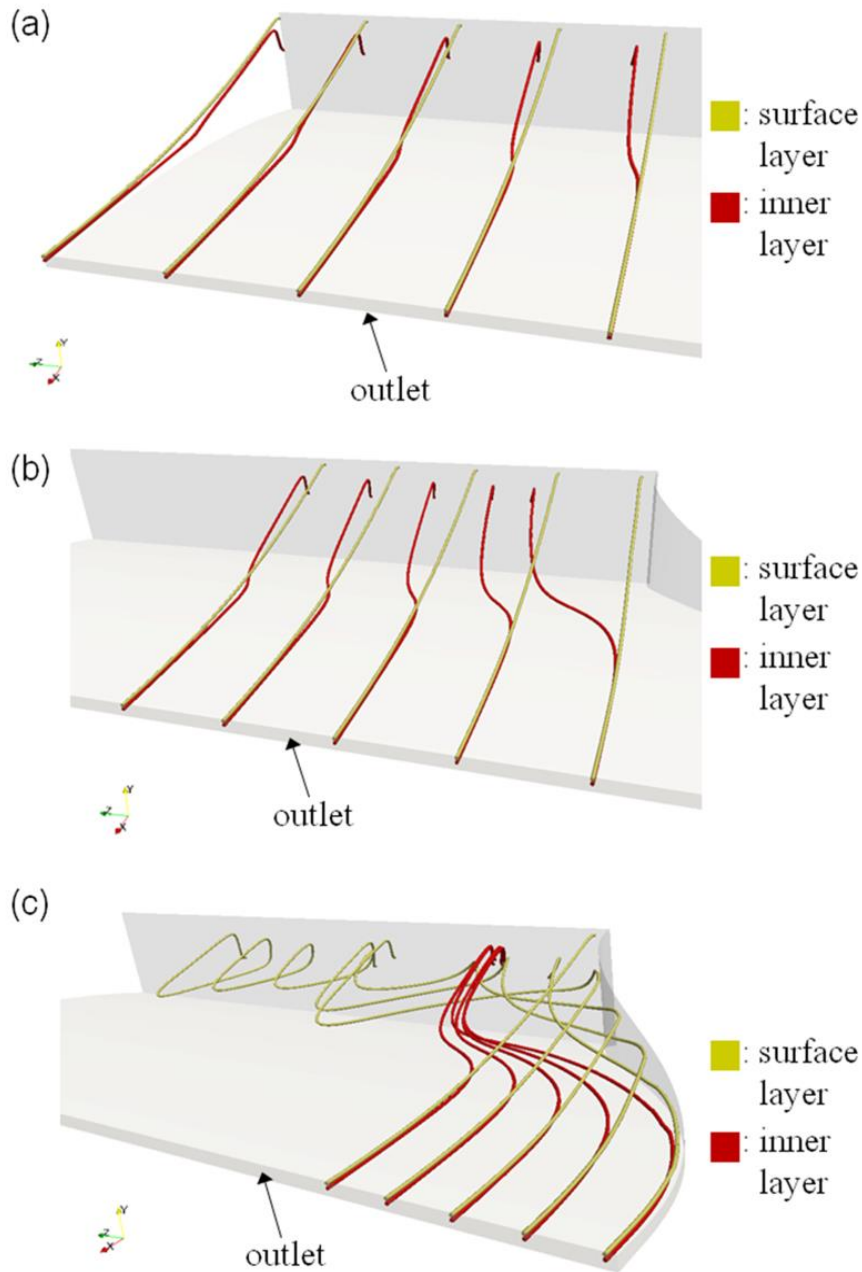
Figure 2-13: Streamlines plotted from the outlet to the inlet for two different sections of the Newtonian calendered material ($W_i/2H_o$=150), with the section close to the calender surface denoted as *surface layer* and the section closer to the *x-z* symmetry plane denoted as *inner layer* with (a) streamlines exiting the flow domain at the region near the middle of the calenders, (b) streamlines exiting at an intermediate region and (c) streamlines at the edge of the calendered sheet (spreading region).

region as well as within the melt bank. However, it is only a fully 3D model, including the presence of deforming side surfaces (spreading), that is capable of predicting the full extent of melt motion as it travels through the calenders. Experimental investigation and confirmation of this is pending, as is an investigation of how the presence of a melt bank might influence these flow patterns.

2.4   Conclusions

We have presented a three-dimensional computational analysis of the calendering process for Newtonian and non-Newtonian materials. The usefulness of earlier unidirectional and two-dimensional analyses notwithstanding, there is no denying the fact that the actual process is three-dimensional and that only a limited number of published studies has been concerned with its 3D features. Of these 3D features we have focused on: (i) the change in the width of the calendered sheet as it passes through the calenders (spreading), (ii) the development of a 3D pressure profile, including a pressure gradient in the transverse direction and (iii) the existence of a spiraling transverse flow pattern of the material in the melt feeding section, as a result of the combined action of recirculation and of the transverse pressure drop. The study reveals that the spreading is affected by (i) the entrance width of the fed sheet (see Fig. 2.5) – the lower the entrance width the higher the spreading while for higher entrance width the spreading ratio declines asymptotically to unity, (ii) the feeding speed of the sheet (see Fig. 2.5) – the higher the feeding speed the higher the spreading and (iii) the thickness of the fed sheet – increasing the thickness the spreading also increases (see Fig. 2.6). Pressure profiles in the transverse direction (z-direction) and at different locations of the machine direction (x-direction) reveal the existence of rapid pressure decrease near the spreading sides and a mild pressure variation in the central region of the calenders. The above-mentioned pressure development in the transverse direction, which is observed for both the Newtonian and power-law material, along with the recirculation occurring behind the nip region, forces the material to flow laterally, following a spiral path. Examination of the flow paths reveals a remarkable material rearrangement from the feeding section to the exit. Material from the skin of the fed sheet (locations close the to the calender surfaces – see Fig. 2.13a and 2.13b) follows the drag flow and exit forming the outer layers of the produced sheet. However, material from the inner part of the fed sheet follows a spiral flow pattern in the transverse direction, ending up at the surface in the region around the edges of the produced sheet.

33

2.5 References

1. R.E. Gaskell, *J. App. Mech.*, **17**, 334 (1950).

2. J.M. McKelvey, *Polymer Processing*, Wiley (1962).

3. S. Middleman, *Fundamentals of Polymer Processing*, McGraw–Hill (1977)

4. I. Brazinsky, H.F. Cosway, C.F. Valle Jr., R. Clark Jones and V. Story, *J. App. Polym. Sci.*, **14**, 2771 (1970).

5. W.W. Alston and K.N. Astill, *J. App. Polym. Sci.*, **17**, 3157 (1973).

6. J. Vlachopoulos and A.N. Hrymak, *Polym. Eng. Sci.*, **20** (11), 725 (1980).

7. S. Sofou and E. Mitsoulis, *Journal of Plastic Film & Sheeting*, **20** (3), 185 (2004).

8. E. Mitsoulis and S. Sofou, *J. App. Mech.*, **73** (2), 291 (2006).

9. C. Kiparissides and J. Vlachopoulos, *Polym. Eng. Sci.*, **16** (10), 712 (1976).

10. C. Kiparissides and J. Vlachopoulos, *Polym. Eng. Sci.*, **18** (3), 210 (1978).

11. J.F. Agassant and M. Espy, *Polym. Eng. Sci.*, **25** (2), 118 (1985).

12. J.F. Agassant, Le Calandrage des Matières Thermoplastiques, Doctoral Thesis, Université Pierre et Marie Curie (1980).

13. E. Mitsoulis, J. Vlachopoulos, and F.A. Mirza, *Polym. Eng. Sci.*, **25**, 6 (1985).

14. M.C. Peck, S.L. Rough and D.I. Wilson, *Ind. Eng. Chem.*, **44**, 4099 (2005).

15. N. Kim and S. Kobayashi, *Int. J. Mach. Tools Manuf.*, **30**, 269, (1990).

16. S.M. Hwang, M.S. Joun and Y.H. Kang, *Transactions of the ASME: Journal of Engineering for Industry*, **115**, 290 (1993).

17. E.N. Dvorkin, M.B. Goldschmit, M.A. Cavaliere, P.M. Amenta, O. Marini and W. Stroppiana, *J. Mater. Process Tech.*, **68**, 99 (1997).

18. J.D. Lee, *Comp. Met. App. Mech. Eng.*, **161**, 315 (1998).

19. K. Komori, *Int. J. Mech. Sci.*, **40**, 479 (1998).

20. Z.Y. Jiang and A. Tieu, *J. Mater. Process Tech.*, **112**, 144 (2001).

21. X. Duan and T. Sheppart, *Int. J. Mech. Sci.*, **44**, 2155 (2002).

22. Z.Y. Jiang, A.K. Tieu, X.M. Zhang, C. Lu and W.H. Sun, *J. Mater. Process Tech.*, **140**, 542 (2003).

23. T. Matsumiya and M.C. Flemings, *Metallurgical Transactions B*, **12**, 17 (1981).

24. R.E. Johnson, *Int. J. Mech. Sci.*, **33** (6), 449 (1991).

25. S. Sezek, B. Aksakal, and Y. Can, *Materials and Design*, **29**, 584 (2008).

26. L. Levine, C.M. Corvalan, O.H. Campanella and M.R. Okos, *Chem. Eng. Sci.*, **57**, 643, (2002).

27. W. Unkrüer, Beitrag zur Ermittlung des Drucksverlaufes und der Fliessvorgange im Walzspalt bei der Kalanderverarbeitung von PVC Hart zu Folien, Doctoral Thesis, Technische Hochschule Aachen (1970).

28. S. Luther and D. Mewes, *Polym. Eng. Sci*. **44** (9), 1642 (2004).

29. S.V. Patankar and D.B. Spalding, *Int. J. Heat Mass Transfer*, **15** (10), 1787 (1972).

Chapter 3

A Study on the Effect of Drawing on Extrudate Swell in Film Casting

(Published in: *Applied Rheology*, **25**, 42425, 2015)

Abstract

We present a numerical study of the film casting process, with a focus on the effect of the draw ratio on the swelling of the extruded sheet. So far, studies regarding film casting have dealt mainly with the phenomenon of neck-in and have neglected swelling of the material as it emerges from the die lips. Knowledge of the amount of swelling is important for accurate determination of the effect of stretching and orientation phenomena. The problem is tackled by studying the gap-wise swelling of the sheet or film as it emerges from a wide rectangular die and is subsequently drawn down under different draw ratios. The material is treated as viscoelastic by utilizing the Linear Phan Thien-Tanner (LPTT) model. Newtonian simulations are also carried out. A decoupled iterative algorithm is used for the determination of the shape of the extruded sheet, based on the fact that the sheet's surfaces belong to streamlines. Our results are in qualitative agreement with results in the literature, with the latter being limited in number and available mainly for the (similar) process of fiber melt spinning.

3.1 Introduction

Film casting is a very important industrial process for the production of plastic film, sheet or tape that finds applications in a wide range of technologies, such as in food packaging, automotive, housing and agriculture. In the process of film casting, the polymer melt extruded from a flat or a slit die is stretched in the machine direction (flow direction) by coming in contact with a roller, often of controlled temperature, which rotates at higher speed (the take-up or draw-down speed) than the speed of the extruded material. The extent of imposed stretch is quantified by the drawing ratio *DR*, which is the ratio of the take-up speed to the average velocity of the melt at the die exit. This speed differential leads to the formation of a sheet of reduced width through a mechanism called neck-in, along with higher thickness near the side edges (edge-beading).

36

In film casting, as well as in other similar industrial processes (e.g. melt spinning), the emerging polymer has the tendency to locally swell near the die exit (extrudate swell).The extrudate or die swell problem itself, in the absence of a take-up roller has been extensively studied, for Newtonian as well as viscoelastic fluids emerging from planar or axisymmetric dies, experimentally, theoretically and numerically [1-9]. Specific to film casting, several studies have also studied the neck-in and to a far lesser extent the edge-beading effects - experimentally or utilizing, theoretical, 1D, 2D and 3D numerical schemes [10-21]. These have offered useful insights concerning the different parameters affecting the process with the most important one being the draw ratio *DR*, the value of which defines the dimensions, shape and properties of the final product. The stretching of the extruded sheet caused by the rotation of the chill roll results in the formation of a product the dimensions of which are reduced compared to the dimensions of the die lip exit. For instance, in film casting the thickness of the extruded sheet is lower than the gap of the rectangular die and in melt spinning the extruded fiber's radius is lower than the radius of the round extrusion orifice or spinneret. However, immediately after the material exits the die it has the tendency to swell, significantly for very elastic melts, and the dimensions of the product, at this location, are generally higher than the dimensions of the die gap. This swelling behavior, in the presence of drawing, has been neglected in the technical literature, even though it is of practical significance as it directly determines the mechanical and stress-relaxation history of the sheet prior to its eventual stretching by the rolls.

While no comparable studies exist for film casting, a small number of studies exist concerning the prediction of swelling under stretching conditions of the extrudate for the process of wet or melt spinning. White et al. [22] studied experimentally and theoretically the melt spinning of fibers by taking photographs of the melt as it emerged from a capillary die. Their results indicate a trend of rapid decrease in the amount of swelling with increasing take-up speed (and take-up force). Keunings et al. [23] studied melt spinning of viscoelastic liquids numerically, using Newtonian as well as Maxwell, Oldroyd-B, and Phan Thien-Tanner (PTT) viscoelastic fluid models. Their results indicate a decrease in swelling by increasing the value of the imposed stretching force. Leonov et al. [24] studied theoretically and experimentally the shape of the swelling and the stretching of an elastic jet emerging from a capillary die. They determined the shape of free swelling of polyisobutylene under three different wall shear stress conditions. For each condition, they applied the same constant axial stretching force corresponding to 0.7×10^4 Pa on the free

37

swelled jet. Their experimental results and theoretical predictions, on the basis of the measured and calculated extrudate profiles, indicate that the applied force reduces the swelling of the jet at each different value of the wall shear stress. A more recent experimental study by Ouyang et al. [25] shows how the jet stretch in the process of wet spinning affects the swelling behavior of an extruded fiber. Specifically, the study concerns the jet swell of polyacrylonitrile (PAN) fibers extruded through a spinneret of 3000 holes (with 65 μm diameter each) under different stretching conditions. For free swelling the fiber average diameter was 114 μm as measured by the Micro-Image Analysis and Processing Software (MIAPS). They report that the diameter of the fibers decreased significantly with increased stretching. It is also interesting to note that in the recent numerical and experimental work of Widjojo et al. [26] - study of the die swell in the hollow fiber spinning process of hyperbranched polyethersulfone (HPES) via different spinneret designs - they report that the die swell can be reduced prominently when a higher take-up speed spinning is applied on the hollow fiber.

Reduced swelling has also been observed in the presence of gravitational forces. While in melt spinning the swelling reduction is caused by increasing the take-up speed of the rollers, gravitational forces also lead to a reduced swelling. This was reported in the experimental study of Trang et al. [27] who measured the swelling of Newtonian and viscoelastic jets under the effect of the gravitational body force expressed through the Stokes number. Their extensive results concerning the shape/profile of the elongated jet indicate that for higher values of the Stokes number the swelling is reduced. A correlation between jet swell and Stokes number can be found in the finite element study performed by Mitsoulis et al. [28] for various factors affecting the Newtonian axisymmetric and planar extrudate swell. Among other results they indicate a trend: that gravitational forces acting in the direction of the flow cause a rapid decrease of the extrudate swell for relatively small values of the Stokes number.

In the area of sheet extrusion, the only known study so far that includes both, swelling and stretching is that by Kwon [29], who used an 1D approach to derive an analytical expression for the shape of the extruded/stretched sheet. The viscoelastic behavior of the material was expressed by the Leonov viscoelastic model. The author provided results for the shape of the extruded sheet for one single value (i.e. under a single drawing condition) of the applied stretching force corresponding to σ_o=6000 Pa.

From the above survey it is evident that the exact effect of drawing speed on melt swelling in the process of film casting has not been adequately studied. The scope of the

38

present work is to fill this gap and specifically focus on how much the maximum swelling is affected by different *DR* values in the process of film casting. For this reason, and to include the partially elastic nature of the melt, we utilize the linear PTT viscoelastic model for a single relaxation mode. Simulations regarding the material as Newtonian were also carried out. The shape of the extruded sheet is computed under different stretching conditions (*DR* up to 6) or free swelling (*DR*=1) for both classes of fluids.

3.2   Problem Formulation

The flow is assumed to be steady-state, creeping, isothermal and incompressible. The governing equations utilized in the present study are the continuity equation

$$\nabla \cdot \mathbf{U} = 0 \tag{3.1}$$

and the momentum equation in the absence of fluid inertia (Stokes equation)

$$0 = -\nabla p + \nabla \cdot \boldsymbol{\tau} \tag{3.2}$$

where $\mathbf{U}$ is the velocity vector, p the pressure and $\boldsymbol{\tau}$ the total stress tensor, which is split into a purely viscous component (often termed the "Newtonian solvent contribution") $2\eta_s \mathbf{D}$ and the contribution of the polymeric macromolecules $\boldsymbol{\tau}_p$, as

$$\boldsymbol{\tau} = 2\eta_s \mathbf{D} + \boldsymbol{\tau}_p \tag{3.3}$$

where η_s is the solvent viscosity and $\mathbf{D} = 1/2\left(\nabla \mathbf{U} + \left(\nabla \mathbf{U}\right)^T\right)$ is the rate of deformation. The elastic nature of the polymer melt is expressed through the viscoelastic part of the stress, namely $\boldsymbol{\tau}_p$. The constitutive equation governing the viscoelastic part of the stress utilized in the present study is the linear Phan Thien-Tanner (LPTT) model for a single relaxation mode

$$\left[1 + \frac{\varepsilon \lambda}{\eta_p} tr\left(\boldsymbol{\tau}_p\right)\right]\boldsymbol{\tau}_p + \lambda \overset{\diamond}{\tau}_p = 2\eta_p \mathbf{D} \tag{3.4}$$

where $\overset{\diamond}{\tau}_p$ is the Gordon-Schowalter convected derivative which is usually defined as [30]

$$\overset{\diamond}{\tau}_p \cong \frac{D\boldsymbol{\tau}_p}{Dt} - \boldsymbol{\tau}_p \cdot \nabla \mathbf{U} - \nabla \mathbf{U}^T \cdot \boldsymbol{\tau}_p + \xi\left(\boldsymbol{\tau}_p \cdot \mathbf{D} + \mathbf{D} \cdot \boldsymbol{\tau}_p\right) \tag{3.5}$$

In Eqs 3.4 and 3.5 η_p is the polymer viscosity, λ is the relaxation time, the ξ parameter is related to the slip of the molecular network with respect to the macroscopic motion of the continuous medium and the parameter ε imposes an upper limit to the elongational viscosity.

39

A schematic of the geometry studied is shown in Fig. 3.1. The downstream direction is denoted as the *z*-direction while *x*-direction corresponds to the thickness of the extrudate. We assume that the thickness of the emerging sheet varies in the downstream direction and we neglect any reduction of the sheet width downstream (neck-in) as well as the edge-beading phenomenon.
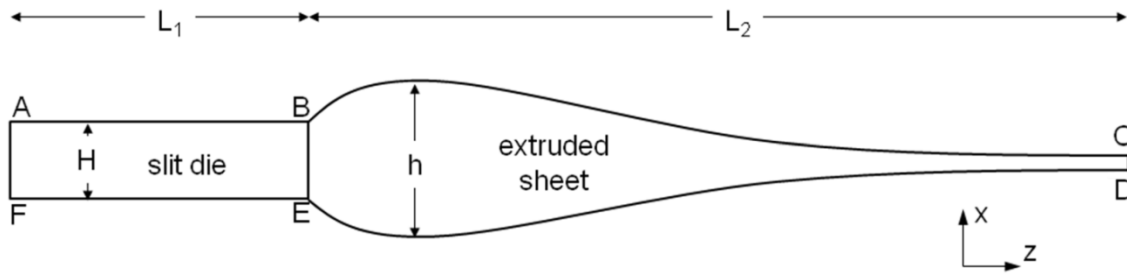
Figure 3-1: (a) Schematic representation of the drawn extrudate geometry with L_1 the length of the die, L_2 the length of the stretched extrudate, H the gap of the die and h the maximum thickness of the sheet. The drawing speed V_R is applied on the boundary CD.

The length of the die L_1, the length of the extrudate L_2 and the gap of the die H shown in Fig. 3.1, were kept constant in the simulations for which $L_1/H=10$ and $L_2/H=30$. The amount of maximum swelling is expressed through

$$\chi = \frac{h}{H} \tag{3.6}$$

where H is the die gap and h is the maximum thickness of the extruded and subsequently stretched sheet (Fig. 3.1). The same definition is also valid in the cases of free swelling. The drawing ratio *DR* is defined as

$$DR = \frac{V_R}{\overline{V}} \tag{3.7}$$

where V_R is the take-up speed of the roller and $\overline{V}$ the average velocity of the fully developed velocity profile. The following boundary conditions apply (with reference to Fig. 3.1):

a. Neglecting any surface tension effects at the free surfaces BC and ED we set $\mathbf{n}\cdot\boldsymbol{\tau}=0$ and $\mathbf{n}\cdot\mathbf{U}=0$ where $\mathbf{n}$ is the outward unit normal vector to the free surface.

b. At the die inlet we set a uniform velocity profile V_d and a zero value for the total stress tensor $\boldsymbol{\tau}$ (within a short distance the velocity profile becomes fully developed and does not influence the results at the exit of this $L_1/H=10$ die).

40

c. At the outflow boundary CD we set a prescribed velocity, namely V_R, which corresponds to the take-up speed of the roller.

d. At the die walls, AB and FE the usual no-slip boundary condition applies.

In Eq. 3.7 above, the average velocity of the fully developed velocity profile is equal to the velocity prescribed at the die inlet ($\overline{V} = V_d$), since mass is conserved. As this value was held constant throughout the different numerical experiments, different DR values were obtained by modifying the velocity at the CD boundary, V_R.

3.3 Numerical Procedure

For the solution of the continuity equation (Eq. 3.1) and the momentum equation (Eq. 3.2), we use the OpenFOAM (Open Source Orientation and Manipulation) package, which is based in the Finite Volume Method (FVM). The FVM subdivides the flow domain into a finite number of smaller control volumes (cells) (see Fig. 3.2a). The size of the flow domain in Fig. 3.2a (16000 cells) was chosen based on the mesh convergence with different mesh arrangements. It is well-known that in the expansion point, point B and E in Fig. 3.1, a critical singularity takes place when determining the amount of free swell, which requires special treatment. To tackle this problem we impose a necessary local refinement of the edges near the expansion point [8] as shown in Fig. 3.2b. The mesh convergence study is presented in section 3.4.

3.3.1 Determination of the Free Surface

The numerical determination of the shape of the extrudate is achieved via a decoupled iterative procedure - the same technique used by Polychronopoulos et al. [31] to predict the shape and the spreading amount of a sheet in the calendering process. We assume that the final shape of the free surface of the sheet may vary only in the *x*- and *z*-directions, and that the top and bottom surfaces of the sheet are streamlines, on each point of which the ratio of the velocities in the *x* and *z* directions equals the slope of the free surface, namely

$$\frac{dx}{dz} = \frac{u}{w} \tag{3.8}$$

where *u* and *w* are the velocity components in the *x* and *z* directions respectively and *dx/dz* is the local slope of the free surface. Determination of the extruded sheet's shape is achieved through a decoupled iterative algorithm in which the shape (line *x=x(z)*) at each
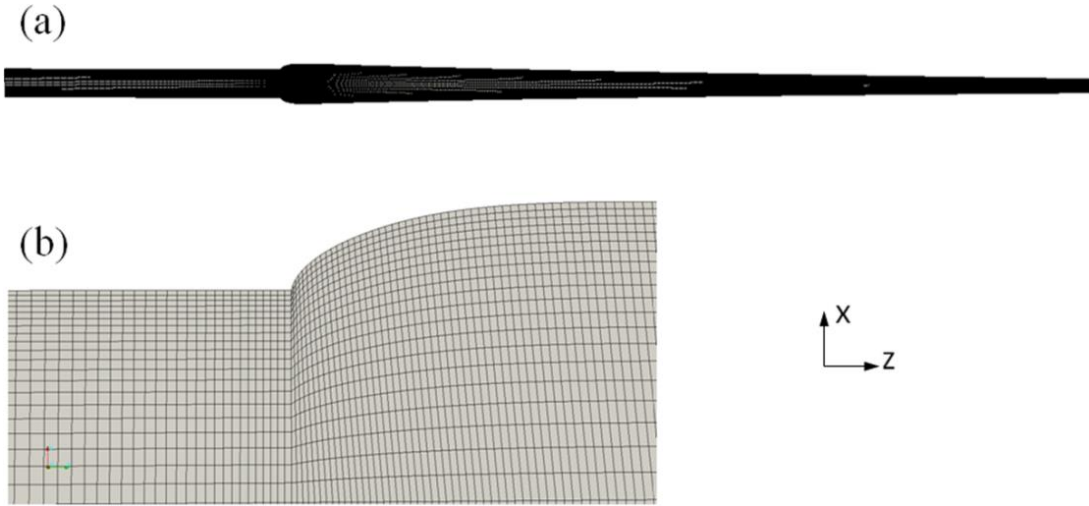
Figure 3-2: Computational flow domain (16000 cells) for *DR*=2, (a) entire domain and (b) magnified view of the domain near the die exit.

iterative step is obtained by integration of Eq. 3.8, utilizing the velocity field (*u,w*) determined from solution of Eqs. 3.1, 3.2 and 3.4 at the previous step. The starting point is a sheet of uniform thickness. The speed of convergence to the final extrudate shape is improved by using a relaxation procedure

$$\tilde{\mathbf{x}}^{s+1} = (1-\kappa)\mathbf{x}^{s+1} + \kappa\mathbf{x}^{s}$$ (3.9)

with relaxation factors κ (0.4<κ<0.9) where $\tilde{\mathbf{x}}^{s+1}$ the *x*-coordinate vector at the sth iteration. Convergence is finally obtained when the velocities *u,w* and the obtained extrudate shape *x=x(z)*, satisfy Eq. 3.8 so that the sum of the squares of errors is less than a prescribed tolerance of $e=10^{-4}$. The speed of convergence for the stretched sheet is further enhanced by assuming, as an initial configuration for each *DR* value, the convergent extrudate shape corresponding to the previous *DR* value. This continuation approach reduced the number of iterations required for convergence at each DR and extended the range of convergence.

3.4   Results and Discussion

In the present study, the parameters of the LPTT model were chosen to be those used by Bush et al. [3] and Karapetsas and Tsamopoulos [8], namely η_s/η_p =0.08, λ=1 s, ξ=0, ε=0.008 A mesh convergence study of the numerical solution was carried out utilizing four different mesh arrangements as shown in Table 3.1, in which the density of the cells was increased from M1 (6000 cells) to M4 (20240 cells). In the Newtonian case without drawing, denser mesh configurations lead to a slightly reduced estimate of swelling χ of the well accepted value of χ=1.19. This trend is also reported in the numerical studies

42

carried out by Georgiou et al [5] and Mitsoulis et al [28] for planar Newtonian free swell. All the employed meshes were non-uniform and refined with smaller cells at the die exit. The results exhibit a satisfactory convergence for the present purposes and all subsequent calculations were carried out for the M3 mesh arrangement.

Mesh	Number of cells	χ (LPTT)	χ, DR=3 (LPTT)	χ (Newtonian)	χ, DR=3 (Newtonian)
M1	6000	1.654	1.338	1.189	1.117
M2	10800	1.692	1.353	1.186	1.115
M3	16000	1.715	1.375	1.182	1.111
M4	20240	1.721	1.382	1.179	1.109

Table 3-1: Effect of mesh size on free swell and swell under drawing (Newtonian and LPTT model).

It should be pointed out that in planar or axisymmetric extrudate swell problems for Newtonian or viscoelastic fluids, typically a fully developed velocity profile is prescribed at the entry of the die (e.g. [3],[8],[28]). The present work, as mentioned in an earlier section, adopts a flat velocity profile at the entrance. Our simulations indicate that the Newtonian velocity profile becomes fully developed at less than $0.5H$ from the entrance and for the L-PTT fluid becomes fully developed at less than $1.9H$. This means that we have at least a length of $8H$ of fully developed flow.

The numerical predictions for DR=1 were also compared to available models for χ. Based on the theory of elastic recovery of a Maxwell Fluid, the free swell of a planar extrudate emerging from a slit die may be calculated by Tanner's equation [1]

$$\chi = 0.19 + \left[1 + \frac{1}{3}S_R^{\,2}\right]^{1/4} \tag{3.10}$$

or, following the theory of rubber elasticity by Malkin et al. [2], the free swell from a slit die may be expressed as

$$S_R^{\,2} = 5\left[\chi^2 + \frac{2}{\chi} - 3\right] \tag{3.11}$$

In Eqs. 3.10 and 3.11, S_R is the recoverable shear given by $S_R = N_{1,w}/2\tau_w$ where $N_{1,w} = \tau_{xx} - \tau_{zz}$ corresponds to the first normal difference and $\tau_w = \tau_{xz}$ the shear stress. The

43

w index in both of these values implies that they are evaluated at the wall of the die far upstream. In the present case, for the chosen LPTT viscoelastic parameters, the recoverable shear determined by the numerical simulation is S_R=2.297. It is interesting to note that substitution of this value in Eq. 3.10 gives χ=1.4795 or swelling of 47.95%, while substitution in Eq. 3.11 gives χ=1.697 or swelling of 69.7%.

The excess pressure losses at the die exit (exit correction) n_{ex} is defined as

$$n_{ex} = \frac{\Delta P_{ex}}{2\tau_w} \tag{3.12}$$

where ΔP_{ex} is the pressure at the slit die exit. For the Newtonian fluid we obtain from the simulations n_{ex}=0.158 which is very close to the value obtained by Reddy and Tanner [32] and Mitsoulis et al. [33] of n_{ex}=0.155. For the L-PTT fluid we obtained from the simulations n_{ex}=0.898. Reddy and Tanner [32] provided an equation for a Second-Order Fluid that relates the excess pressure losses n_{ex} with the recoverable shear S_R as

$$n_{ex} = 0.26 S_R + 0.155 \tag{3.13}$$

As mentioned earlier S_R=2.297 and consequently Eq. 3.13 gives n_{ex}=0.752.
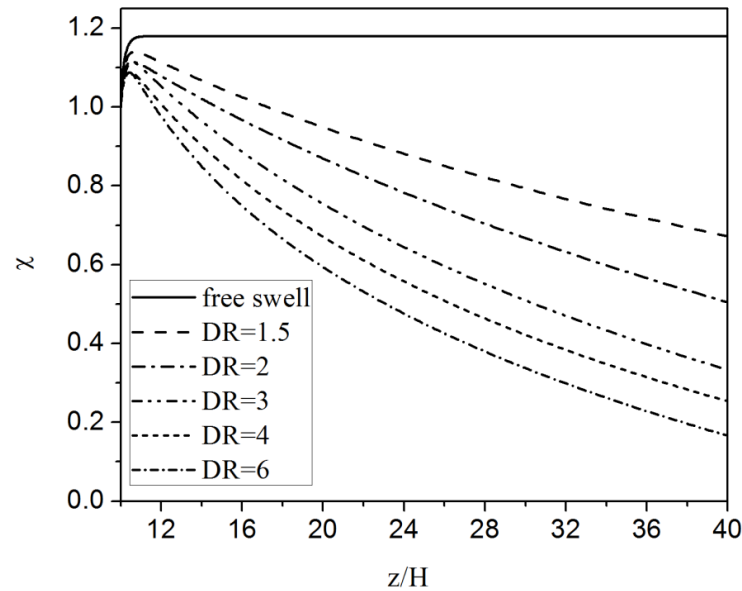
Figure 3-3: Shape of the upper half of the extruded sheet for free swell as well as under drawing. Newtonian material.

The extrudate shapes for different *DR* values are shown in Fig. 3.3 for the Newtonian material and in Fig. 3.4 for the LPTT viscoelastic model, where the upper half of the extruded sheet is presented. Fig. 3.5 shows the free surface shape close to the expansion point, ranging from the die exit (located at *z/H*=10) to *z/H*=12 for the viscoelastic case. Following a similar drawing ratio range used in the experimental and theoretical film casting study by Pol et al [20], in our study the examined *DR* values ranged from *DR*=1, which corresponds to free swelling, to *DR*=6. For free swelling, the
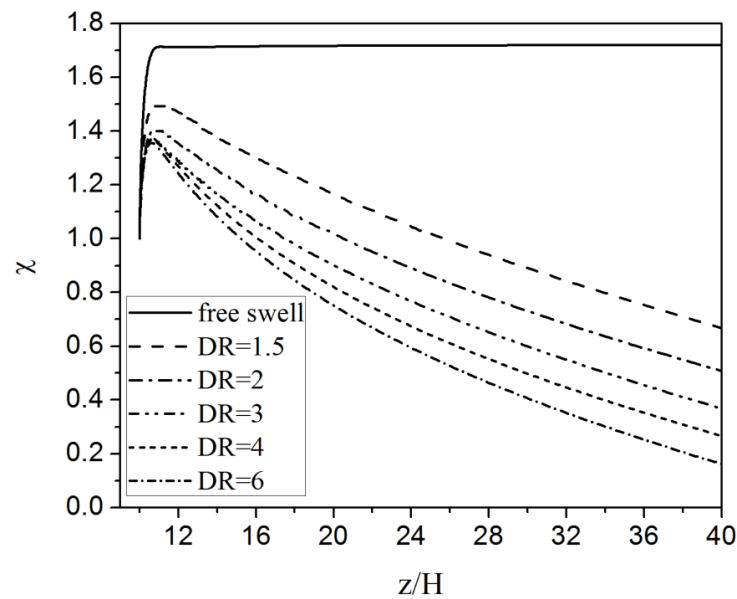
Figure 3-4: Shape of the upper half of the extruded sheet for free swell as well as under drawing. LPTT model.

thickness of the extrudate increases upon exit from the die, until a maximum value (χ=1.715) is reached; this is the final thickness of the extruded sheet. As the drawing ratio is increased, the amount of maximum swell as well as the final thickness of the sheet decrease. Our free surface shapes are similar to the one shape reported by Kwon [29] – which was obtained by imposing a value of σ_o=6000 Pa at the take-up point. Although the present study deals with film casting, it is worth noting that the obtained shapes are also similar to the numerically obtained shapes by Keunings et al. [23] or the analytically calculated shapes by Leonov et al. [24] for the, in principle similar, process of melt spinning. Similar convergent shapes for the same *DR* values were also calculated for the Newtonian case. We also notice that the location of the maximum thickness of the

45
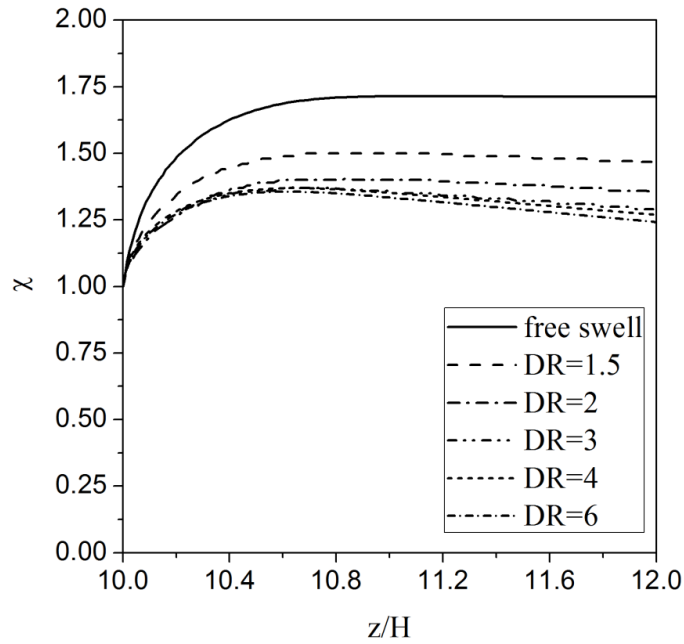
Figure 3-5: Shape of the upper half of the extruded sheet near the die exit, for free swell as well as under drawing. LPTT model.
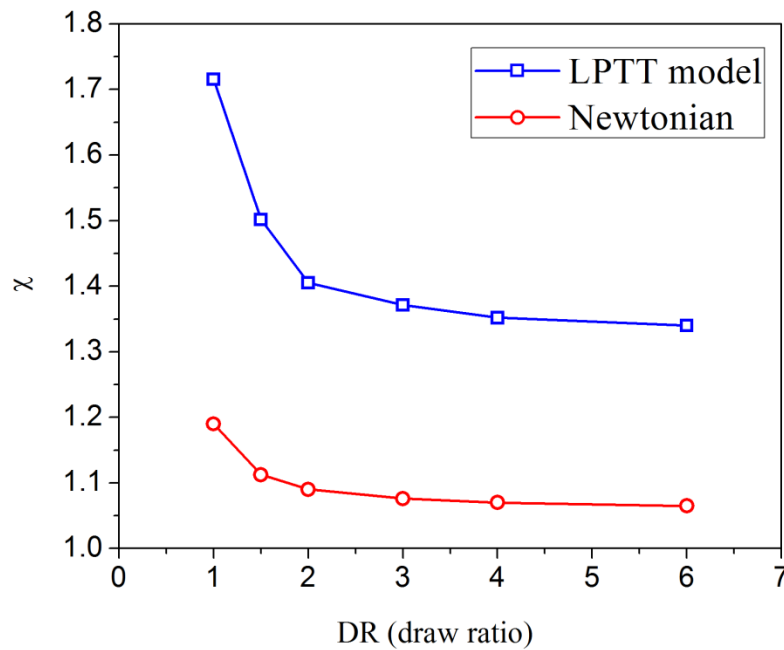
Figure 3-6: Effect of the drawing ratio on the maximum swell of the sheet for the Newtonian case and the viscoelastic LPTT fluid.

extruded sheet in the z-direction remains largely unaffected by increasing DR. Fig. 3.6 plots the predicted swell χ against the imposed drawing ratio DR. It is interesting to observe that as the extruded sheet is stretched the maximum swelling *decreases rapidly* from 1.715 to the value of 1.375 for $DR=2$. For higher drawing speeds χ decreases

46

asymptotically. The results for the Newtonian fluid are also shown in Fig. 3.6, with the maximum free swell of $\chi=1.1825$ asymptotically decreasing to $\chi=1.06$ for $DR=6$. These trends are in qualitative agreement with the experimental observations by White et al. [22] and by Ouyang et al. [25] for the similar process of wet spinning.

When the extruded sheet or film freely swells as it emerges from the slit die, it will leave the die with a velocity V_s (at the point of maximum swell) which is considerably lower than the average velocity $\bar{V}$ of the fully developed velocity profile. The velocity V_s at the location of maximum swelling for the LPTT fluid shown in Fig. 3.4 and Fig. 3.5, is 30%~40% smaller than the average velocity $\bar{V}$, and it is expected to be even smaller for more elastic fluids, which may exhibit swelling ratios perhaps up to 4. This suggests that any subsequent correlations or calculations regarding orientation stretching and determination of crystallinity, as for example by Lamberti et al [34], should use the ratio of the take-up speed V_R over the velocity at the maximum swell V_s rather than the average velocity at the die exit. Consequently, the actual draw ratio will be higher than the drawing ratio defined by Eq. 3.7 and frequently encountered in film casting and melt spinning analyses in the technical literature. This suggestion is fully in agreement with a proposal by Paul [35] that V_R/V_s is "*a more realistic parameter*" for describing the orientation stretching in (acrylic) fiber formation by the process of wet spinning.

3.5   Concluding Remarks

We presented two dimensional numerical results on how the maximum swelling of a sheet or film emerging from a slit die is affected by different drawing speeds for the process of film casting, neglecting the neck-in and edge beading formation. Two cases were examined: (a) Newtonian and (b) viscoelastic LPTT model as the constitutive equation. The extrudate shape was obtained via a decoupled iterative scheme by assuming that the top and bottom surfaces of the sheet lie on streamlines. The numerical results, for the viscoelastic case, indicate a *rapid decrease* of the maximum amount of swell as the drawing ratio increases. Similar behavior for a Newtonian fluid was also reported. However, a certain amount of swelling persists near the die exit even at drawing ratios of 6. Expressing the draw ratio in terms of the velocity at the point of the sheet's maximum thickness may give a more realistic picture of the process especially when any subsequent orientation stretching calculations are involved. The obtained results are in qualitative agreement with experimental, numerical and analytical studies for the (similar) processes of melt and wet spinning.

3.6 References

1. Tanner RI: A Theory of Die-Swell, Journal of Polymer Science Part A2 8 (1970) 2067-2078.

2. Malkin AY, Goncharenko VV, Malinovskii VV: Barus Effects in Polymer Flows Through Cylindrical and Flat Dies, Polymer Mechanics 12 (1976) 439-444.

3. Bush MB, Tanner RI., Phan-Thien N: A Boundary Element Investigation of Extrudate Swell, J. Non-Newt. Fluid Mech. 18 (1985) 143-162.

4. Luo XL, Mitsoulis E: Memory Phenomena in Extrudate Swell Simulations for Annular Dies, J. Rheol. 33 (1989) 1307-1326.

5. Georgiou GC, Boudouvis AG: Converged Solutions of the Newtonian Extrudate Swell Problem, Int. J. Numer. Meth. Fluids 29 (1999) 363-371.

6. Manas-Zloczower I, Nithi-Uthai N: Numerical Studies on the Effect of Constitutive Model Parameters as Reflecting Polymer Molecular Structure on Extrudate Swell, Appl. Rheol. 12 (2002), 252-259.

7. Mitsoulis E: Annular Extrudate Swell of Pseudoplastic and Viscoplastic Fluids, J. Non-Newtonian Fluid Mech. 141 (2007) 138-147.

8. Karapetsas G, Tsamopoulos J: Steady Extrusion of Viscoelastic Materials from an Annular Die., J. Non-Newt. Fluid Mech. 154 (2008) 136-152.

9. Saadat A, Nazockdast H, Sepehr F, Mehranpoor M: Viscoelastic Modeling of Extrudate Swell of Acrylonitrile-Butadiene-Styrene/Clay Nanocomposite, Appl. Rheol. 23 (2013) 12131.

10. Dobroth T, Erwin L: Causes of Edge Beads in Cast Films, Polym. Eng. Sci. 26 (1986) 462-467.

11. d'Halewyu S, Agassant JF, Demay Y: Numerical Simulation of the Cast Film Process, Polym. Eng. Sci. 30 (1990) 335-340.

12. Alaie SM, Papanastasiou TC: Film Casting of Viscoelastic Liquid, Polym. Eng. Sci. 31 (1991) 67-75.

13. Sakaki K, Katsumoto R, Kajiwara T, Funatsu K: Three-Dimensional Flow Simulation of a Film-Casting Process, Polym. Eng. Sci. 36 (1996) 1821-1831.

14. Silagy D, Demay Y, Agassant JF: Numerical Simulation of the Film Casting Process, International Journal for Numerical Methods in Fluids 30 (1999) 1-18.

15. Beaulne M. Mitsoulis E: Numerical Simulation of the Film Casting Process, Intern. Polym. Proc. XIV 3 (1999) 261-275.

16. Lamberti G, Titomanlio G, Brucato V: Measurement and Modeling of the Film Casting Process 1. Width Distribution along Draw Direction, Chem. Eng. Sci. 56 (2001) 5749-5761.

17. Shin DM, Lee JS, Kim JM, Jung HW, Hyun JC: Transient and Steady-State Solutions of 2D Viscoelastic Non-isothermal Simulation Model of Film Casting Process via Finite Element Method, J. Rheol. 51 (2007) 393-407.

18. Zheng H, Yu W, Zhou C, Zhang H: Three-Dimensional Simulation of Viscoelastic Polymer Melts Flow in a Cast Film Process, Fibers and Polymers 8 (2007) 50-59.

19. Shiromoto S, Masutani Y, Tsutsubuchi M, Togawa Y, Kajiwara T: A Neck-In Model in Extrusion Lamination Process, Polym. Eng. Sci. 50 (2010) 22-31.

20. Pol HV, Thete SS, Doshi P, Lele AK: Necking in Extrusion Film Casting: The Role of Macromolecular Architecture, J. Rheol. 57 (2013) 559-583.

21. Shiromoto S: The Mechanism of Neck-in Phenomenon in Film Casting Process, Intern. Polym. Proc. XXIX, 2 (2014) 197-206.

22. White JL, Roman JF: Extrudate Swell During the Melt Spinning of Fibers-Influence of Rheological Properties and Take-up Force, J. Appl. Pol. Sci. 20 (1976) 1005-1023.

23. Keunings R, Crochet MJ, Denn MM: Profile Development in Continuous Drawing of viscoelastic Liquids, Ind. Eng. Chem. Fundam. 22 (1983) 347-355.

24. Leonov AI, Prokunin AN: On the Stretching and Swelling of an Elastic liquid Extruded from a Capillary Die, Rheologica Acta 23 (1984) 62-69.

25. Ouyang Q, Chen YS, Zhang N, Mo GM, Li DH, Yan Q: Effect of Jet Swell and Jet Stretch on the Structure of Wet-Spun Polyacrylonitrile Fiber, J. Macromolecular Sci. B 50 (2011) 2417-2427.

26. Widjojo N, Chung TS, Arifin DY, Weber M, Warzelhan V: Elimination of Die Swell and Instability in Hollow Fiber Spinning Process of Hyperbranched Polyethersulfone (HPES) via Novel Spinneret Designs and Precise Spinning Conditions, Chem. Eng. J. 163 (2010) 143-153.

27. Trang CT, Yeow YL: Extrudate Swell of Newtonian and non-Newtonian Fluids-The Effect of Gravitational Body Force, J. non-Newt. Fluid Mech. 20 (1986) 103-116.

28. Mitsoulis E, Georgiou GC, Kountouriotis Z: A Study of Various Factors Affecting Newtonian Extrudate Swell, Computers & Fluids 57 (2012) 195-207.

29. Kwon Y: One-Dimensional Modeling of Flat Sheet Casting or Rectangular Fiber Spinning Process and the Effect of Normal Stresses, Korea-Australia Rheology Journal 11 (1999) 225-232.

30. Alves MA, Pinho FT, Oliveira PJ: Study of Steady Pipe and Channel Flows of a Single-Mode Phan-Thien–Tanner Fluid, J. Non-Newtonian Fluid Mech. 101 (2001) 55-76.

31. Polychronopoulos ND, Sarris IE, Papathanasiou TD: 3D Features in the Calendering of Thermoplastics: A Computational Investigation, Polym. Eng. Sci. 54 (2014) 1712-1722.

32. Reddy KR, Tanner RI: Notes: On the Swelling of Extrudate Plane Sheets, J. Rheol. 22 (1978) 661-665.

33. Mitsoulis E, Vlachopoulos J, Mirza FA: Numerical Simulation of Entry and Exit Flows in slit Dies, Polym. Eng. Sci. 24 (1984) 707-715.

34. Lamberti G, Brucato V: Real-Time Orientation and Crystallinity Measurements during the Isotactic Polypropylene Film-Casting Process, J. Appl. Pol. Sci. B 41 (2003) 998-1008.

35. Paul DR: Spin Orientation during Acrylic Fiber Formation by Wet-Spinning, J. Appl. Pol. Sci. 13 (1969) 817-826.

Chapter 4

Pin-Assisted Resin Infiltration of Porous Substrates

Abstract

We analyze computationally the process of pin-assisted resin infiltration of porous substrates. In such a process, a porous substrate is pulled over a staggered array of stationary pins. A wedge-shaped fluid region forms between each pin and the moving substrate and the generated pressure forces the resin to infiltrate into the substrate. The objective is to investigate any relationships between process characteristics (substrate speed, permeability and pin radius) and the extent of resin infiltration. Our results show that the infiltration depth in the limit of a dry substrate scales with $K^{0.403}$ and $R^{0.361}$. The effect of pin radius and of substrate permeability can be expressed by power functions of the dimensionless variables L_o/R and $L_o/\sqrt{K}$. Finally, we suggest a scaling which, for a given pin radius, collapses all ΔL_f data into one master curve described by the equation

$$\Delta L_f = 0.839 K^{0.403} \left[1 + 0.271 \left(L_o / \sqrt{K} \right)^{0.986} \right]^{-1}.$$ The existence of such a relationship allows for the estimation of the sensitivity of the predicted infiltration depth on the relevant parameters, as well as for the design of a multi-pin process.

4.1 Introduction

Polymeric fibrous composites consist of thermoplastic or thermoset polymer matrices reinforced by various types of fibers. Several composites manufacturing technologies have been developed over the past years, such as pultrusion, resin transfer molding and resin infusion with many applications in the aerospace, automotive and construction industries. A key step in the above processes is the resin infiltration of the reinforcement, having a critical and often detrimental effect on the quality and subsequent performance of the final manufactured product. In fact, failure of composite components is most often linked to poor/incomplete resin infiltration of the fibrous substrate. To facilitate this, besides control of the architecture (and thus permeability) of the fibrous preform/substrate, pressure is applied. This can take several forms [1-3]. In the pultrusion process of interest to this study, namely pin-assisted pultrusion, bundles of fibers are

51

pulled through a die and over an array of cylindrical pins located inside a pool of polymeric resin [4-6]. During the pulling of the roving over and around each pin, a small wedge-shaped region is formed between the roving and the pin. The pressure generated in this region forces the fluid to penetrate into the porous substrate while the pulling laterally spreads the fibrous roving making the fluid penetration even easier. Usage of different numbers of pins can accomplish the desired final degree of impregnation.

In previous studies of the process [7-10] the flow of the polymer melt through the porous substrate has been described using Darcy's law [11]:

$$\mathbf{U} = -\frac{\mathbf{K}}{\mu}\nabla p \tag{4.1}$$

where $\mathbf{U}$ the local resin superficial velocity, $\mathbf{K}$ the permeability tensor (which is scalar for isotropic porous media) of the porous medium, a characteristic property of the porous structure which measures the resistance to flow, ∇p the local pressure gradient and μ the viscosity of the fluid. Permeability can be measured experimentally [12,13] or predicted [14,15]. The flow in the region occupied by the polymeric resin is modeled using the-Stokes equation

$$0 = -\nabla p + \mu\nabla^2\mathbf{U} \tag{4.2}$$

combined with the incompressibility condition $\nabla\cdot\mathbf{U}=0$. In the area of composites pultrusion this is justifiable in light of the low elasticity/low processing speed and high viscosity of the resins typically used. Coupling Darcy's flow (Eq.4.1) with Stokes flow (Eq. 4.2) necessitates the use of artificial slip at the porous/fluid interface [16]. Alternatively, Brinkman's equation [17] may be used to model the flow inside the porous medium:

$$\nabla p = -\mu\mathbf{K}^{-1}\mathbf{U} + \mu_e\nabla^2\mathbf{U} \tag{4.3}$$

where μ and μ_e represent respectively the fluid and effective viscosities. Estimation of the effective viscosity remains a lively debate. Neale and Nader [18] proved that if $\alpha=(\mu_e/\mu)^{0.5}$, where α is a slip coefficient introduced by [16], the Brinkman equation with continuity conditions yields the same solution as the Darcy's Law with the slip velocity condition. James and Davis [19] in their numerical study showed that for $\mu_e/\mu=1$, the Brinkman equation over-predicts the velocity at the interface and the infiltration depth, while Tachie et al [20] validated experimentally the results of [19]. An alternative approach has been proposed by Ochoa-Tapia and Whitaker [21], utilizing a sophisticated volume-averaging technique, and assuming a jump in the shear stress condition at the interface. Moreover,

Brinkman's equation has been used extensively to model flows related to composites manufacturing in which a porous zone borders a clear fluid [22-28].

One of the earliest concepts that may be regarded as the forerunner of the pin-assisted infiltration process, derives from the foil lubrication problem [29]. In this, a flexible impermeable tape is in contact with a rotating cylinder and lubricating oil, and the developed oil pressure, in a constant-thickness film forming in the gap between tape and cylinder, is related to the pulling tension of the tape. Extending the idea into a porous substrate, Gaymans and Wevers [30], carried out experiments to examine the infiltration of polypropylene (PP) melt into a glass fiber roving using single- and multiple-pin processes. Their results indicate that the degree of impregnation of the roving may be expressed in terms of the residence time of the melt – a result of a simple integration of Darcy's law. The impregnation is reported to remain relatively unaffected by the radius of the pin and the fiber tension of the roving, while it is strongly affected by the Melt Flow Index (MFI) of the polypropylene melt (high MFI increases impregnation degree) and the presence of more than one pins – with more pins promoting impregnation. Another experimental approach to quantify the impregnation of a glass roving (with polyamide 66) utilizing pins was carried out by Bates and Charrier [31] in which the melt impregnation was determined indirectly, based on measurements of the interlaminar shear strength of the pultruded composite parts. Some of their results indicate that higher number of pins, lower melt viscosity, lower pulling speeds and high tension induced pressure, promotes the impregnation of the roving. On an effort to correlate the experimentally assessed impregnation with process parameters such as pin diameter, pulling tension and melt viscosity, they proposed a global dimensionless group (in light of Darcy's law), called *impregnation number*, which is related to the parameters of the process. This scaling approach produced results of high scatter which however seemed to follow some basic trend and gave a critical impregnation number value for the occurrence of maximum melt impregnation. The same authors (Bates and Charrier [32]) used a simple one dimensional model based on Blok's [29] pulling tension concept, along with experimental measurements, to predict the pulling force of a glass roving dragged over an array of cylindrical pins under assumptions of solid-solid friction. In their study the melt pressure in the gap between the pin and the roving was related via a lumped factor to the pulling tension and additionally consider the additive influence of friction on tension. They report that higher values of the pin radius or arrangements with more pins, increase the pulling force. In terms of pressure, Bates *et al.* [33] employed the essential one dimensional tenets

53

of [29], [31], and [32] to estimate the generated pressure of a glass roving (as well as of an imperbeable tape) dragged over a sequential arrangement of pins, inside a Newtonian fluid pool (silicone oil). The pressure estimation was performed via the measured pulling tension, through a lumped factor (ratio of measured to maximum pressure) the value of which was determined under different experimental conditions - expressed through a lubrication number. Their results for the permeable roving, indicate pressure build up near the zero-tangency point of the pin, while the calculated lumped factor showed constant behavior at the high value region of the lubrication number. Further experimental and modeling investigation of pin-assisted polymer melt impregnation of glass roving, and of particular interest to the present work, was carried out in a subsequent experimental and one-dimensional study by Bates and Zou [34]. Their study regards the roving as a homogeneous porous medium. The flow of the resin in the wedge-shaped region between roving and pin was described by the 1D lubrication theory, while Darcy's law governed resin transport into the roving. It was also assumed that resin flow into the roving occurs in a small region between the roving and the pin, in which the pressure build-up takes place. Their experimental and model results generally indicate that larger numbers of pins or larger pin radii promote resin infiltration, and line speed for a seven-pin arrangement does not seem to influence the impregnation, while in three-pin arrangements it does.

It is clear from the above, that the approaches followed so far have mostly utilized a one-dimensional form of Darcy's law [5,30,31,34] or models which relate the generated pressure with the applied roving's tension [32,33]. It is also obvious that the details of the fluid mechanics of the process in the region near the roving-pin contact are central to any analysis of predictive value. No study has appeared in the technical literature in which the two-dimensional nature of the flow in the entire region where the disturbance introduced by the pin is felt or the details of the intra-roving pressure development (by utilizing Brinkman's equation) have been considered. To fill this gap, we analyze the results of a large number of 2D simulations using the OpenFOAM software to relate the resin infiltration depth to measurable process parameters. We employ Brinkman's equation for the flow in the porous substrate, assuming the latter to be homogeneous and isotropic, and Stokes equation for the flow in the region occupied by the resin.

4.2 Two-Dimensional Model and Boundary Conditions

In an industrial pin-assisted impregnation process, the fibrous roving is pulled over an array of pins located within a resin pool, and over some wrap angle on each pin. This

54

wrapping leads to the formation of three distinct regions between the porous roving and each pin: (a) a converging wedge-shaped region which extends from the maximum distance between the roving and the pin to the zero tangency point (i.e. minimum distance of porous roving from the pin), (b) a region of constant roving/pin separation and (c) a diverging wedge-shaped region in which the roving separates from the pin surface. Our
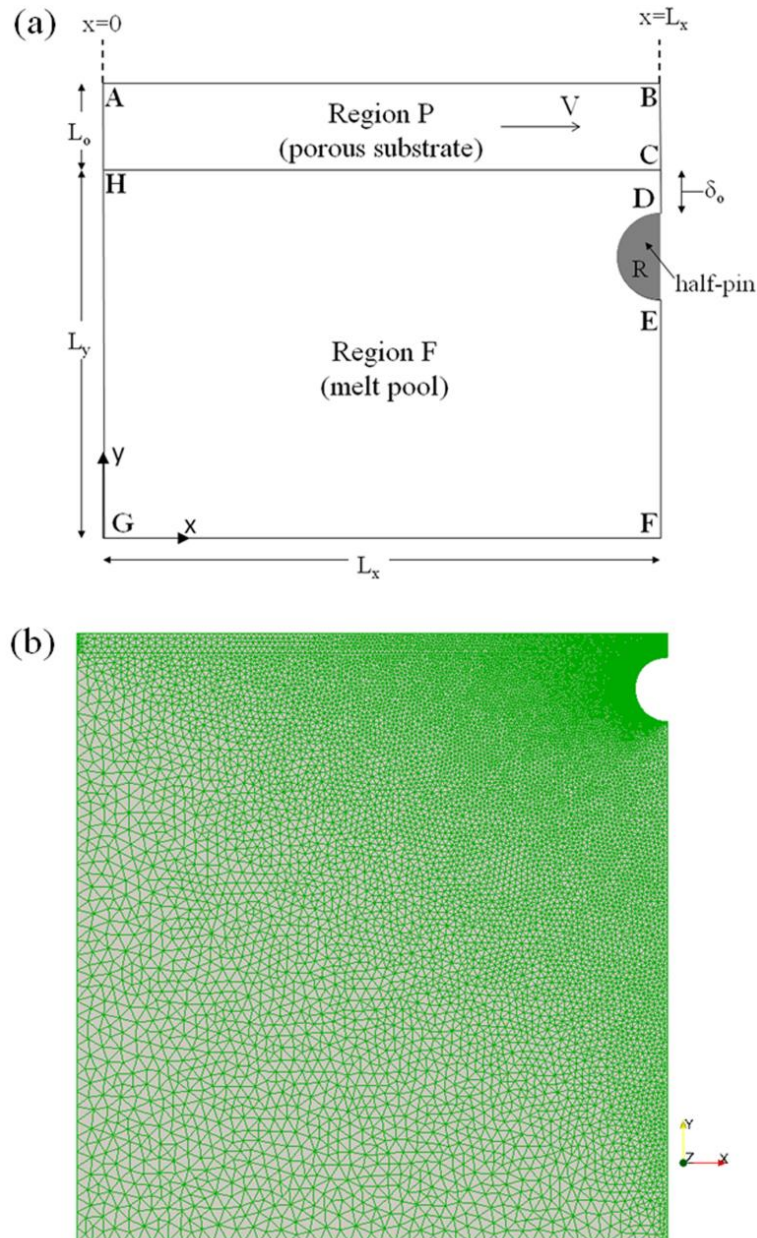
Figure 4-1: Schematic representation of the model geometry (a) and sample computational mesh (b). The pre-impregnated porous zone (thickness L_o) is denoted by the domain ABCH and the melt bath is denoted by the domain CDEFGH. δ_o is the minimum distance between the porous zone and the pin of radius R, L_x and L_y the lengths of the melt pool in the x and y direction respectively and V the pulling speed of the substrate.

analysis considers a single-pin process in which resin infiltration occurs only within the wedge- shaped region forming prior to zero tangency point (zone (a) above). This ignores any additional infiltration that might occur in the small region in which the roving is in near-contact with the pin (zone (b) above). Since the extent of this zone is unknown, this is a reasonable assumption, avoiding the need to introduce arbitrary variables in the analysis. This assumption is also in line with earlier work on the topic (e.g [34]). While any such secondary infiltration is not considered, our analysis takes full account of the presence of a large (compared to the dimensions of the pin) resin pool surrounding it. Bates et al [33] report that as the porous roving is dragged over the pin, contact between the pin surface and individual filaments is possible, with the inter-filament fluid being sheared while frictional forces arise due to contact with the pin surface. Our analysis ignores any such phenomena, chiefly because of the inability to measure the relevant geometrical parameters. Finally, it is known that as it comes in contact with the pin, a fibrous roving will spread laterally (due to leakage flow) over the pin length resulting in a decrease of its thickness as well as in a change in its microstructure. This spreading is also beyond the scope of this study. Summarizing, we focus on the effect the hydrodynamics within the fluid wedge (zone (a) above) have on the extent of resin infiltration, taking full account of the 2D nature of this flow and of the presence of a large resin bath.

The flow in the resin pool is modeled using the Stokes equation (Eq. 4.2) and is regarded as steady-state, isothermal, incompressible and Newtonian, while for the flow inside the porous substrate the Brinkman equation (Eq. 4.3) is utilized. A value of μ=1000 Pa·s is used for the resin viscosity. Following earlier studies of fluid flow in porous media with Brinkman's equation we choose $\mu_e=\mu$ [22-24]. The porous substrate is regarded as isotropic. Brinkman's equation for non-isotropic porous medium and thus use of a second-order permeability tensor can be easily implemented.

The geometrical domain utilized is shown in Fig. 4.1a. A pre-impregrated zone of thickness L_o, the value of which varies, is assumed to exist. This zone moves with speed V (pulling speed) in the x-direction as denoted in Fig. 4.1a. The resin pool (region F) is defined so that L_y>>R and L_x>>R . In this way, the boundary conditions imposed on the corresponding boundaries (that is boundaries FG and GH) will have little, if any, effect to the behavior of the flow in the wedge-shaped region forming between the pin and the porous substrate. A constant value is utilized for the horizontal distance L_x (L_x=90 mm). The vertical distance L_y can vary, since we perform simulations for various values of the pin radius R and the gap δ_o as L_y=84.445+R+δ_o mm. The computational mesh for L_o=3

mm, $L_x=L_y$=90 mm, δ_o=0.544 mm and R=5 mm is shown in Fig. 4.1b. With reference to Fig. 4.1, the following boundary conditions apply:

i. The porous substrate (region P in Fig.4.1a) is assumed to move with speed *V*.

ii. For the boundary DE, which corresponds to the surface of the pin, the usual no-slip condition is applied, along with $\partial p / \partial \mathbf{n} = 0$ for the pressure *p*, where n is the unit normal vector to that boundary.

iii. For boundaries EF, FG and GH we set $\partial \mathbf{U} / \partial \mathbf{n} = 0$, for the velocity and *p*=0 (ambient) for the pressure, reflecting the fact that these boundaries are located far away from the wedge-shaped region where all pressure build-up occurs.

iv. At boundaries BC and CD, we apply $\partial p / \partial \mathbf{n} = 0$ and $\partial \mathbf{U} / \partial \mathbf{n} = 0$ for the velocity. Use of these conditions implies the presence of a constant separation zone past the zero tangency point, as argued above.

v. At boundary AH, we set $\mathbf{U} = V$ for the velocity (i.e. that this boundary moves with the speed of the porous substrate) and $p = 0$ for the pressure.

vi. At the top boundary AB, which represents the resin profile within the porous medium, and whose shape is a-priori unknown, to be determined in the course of the computation, we set $\partial \mathbf{U} / \partial \mathbf{n} = 0$ and *p*=0. This implies that the substrate is sufficiently thick. In other words, we do not consider the case of a thin substrate than can be fully impregnated before a pass around the pin is completed. Following the iterative procedure described in section 4.3 for the determination of the shape of line AB, the velocities on that line, after convergence, will satisfy $\mathbf{U} \cdot \mathbf{n}$=0.

When the Brinkman equation is used to model the porous flow, together with Stokes equation for the clear fluid flow, the most common way of dealing with the boundary conditions at the interface is that both the velocity and stress are assumed to be continuous[19,25]. The same approach is also followed here for the interface CH (see Fig. 4.1a).

The governing equations (continuity equation along with the Stokes (Eq. 4.3) and Brinkman equations (Eq. 4.4), we use the OpenFOAM (Open Source Field Orientation and Manipulation) package utilizing the Finite Volume Method (FVM). In all the simulations performed, the domain was subdivided using an approximate total of 3×10^4 cells. Grading of the mesh density close to the formed wedge-shaped region was also employed.

4.3 Prediction of Fluid Infiltration Profile

In the present section we describe the predictor-corrector method used to predict the shape of the boundary AB (Fig. 4.1) and thus the resin infiltration depth. We start by constructing the computational flow domain assuming a pre-impregnated porous substrate of thickness L_o (0.05mm$<L_o<$4 mm) as shown in Fig. 4.1. The permeability of the porous medium ranges from $K=10^{-6}$ m^2 to $K=10^{-9}$ m^2. The top boundary (boundary AB in Fig. 4.1a) represents the infiltration profile of the fluid. The final shape of AB will be determined by requiring that at steady state the fluid velocity U_n across that boundary $U_n=-U_x\sin\theta+U_y\cos\theta$ is zero. This results in

$$tan\,\theta \equiv \frac{dy}{dx} = \frac{U_y}{U_x} \tag{4.4}$$

where dy/dx is the local slope of line AB, U_y is the velocity in the transverse direction (y-direction) and U_x the velocity in the x-direction. To determine the shape of the infiltration profile, the continuity, Stokes and Brinkman equations are solved for an initial configuration, for example with AB as a straight line. At the end of this step (predictor), the velocity and pressure fields are known everywhere, including on line AB. The corrector step involves the correction of the shape of boundary AB, based on integration of Eq. 4.4, namely

$$y_j^{n+1} = y_o^n + \sum_{j=1}^{N_x} \frac{U_{yj}^n}{U_{xj}^n}\left(x_j^n - x_{j-1}^n\right) \tag{4.5}$$

In Eq. 4.5 y_j corresponds to the updated y-coordinate at the corresponding nodal point at the nth iteration, y_o is the y-coordinate of point A (at $x=0$) in Fig. 4.1a, x_j-x_{j-1} the distance between two successive nodal points of boundary AB in the x-direction and N_x the number of nodes in the x-direction. A similar procedure was used in [35] to predict the lateral spreading of a calendered sheet. Having determined a new shape of boundary AB and thus a new computational domain, a new mesh is constructed and the Stokes, Brinkman and continuity equations are solved again. The new velocity field is used to correct the shape of the boundary AB through Eq. 4.5. The procedure continues until the normal velocity across boundary AB, as determined by the predictor step, is less than a prescribed tolerance ($\varepsilon=10^{-6}$), namely

$$\frac{1}{N_x}\sqrt{\sum_{j=1}^{Nx}\left(U_{nj}\right)^2} \leq \varepsilon \tag{4.6}$$

The normal velocity on line AB is calculated in a straightforward manner using

$$\begin{bmatrix} U_t \\ U_n \end{bmatrix} = \begin{bmatrix} \cos\theta & \sin\theta \\ -\sin\theta & \cos\theta \end{bmatrix} \begin{bmatrix} U_x \\ U_y \end{bmatrix} \tag{4.7}$$

where U_t and U_n are the tangential and normal to the boundary velocities, U_x and U_y the velocities in the x- and y- direction respectively, and θ the local slope of the line AB defined as

$$\theta_j = \tan^{-1}\left(\frac{y_j - y_{j-1}}{x_j - x_{j-1}}\right) \tag{4.8}$$

where y_j and x_j are the coordinates of nodal points on line AB.

Results for the final convergent shape of the boundary AB, assuming μ=1000 Pa·s, L_o=1mm and δ_o=0.544 mm, for different permeability values ($K=10^{-6}$ m^2 to $K=10^{-8}$ m^2) are shown in Fig. 4.2. The final infiltration depth ΔL_f is the vertical distance between point A and point B_i and the maximum distance between the pin and the substrate is located at x=0.085 m (note that R=0.005m). For the cases with highly permeable substrate (e.g. $K=10^{-6}$ m^2) and for low thickness of the pre-impregnated zone (e.g. L_o=1 mm) a maximum of 7 iterations were needed to obtain convergence based on the criterion described by Eq. 4.6. In the cases of low K (e.g. $K=10^{-8}$ m^2) a maximum of 3 iterations were needed, even
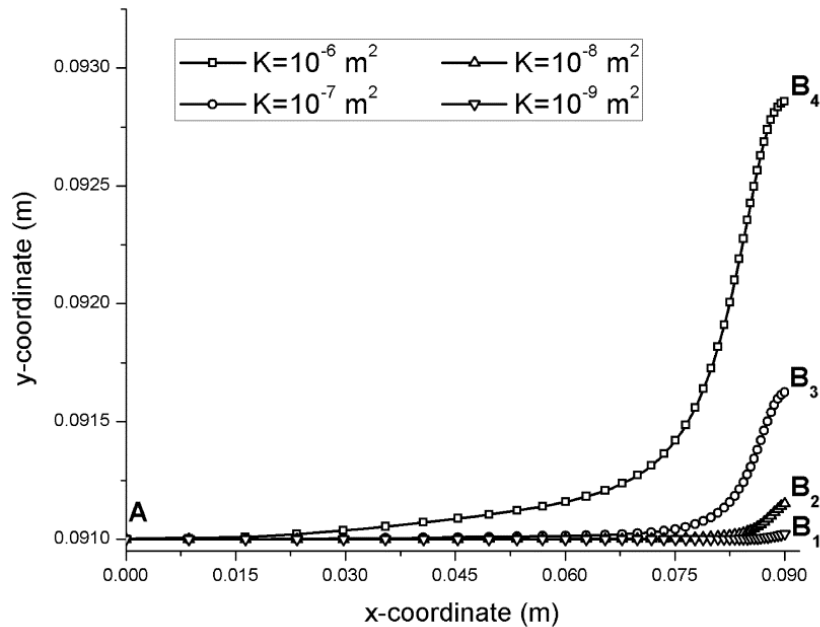
Figure 4-2: Steady state shape of the resin infiltration profile (curves AB$_4$ to AB$_1$) for $K=10^{-6}$, 10^{-7}, 10^{-8} and 10^{-9} m^2 respectively. L_o=1 mm, R=5 mm, δ_o=0.544 mm, V=0.15 m/s, μ=1000 Pa·s.

for the cases of low L_o (e.g. L_o=1 mm). We observe that the maximum infiltration depth ΔL_f is located at the symmetry axis of the pin. It is interesting to also note that, as is evident in the case of K=10^{-6} m^2, a significant amount of fluid infiltrates the substrate well ahead of the pin. We elaborate more on this issue further on in our results.

Consideration of a pre-impregnated zone of thickness L_o is necessary so that a continuum model of the process can be formulated. Neglecting to include such a zone would necessitate consideration of the dry substrate as a two-phase region, in which pockets of air will alternate with solid inclusions (e.g fibers) and which, on one side, will be in contact with the fluid. This physical picture for the process is implicit in earlier works (e.g. Bates and Zou [34]), albeit not utilized. This physical picture has been used with success by Chen and Papathanasiou [36] to model flow through fully-saturated fibrous media; and by Tan *et al* [28] to model flow at the interface between a saturated fiber array and a clear fluid. However, treating the problem at hand as one of un-saturated multiphase flow, would necessitate the use of a free-surface tracking scheme in a geometrically complex, unknown a-priori, multiply-connected domain (the interior free space of the porous substrate). While this is in principle feasible, the complexities involved in free surface tracking, as well as in describing realistically the internal geometry of the porous substrate would divert from present task.

4.4   Results and Discussion

4.4.1   Velocity and Pressure Fields

In this section we give representative results elucidating the structure of the flow and pressure fields, as obtained for the following parameters: K=10^{-8} m^2, R=5 mm, L_o=2 mm, ΔL_f=0.09 mm, V=0.15 m/s and μ=1000 Pa·s. We calculate the velocity profiles along the x- and y- direction in the various locations presented in Fig. 4.3a-4.3c. The velocities in these locations are shown respectively in Fig. 4.3d-4.3f. The fluid inside the melt pool is sheared due to the motion of the substrate - Fig. 4.3d for the location $x=x_A$ far away from the pin. The slightly non-linear shape of the velocity profile at that location (linear would imply simple shear) is indicative of a reverse pressure drop – an extension of the pressure built within the wedge region. This back-flow is manifestly evident from the shape of the U_x velocity profile at the location $x=x_B$ (Fig. 4.3d) as well as at $x=x_C$ and $x=x_D$. Closer to the point of minimum tangency, the flow approaches simple shear, as expected. From the above it is clear that the flow field is the result of the combined action of a pressure-driven back-flow caused by the pressure build-up within the wedge-shaped region and the drag

60

flow caused by the pulling of the porous substrate. It is observed that fluid within a small region adjacent to the porous-open fluid interface is undergoing shear; this shear becomes lower as we move from location x_C to location x_F. The rest of the fluid in the porous region is conveyed with the substrate's pulling speed. The transverse velocity profiles U_y are presented in Fig. 4.3f. The U_y profiles are plotted along lines y_A, y_B, y_C and y_D, the distances of which are equal to the diameter $2R$ of the pin. For $y=y_A=\delta_o/2$ there are negative (that is, downward) U_y values, reflecting the two-dimensional nature of the flow field in
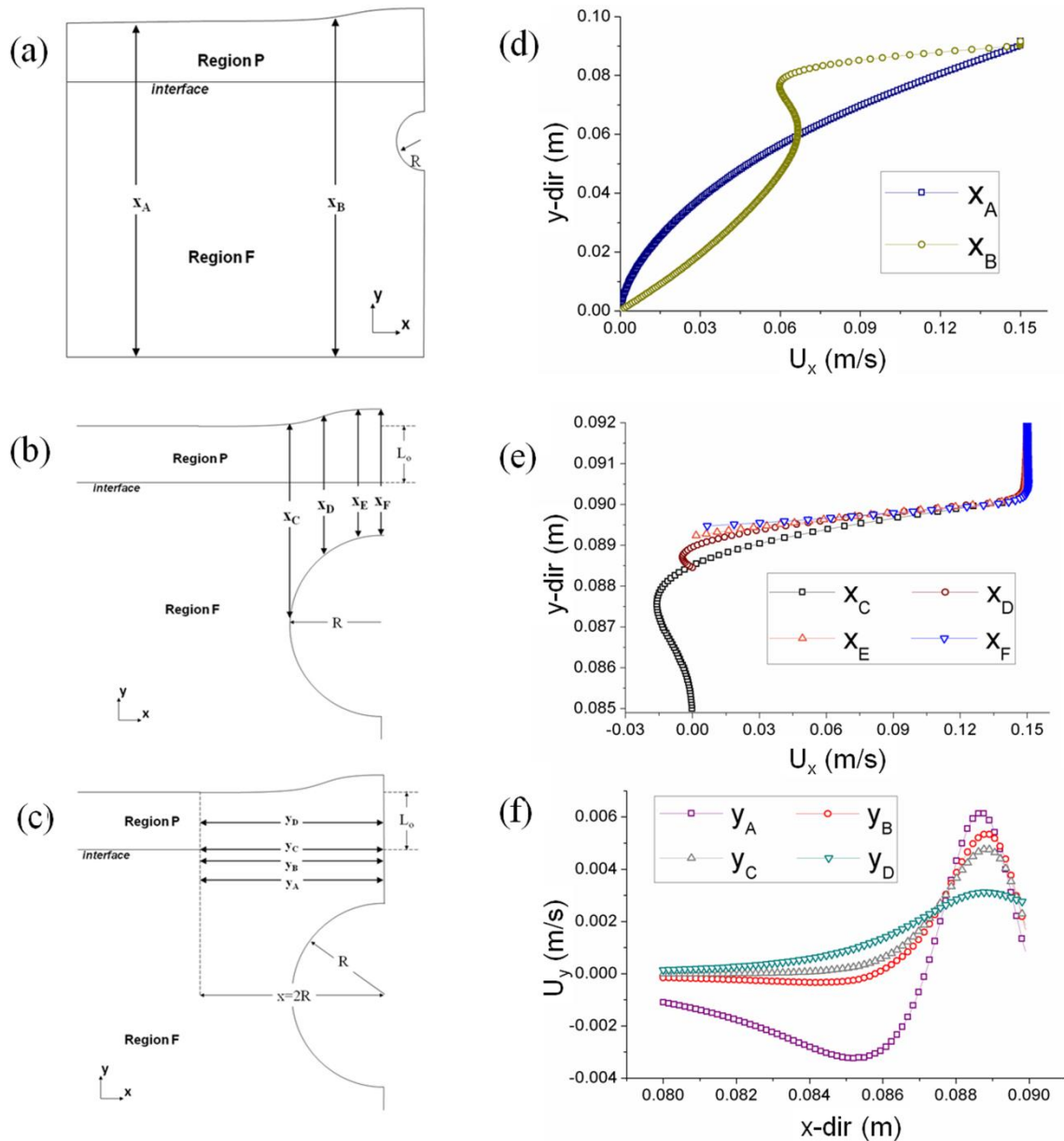
Figure 4-3: Velocity profiles along different directions for $K=10^{-8}$ m^2, $R=5$ mm, $L_o=2$ mm, $\Delta L_f=0.09$ mm, $V=0.15$ m/s and $\mu=1000$ Pa·s. The directions are shown in (a), (b) and (c), and the corresponding velocity profiles are shown in (d), (e) and (f).

61

the resin pool away from the wedge region. Within the substrate, only positive U_y values are found, reflecting the infiltration of the resin. The same results also reveal that there is a significant amount of fluid that moves away from the substrate and the pin as a result of the pressure-driven back-flow as the pin is approached. Therefore, not all fluid dragged by the moving substrate will approach the pin, and even less will enter the porous substrate.
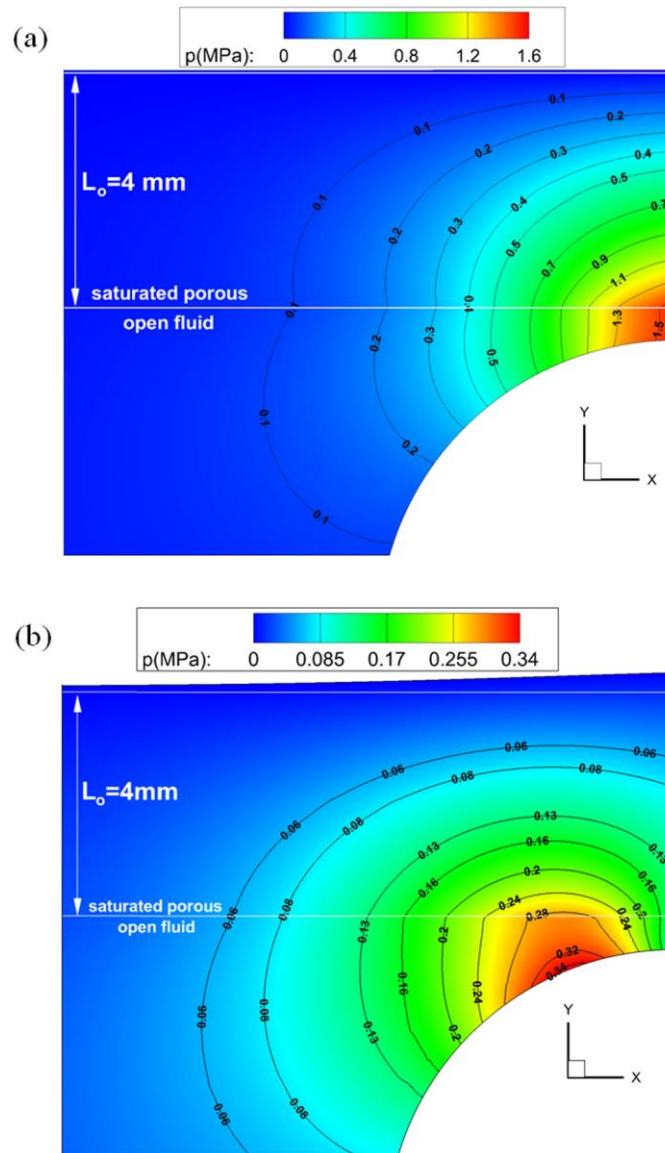
Figure 4-4: Pressure field near the wedge-shaped region formed between the pin and the porous medium for (a) $K=10^{-9}$ m^2, $L_o=4$ mm, $R=5$mm, $V=0.15$ m/s and $\mu=1000$ Pa·s; and (b) $K=10^{-7}$ m^2, $L_o=4$ mm, $R=5$mm, $V=0.15$ m/s and $\mu=1000$ Pa·s. Notice that the small region above L_o corresponds to ΔL_f.

The relevant amounts depend primarily on the permeability of the porous medium. More permeable substrates imply ease of fluid penetration (with subsequent higher value of ΔL_f) and therefore lower tendency for back-flow. For a higher permeability, namely $K=10^{-6}$ m^2,

62

the velocity profiles were also obtained at the same locations (x_A-x_F, y_A-y_D). These simulations revealed that for the same geometric and fluid parameters (R=5 mm, L_o=2 mm, V=0.15 m/s and μ=1000 Pa·s.) the obtained infiltration depth was many times higher (ΔL_f =1.46 mm) than the ΔL_f=0.09 mm obtained for K=10^{-8} m^2. It was also observed that the transverse velocity profiles U_y (at the same locations as in Fig. 4.3f), showed only positive values even within the fluid zone (y=y_A).

The permeability of the porous substrate has a significant effect on the pressure field. This is shown in Fig. 4.4a for K=10^{-9} m^2 and in Fig. 4.4b for K=10^{-7} m^2. Evidently, for K=10^{-9} m^2 the maximum pressure is observed to occur at the zero-tangency point (i.e. minimum distance between the pin and porous substrate). However, when the permeability of the substrate increases, the local pressure maximum shifts away from the zero-tangency point - as shown in Fig. 4.4b. For this reason the resin starts infiltrating even before reaching the wedge-shaped region – observe the infiltration profiles shown in Fig. 4.2. An even larger shift of the pressure maximum to the left is observed for K=10^{-6} m^2, at which value the infiltration of the substrate appears to take place far ahead of the pin (profile AB$_4$ in Fig. 4.2). It should be pointed out that earlier approaches to quantify the infiltration of the porous substrate (e.g. [34]), assume that pressure build-up and resin infiltration take place only in the wedge-shaped region formed between the substrate and the pin. This essentially implies that the pressure at distances beyond one pin radius from the zero tangency point must be zero. The present two-dimensional approach suggests that at high substrate permeabilities significant infiltration may occur well ahead of the pin.

4.4.2 Resin Infiltration Depth

4.4.2.1 Effect of minimum pin-substrate separation

In this section we examine the extent to which changes in the gap δ_o (see Fig. 4.1a) between the porous medium and the pin surface at the zero tangency point affect the achieved infiltration depth ΔL_f. The choice of δ_o is an important one. While its value cannot be measured, it is bound to affect the predicted ΔL_f, since it affects the pressure build-up. A series of simulations were carried out for K=10^{-8} m^2 and R=5 mm with δ_o ranging from 0.17 mm to 0.7 mm. For each value of δ_o, ΔL_f was calculated at different values L_o (from 0.1mm to 4 mm). The obtained results are summarized in Fig. 4.5 in which the ΔL_f has been plotted against $\sqrt{\delta_o L_o}$. It is evident that as the gap at the zero tangency

63
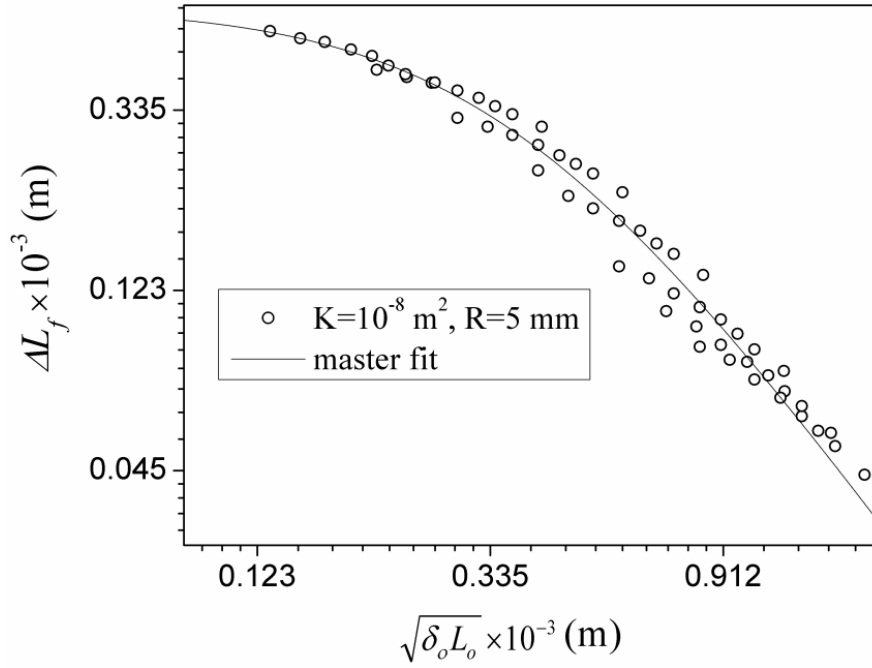
Figure 4-5: Sensitivity of predicted infiltration depth ΔL_f on minimum pin/substrate separation (δ_o). R=5 mm, V=0.15 m/s, K=10^{-8} m^2 and μ=1000 Pa·s.

point decreases, the infiltration depth increases. The data also indicate that the infiltration depth will be finite even for $\delta_o \rightarrow 0$. While this particular issue deserves further study, this is an interesting conclusion. The data in Fig. 4.5 suggest a scaling which may expressed by

$$\Delta L_f = \frac{L_A}{1 + a_A \left(\sqrt{\delta_o L_o}\right)^{b_A}} \qquad (4.9)$$

where α_A=2.405×10^9 and b_A=1.795 are fitted parameters. The parameter L_A (L_A=0.595 mm) represents the value of ΔL_f when the porous medium is in contact with the pin. Equation 4.9 allows for a relative sensitivity analysis on the effect of δ_o on ΔL_f, utilizing

$$\left(\frac{d\Delta L_f}{\Delta L_f}\right)_{RP} = \left(\frac{\partial \Delta L_f}{\partial \delta_o}\right)_{RP} \cdot \frac{\overline{\delta_o}}{\overline{\Delta L_f}} \cdot \frac{d\delta_o}{\delta_o} \qquad (4.10)$$

In Eq. 4.10 $\overline{\delta_o}$ and $\overline{\Delta L_f}$ correspond to a reference point (RP) around which a sensitivity analysis is made. For example, if $\overline{\delta_o}$ is equal to two times the Brinkman screening length ($\overline{\delta_o} = 2\sqrt{K} = 2\times 10^{-4}$ m), at which value the infiltration depth predicted by Eq. 4.9 is $\overline{\Delta L_f}$ =4.481×10^{-4} m, use of Eqs. 4.9 and 4.10 gives that for a 100% variation in the value of δ_o, the expected change in ΔL_f is 22%.

4.4.2.2 Effect of Substrate Permeability

In the following section we examine how the permeability K and the substrate's pre-impregnation thickness L_o affect the infiltration depth ΔL_f. L_o may be expressed in dimensionless form as $L_o/\sqrt{K}$. With the values of pin radius, pulling speed and resin viscosity held constant at R=5mm, V=0.15 m/s and μ=1000 Pa·s respectively, the calculated infiltration depths ΔL_f are plotted as a function of $L_o/\sqrt{K}$ in Fig. 4.6a. It is
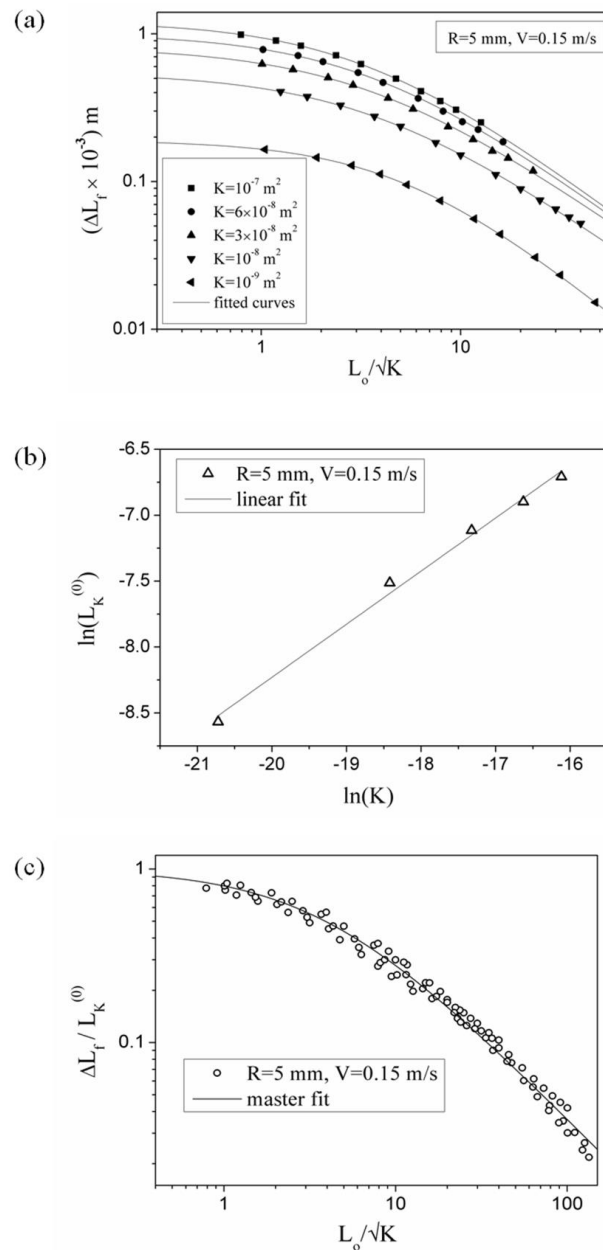
Figure 4-6: (a) Effect of substrate permeability K on infiltration depth ΔL_f for R=5 mm; (b) effect of K on the impregnation depth $L_K^{(0)}$ in the limit of an initially dry substrate ($L_o \to 0$); and (c) master curve showing the effect of $L_o/\sqrt{K}$ on the impregnation depth $\Delta L_f/L_K^{(0)}$.

65

observed that lower K values result in lower infiltration depths ΔL_f, while at each permeability level, the ΔL_f vs $L_o/\sqrt{K}$ data of Fig. 4.6a may be fitted quite well using a non-linear function of the form

$$\frac{\Delta L_f}{L_K^{(0)}} = \frac{1}{1 + a_1\left(\dfrac{L_o}{\sqrt{K}}\right)^{b_1}} \tag{4.11}$$

in which a_1 and b_1 are dimensionless fitting parameters and $L_K^{(0)}$, which represents ΔL_f in the limit of $L_o/\sqrt{K} \to 0$ has units of length. It may be interpreted as the achieved infiltration depth ΔL_f in the limit of a dry porous substrate ($L_o \to 0$). Estimation of the infiltration depth in the limit of a dry porous substrate is of practical significance especially for a multi-pin process. While L_o at the Nth pin is the result of the operation of the N-1 preceding pins and thus possible to determine, the extent of impregnation (if any) of the substrate at the first pin is frequently not known. A reasonable assumption is for that

to be zero, implying an originally dry substrate. The intercepts $L_K^{(0)}$ of each curve in Fig. 4.6a allow us to relate $L_K^{(0)}$ to the permeability K through an expression of the form

$$L_K^{(0)} = A_K K^m \tag{4.12}$$

in which the parameters A_K and m can be obtained by linear fit of $\ln L_K^{(0)}$ vs $\ln K$ as shown in Fig. 4.6b. Our data give A_K=0.839 m^{1-2m} and m=0.403. Therefore the infiltration depth for a dry substrate scales with K as $L_K^{(0)} \sim K^{0.403}$. This may be compared to the scaling $L_K^{(0)} \sim K^{0.5}$ obtained using a simple mass balance approach (see Appendix below section 4.5). Scaling the achieved infiltration depths by $L_K^{(0)}$ and plotting ($\Delta L_f/L_K^{(0)}$) as a function of $L_o/\sqrt{K}$ collapses all data points to a single master curve, as shown in Fig. 4.6c. Each point in Fig. 6c is the result of one simulation corresponding to one set of values for K and L_o. The results can be described by the following equation

$$\Delta L_f = \frac{0.839 \times K^{0.403}}{1 + 0.271\left(\dfrac{L_o}{\sqrt{K}}\right)^{0.986}} \tag{4.13}$$

where $L_K^{(0)}$ is replaced by the expression of Eq. 4.12. The master curve expressed by Eq. 4.13, gives an estimation of the infiltration depth for a given set of R and μ values as a function of L_o and K. A relative sensitivity analysis, utilizing an equation similar to Eq.4.10, around the point ($\overline{K}=10^{-9}$ m^2 and $\overline{\Delta L_f}$=7.4166×10^{-5} m) indicates that a 90%

66

relative change in K (from 10^{-9} m^2 to 10^{-10} m^2) gives a 71% relative change in the infiltration depth. A one order of magnitude change in K is a reasonable choice. Bates and Zou [34] report that the void fraction in the porous roving and for a single-pin process, changes from 0.5 to 0.3. For hexagonal packing of fibers this corresponds to a permeability range of approximately two orders of magnitude [14].

It should be also noted that in the master curve presented in Fig. 4.6c, the minimum value of L_o was taken to be of the order of Brinkman's screening length $\left(L_o/\sqrt{K}\right)_{min} \sim 1$. In geometric terms (i.e. monofilament diameter D_f), L_o may be used to deduce to the required number of monofilament layers. For example, for E-glass fibers with D_f=17 μm [37], $\left(L_o/\sqrt{K}\right)$=100 μm (for K=10^{-8} m^2), L_o would be of the order of six glass monofilament diameters (hexagonally packed fibers at volume fraction 80%) while for high strength carbon fibers with D_f=7 μm [37] L_o would be of the order of fifteen carbon fiber diameters.

4.4.2.3 Effect of Pin Radius

A similar procedure is followed in the analysis of results for varying pin radius R and fixed K, V and μ (K=10^{-8} m^2, V=0.15 m/s and μ=1000 Pa·s). The pin radius R may be scaled with the pre-impregnation depth L_o as L_o/R, giving a dimensionless pre-impregnation thickness. The impregnation depth ΔL_f versus L_o/R results are shown in Fig. 4.7a. The range of the pin radii investigated in the present study are within typical limits similar to earlier experimental studies of the process (e.g. [30]). Evidently, employing pins with higher R promotes resin infiltration. For a specific R the infiltration depth decreases as the dimensionless quantity L_o/R increases (or as L_o increases). This feature is observed for all the pin radii examined which range from R=3 mm to R=20 mm. The numerical data can be described by a function of the form

$$\frac{\Delta L_f}{L_R^{(0)}} = \frac{1}{1+a_2\left(\dfrac{L_o}{R}\right)^{b_2}} \tag{4.14}$$

As shown in Fig. 4.7a, in Eq. 4.14, a_2 and b_2 are fitting parameters. The fitting parameter $L_R^{(0)}$ corresponds to the value where the fitted curves intercept with the ΔL_f axis, the physical meaning of the which may be regarded as the infiltration depth achieved in the limit of a dry substrate ($L_o \rightarrow 0$). It is clear from Fig. 4.7a that $L_R^{(0)}$ is affected by the pin radius R. It is also clear that at larger values of L_o/R, pins of differing radii yield curves
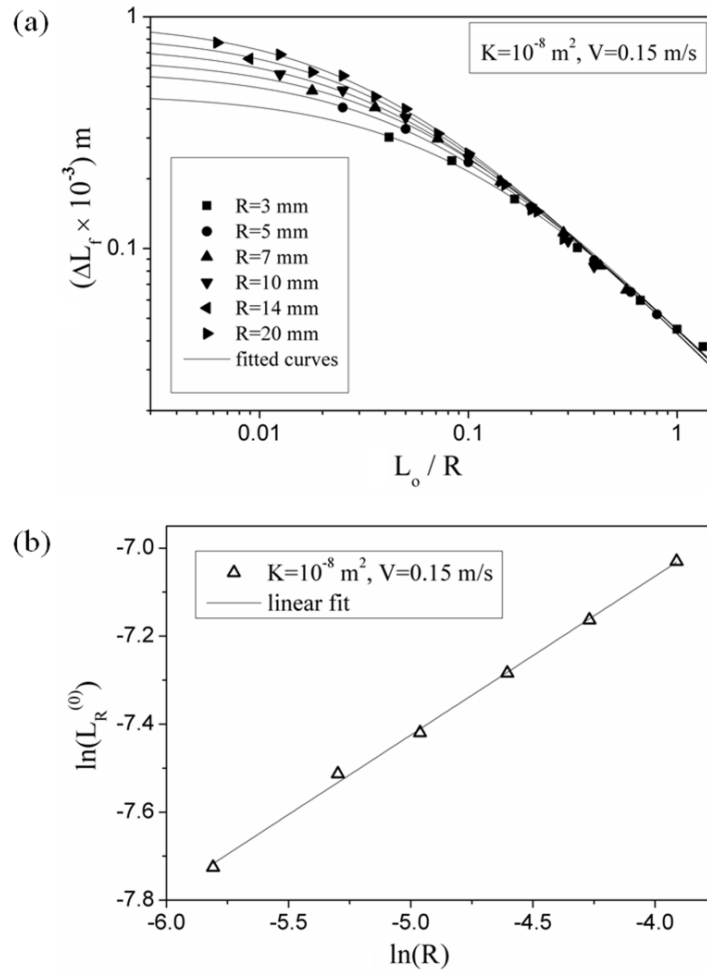
Figure 4-7: (a) Effect of the pin radius R on the impregnation depth ΔL_f for different values of the dimensionless depth L_o/R ($K=10^{-8}$ m^2); and (b) effect of the pin radius R on the impregnation depth $L_R^{(0)}$ in the limit of an initially dry substrate ($L_o \to 0$) for $K=10^{-8}$ m^2 and $\mu=1000$ Pa·s.

that are asymptotically identical. To quantify this correlation we plot $\ln(L_R^{(0)})$ against $\ln(R)$. The results are shown in Fig. 4.7b. Fitting of the results by a function of the form

$$L_R^{(0)} = A_R \cdot R^n \tag{4.15}$$

gives an estimate of the effect of R on $L_R^{(0)}$. The linear fit parameters obtained are $A_R=3.626\times10^{-3}$ m^{1-2n} and $n=0.361$. Eq. 4.15 implies a correlation of the form $\Delta L_f \sim K^{0.361}$. This is in reasonable agreement with the result shown in Appendix (after section 4.5) for a dry porous substrate, namely $\Delta L_f \sim R^{0.5}$.

As shown in Fig. 4.7a, and for approximately $L_o/R>0.2$, the obtained infiltration depths ΔL_f remain unaffected by the different pin radii (same slope region). At this region the corresponding values of the pre-impregnation thickness L_o are generally high. This implies that any variation in the radius of the pin, for a specific L_o, would simply cause the

68

same level of infiltration in the porous medium. That is not the case when the pre-impregnated thickness holds lower values (i.e. lower values of L_o/R). Such a behavior might help explain the results by Bates and Zou [34] in which they report that essentially for a seven-pin arrangement the pin diameter affects to a small extend, if any, the infiltration in contrast to the three-pin arrangement where the effect is very high.

4.4.2.4 Effect of Pulling Speed

Figure 4.8 shows the effect of the pulling speed V on the infiltration depth ΔL_f for different values of L_o (R=5 mm, K=10^{-8} m^2 and μ=1000 Pa·s) for a single-pin process. It is evident that the infiltration depth ΔL_f remains unaffected by the pulling speed. In the practice of pultrusion, pulling speed relates to the residence time of the roving into the resin bath and is a parameter of significance. A simple relationship between the infiltration
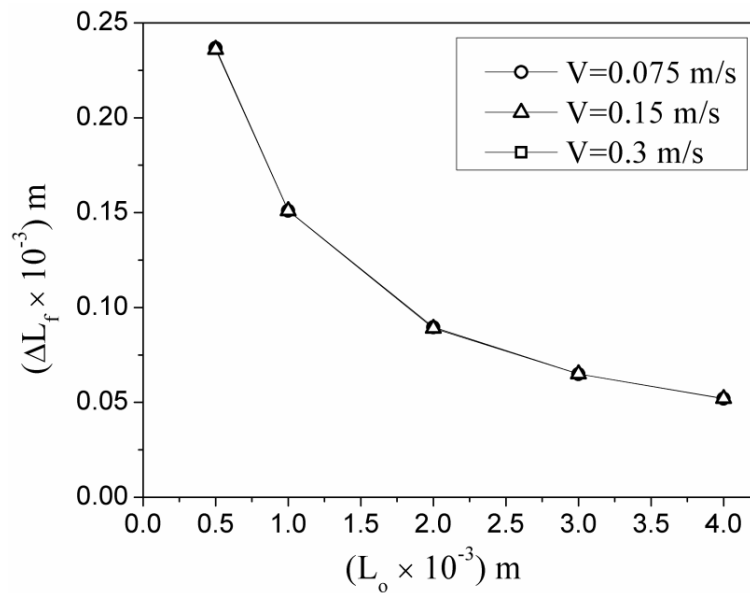
Figure 4-8: Effect of L_o on the impregnation depth ΔL_f for three different pulling speeds, for R=5mm, K=10^{-8} m^2 and μ=1000 Pa·s.

depth ΔL_f and process parameters (V, K, R and μ) is derived in Appendix (below section 4.5), based on a mass conservation argument. Since our results show no effect of V on resin infiltration, and in light of Eq. A–4, the implication is that the ratio P_{av}/V must remain constant when V changes - where P_{av} is the average pressure developing between the pin and the substrate $P_{av} = \dfrac{1}{L_x} \int\limits_{Lx} P(x)dx$, where L_x is the length at the porous medium / fluid interface where this pressure is applied. Thus, even though increasing pulling speed

does increase the developed pressure, as shown in terms of pulling force by Bates et al. [32] and corroborated by our simulations, the ratio P_{av}/V remains constant with respect to V. Consequently, for constant viscosity of the fluid and permeability of the porous substrate, changes in the pulling speed will not affect the achieved infiltration depth. This result is also verified experimentally in the work by Bates and Zou [34] for a three pin system – however their results for a 7-pin system did not show this trend.

4.5 Conclusions

We have studied the pin-assisted infiltration process of a Newtonian resin into a porous substrate via a 2D computational approach utilizing the Stokes equation, for the clear-fluid flow, and Brinkman's equation for the flow in the porous region. A key feature of the model is the existence of a pre-impregnated zone within the porous substrate as it approaches the pin – the depth of this zone is a variable in the analysis. Our results indicate that the infiltration profile is of sigmoidal shape with maximum infiltration at the zero tangency point of the pin. Interestingly enough, for higher values of permeability (e.g. $K=10^{-6}$ m^2) the fluid starts infiltrating far ahead of the wedge-shaped region forming between the pin and the porous substrate. This may be explained in terms of the maximum generated pressure, the location of which, for higher K values, shifts away from the zero-tangency point of the pin. This shift necessitates the use of a larger-area model that extends beyond the neighborhood of the pin. The structure of the flow-field reveals the presence of back-flow caused by the build-up of pressure near the pin surface. Following a large number of simulations, we analyze the results in terms of the achieved resin infiltration depth ΔL_f as function of substrate permeability K and pin radius R. For the limit of a dry substrate ($L_o \to 0$) we find $\Delta L_f \approx K^{0.403}$ and $\Delta L_f \approx R^{0.361}$. Finally, we suggest a scaling which, for a given pin radius, collapses all ΔL_f data into one master curve described by the equation $\Delta L_f = 0.839 K^{0.403} \left[1 + 0.271 \left(L_o / \sqrt{K} \right)^{0.986} \right]^{-1}$. The existence of such a relationship allows for the estimation of the sensitivity of the predicted infiltration depth on the relevant parameters, as well as for the design of a multi-pin process. Our results finally, indicate that changes in the pulling speed of the porous substrate does not affect the infiltration depth; this is probably because as V increases, the pressure within the fluid wedge also increases so that the ratio P_{av}/V remains constant.

APPENDIX

Consider the geometry of the wedge-shaped region between the pin and the moving porous substrate. Fluid leaves this region - and enters the porous substrate - by virtue of the pressure differential between the fluid zone, where a pressure profile $P(x)$ exists and the ambient pressure ($P=0$) existing within the dry substrate. Conservation of mass in a differential control volume $dV=WL(x)\,dx$, dictates that the amount of fluid dQ leaving a section of the wedge-shaped fluid region enters the porous substrate where its flow is governed by Darcy's law. As a result

$$dQ = WU_y dx = W \cdot \frac{K}{\mu} \frac{P(x)}{L(x)} dx \qquad \text{(A-1)}$$

were W is the width of the system and $L(x)$ the infiltration depth at the location x. Integration gives

$$Q_1 = \frac{KW}{\mu} \int_{-x0}^{0} \frac{P(x)}{L(x)} dx \qquad \text{(A-2)}$$

If the pressure $P(x)$ and infiltration $L(x)$ profiles are known, the integral in the above equation can be evaluated exactly. At the same time, an overall mass balance states that the total amount of fluid Q_1 leaving the wedge region will exit with the moving substrate. If L_f is the final achieved infiltration depth, V the velocity of the substrate and W its width, this flux is $Q_2 = VWL_f$. Therefore, the mass balance will give

$$L_f = \frac{K}{\mu V} \int_{-x0}^{0} \frac{P(x)}{L(x)} dx \qquad \text{(A-3)}$$

This however is of no practical use, since knowing $L(x)$ implies knowledge of the final infiltration depth L_f. However, an interesting result can be derived if the integral in Eq. (A-3) is simplified by assuming that (*i*) an average pressure $P_{av.}$ exists in the wedge-shaped region, (*ii*) the infiltration profile can be approximated by an average infiltration thickness L_{av} which is expressed as a fraction of L_f ($L_{av}=f_1 \cdot L_f$, where $f_1<1$, and (*iii*) this average pressure $P_{av.}$ is applied over a distance x_o that is some fraction of the pin radius $x_o=f_2 \cdot R$. Evaluating the integral based on assumptions (i)-(iii) above gives

$$L_f = \sqrt{\frac{KP_{av.}fR}{\mu V}} \qquad \text{(A-4)}$$

in which the factor f is meant to include all assumptions associated with the simplifications (i)-(iii). Eq. (A-4) indicates that the infiltration depth achieved at the first pin will scale with $\sqrt{K}$ and $\sqrt{R}$.

71

4.6 References

1. Hilakos W. Resin impregnation of fiber structures. US4728387 A, 1988.

2. Gibson AG, Månson J-A. Impregnation technology for thermoplastic matrix composites. Compos Manuf. 1992;3(4):223–33.

3. Carlsson A, Tomas Åström B. Experimental investigation of pultrusion of glass fibre reinforced polypropylene composites. Compos Part Appl Sci Manuf. 1998;29(5–6):585–93.

4. Peltonen P, Lahteenkorva K, Paakkonen EJ, Jarvela PK, Tormala P. The Influence of Melt Impregnation Parameters on the Degree of Impregnation of a Polypropylene/Glass Fibre Prepreg. J Thermoplast Compos Mater. 1992;5(4):318–43.

5. Bijsterbosch H, Gaymans RJ. Impregnation of glass rovings with a polyamide melt. Part 1: Impregnation bath. Compos Manuf. 1993;4(2):85–92.

6. Peltonen P, Törmälä P. Melt impregnation parameters. Compos Struct. 1994;27(1–2):149–55.

7. Lee WI, Springer GS. A Model of the Manufacturing Process of Thermoplastic Matrix Composites. J Compos Mater. 1987;21(11):1017–55.

8. Bafna SS, Baird DG. An Impregnation Model for the Preparation of Thermoplastic Prepregs. J Compos Mater. 1992;26(5):683–707.

9. Kim TW, Jun EJ, Um MK, Lee WI. Effect of pressure on the impregnation of thermoplastic resin into a unidirectional fiber bundle. Adv Polym Technol. 1989;9(4):275–9.

10. Kim D-H, Lee WI, Friedrich K. A model for a thermoplastic pultrusion process using commingled yarns. Compos Sci Technol. 2001;61(8):1065–77.

11. Dullien FAL. Porous Media: Fluid Transport and Pore Structure. Academic Press; 1991.

12. Parnas RS, Howard JG, Luce TL, Advani SG. Permeability characterization. Part 1: A proposed standard reference fabric for permeability. Polym Compos. 1995;16(6):429–45.

13. Gebart BR, Lidström P. Measurement of in-plane permeability of anisotropic fiber reinforcements. Polym Compos. 1996;17(1):43–51.

14. Gebart BR. Permeability of Unidirectional Reinforcements for RTM. J Compos Mater. 1992;26(8):1100–33.

15. Bruschke MV, Advani SG. Flow of generalized Newtonian fluids across a periodic array of cylinders. J Rheol 1978-Present. 1993;37(3):479–98.

16. Beavers GS, Joseph DD. Boundary conditions at a naturally permeable wall. J Fluid Mech. 1967;30(1): 197-207.

17. Brinkman HC. A calculation of the viscous force exerted by a flowing fluid on a dense swarm of particles. Appl Sci Res. 1949;1(1):27–34.

18. Neale GH, Nader WK. Prediction of transport processes within porous media: Creeping flow relative to a fixed swarm of spherical particles. AIChE J. 1974;20(3):530–8.

19. James DF, Davis AMJ. Flow at the interface of a model fibrous porous medium. J Fluid Mech. 2001;426:47–72.

20. Tachie MF, James DF, Currie IG. Velocity measurements of a shear flow penetrating a porous medium. J Fluid Mech. 2003;493:319–43.

21. Ochoa-Tapia JA, Whitaker S. Momentum transfer at the boundary between a porous medium and a homogeneous fluid—I. Theoretical development. Int J Heat Mass Transf. 1995;38(14):2635–46.

22. Ranganathan S, Phelan FR, Advani SG. A generalized model for the transverse fluid permeability in unidirectional fibrous media. Polym Compos. 1996;17(2):222–30.

23. Yu B, James Lee L. A simplified in-plane permeability model for textile fabrics. Polym Compos. 2000;21(5):660–85.

24. Ngo ND, Tamma KK. Microscale permeability predictions of porous fibrous media. Int J Heat Mass Transf. 2001;44(16):3135–45.

25. Costa VAF, Oliveira LA, Baliga BR, Sousa ACM. Simulation of coupled flows in adjacent porous and open domains using a control-volume finite-element Method. Numer Heat Transf Part Appl. 2004;45(7):675–97.

26. Tan H, Pillai KM. Finite element implementation of stress-jump and stress-continuity conditions at porous-medium, clear-fluid interface. Comput Fluids. 2009;38(6):1118–31.

27. Salinger AG, Aris R, Derby JJ. Finite element formulations for large-scale, coupled flows in adjacent porous and open fluid domains. Int J Numer Methods Fluids. 1994;18(12):1185–209.

28. Tan H, Chen X-M, Pillai MK, Papathanasiou TD, Evaluation of boundary conditions at the clear-fluid and porous-medium interface using BEM, 2008, FPCM-9, Montreal, Quebec, Canada

29. Blok H, van Rossum JJ. The foil bearing-A new departure in hydrodynamic lubrication, Lubrication Engineering, 1953;20:316.

30. Gaymans RJ, Wevers E. Impregnation of a glass fibre roving with a polypropylene melt in a pin assisted process. Compos Part Appl Sci Manuf. 1998;29(5–6):663–70.

31. Bates PJ, Charrier JM. Effect of Process Parameters on Melt Impregnation of Glass Roving. J Thermoplast Compos Mater. 1999;12(4):276–96.

32. Bates PJ, Charrier JM. Pulling tension monitoring during the melt impregnation of glass roving. Polym Compos. 2000;21(1):104–13.

33. Bates PJ, Kendall J, Taylor D, Cunningham M. Pressure build-up during melt impregnation. Compos Sci Technol. 2002;62(3):379–84.

34. Bates PJ, Zou XP. Polymer Melt Impregnation of Glass Roving. Int Polym Process. 2002;17(4):376–86.

35. Polychronopoulos ND, Sarris IE, Papathanasiou TD. 3D features in the calendering of thermoplastics: A computational investigation. Polym Eng Sci. 2014;54(7):1712–22.

36. Chen X, Papathanasiou TD. The transverse permeability of disordered fiber arrays: a statistical correlation in terms of the mean nearest interfiber spacing. Transp Porous Media. 2008;71(2):233–51.

37. Cogswell FN, Thermoplastic aromatic polymer composites, Butterworth-Heinmann Ltd, 1992.

Chapter 5

A novel model for resin infiltration in pin-assisted pultrusion

Abstract

Based on the results of a comprehensive numerical study of pin-assisted pultrusion, we present a simple explicit model which allows for the estimation of the infiltration depth as a function of measurable parameters. The numerical approach on which the infiltration model is based combines use of Stokes equation within the resin pool, Brinkman equation for flow inside the porous roving and a predictor-corrector iterative scheme to determine the location of the advancing resin front inside the roving. As a result of each computation we obtain a value for the infiltration depth h_f, which depends on process and material parameters, such as roving speed V, pin radius R, resin viscosity μ and substrate permeability K. The results of hundreds of such calculations are analyzed in terms of a dimensionless number $\Lambda = \mu V L_o \delta / \overline{P} K R$ and a master curve is obtained, according to which h_f is a power function of Λ, namely $h_f = C/\left(1 + A\Lambda^B\right)$, where A, B and C are known parameters, obtained from non-linear data fitting. Following this, we extend the model to incorporate the tensioning force as well as present a procedure for its use in multiple-pin arrangements. Finally, we present result of an extensive parametric analysis as well as comparisons with published experimental data; the agreement with the latter is very encouraging, the model being in all cases in semi-quantitative agreement with experiment.

5.1 Introduction

The infiltration of a polymeric resin into a fibrous network is the determining step in several composites manufacturing technologies, such as pultrusion [1], resin transfer molding [2] or resin infusion [3]. Poor or incomplete impregnation of a fibrous preform is the source of defects in composite components. In the pin-assisted pultrusion process of interest to this study, bundles of fibers (usually in the form of a flexible roving) are pulled through a die and over an array of solid pins located inside a resin pool [4,5] as shown schematically in Fig. 5.1. As the fibrous roving moves around each pin, a small wedge-shaped converging region of polymeric resin forms between the pin surface and the roving.
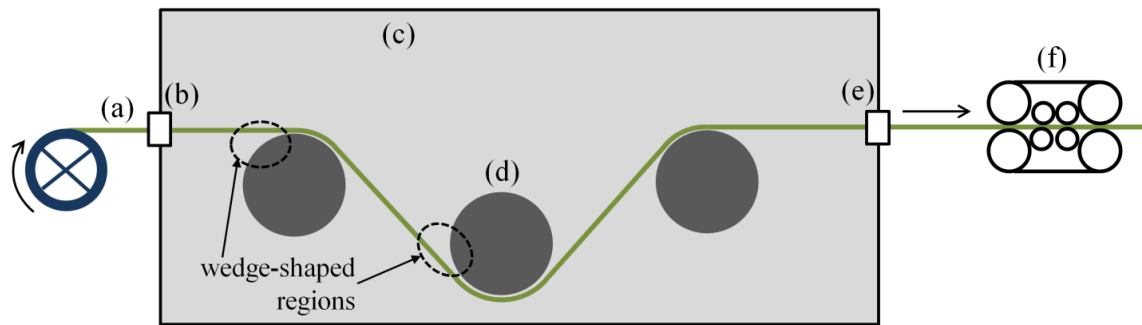
Figure 5-1: Schematic representation of the pin-assisted pultrusion process studied. The fibrous preform (a) enters from an entry die (b) into a melt bath (c) in which it moves over an array of cylindrical pins (d). The preform exits the bath through an exit die (e) as it is pulled from a double belt puller (f). For illustrative purposes a three-cylinder system is shown here but more cylinders can be utilized. Figure not to scale.

Lubrication theory mandates that a pressure rise occurs within this region; this pressure forces the resin to infiltrate into the fibrous roving. The total infiltration depth achieved in the process is the result of the sequential passage of the roving over several pins in the resin bath. The fibrous preform being essentially a porous medium, Darcy's law has been used to assess the extent of resin infiltration for any given pressure build-up near the pin surface [6,7]. Bates and Charrier [8] followed an experimental approach to determine the effect of a dimensionless number (impregnation number Ψ) on impregnation. This number was an empirical dimensionless number which combined equipment (e.g. pin radius) and process parameters (e.g. melt viscosity) as well as the roving characteristics (e.g. roving void fraction). In the study of Bates and Zou [9] the impregnation process was studied numerically, based on one-dimensional lubrication flow in the wedge region and Darcy's flow inside the fibrous roving. The results in terms of the extent of resin infiltration compared well with experimental observations. Factors such as the pulling speed of the roving, the pin radius, the contact time between the pin and the roving, the viscosity of the polymeric resin, and the void fraction of the roving were reported to affect impregnation. Another measurable process parameter correlating directly with the extent of impregnation is the tension T required to move the roving over an array of pins. It has been also shown by Bates and co-workers [10,11] that T is a linear function of the pressure generated at the pin surface, the slope depending on variations in the pin radius and the number of pins utilized.

In a previous study [12] we have shown that the effect of pin radius R and substrate permeability K on the extent of infiltration (as obtained computationally) can be expressed as power functions of the dimensionless quantities (L_o/R) and $(L_o/\sqrt{K})$, L_o being the depth of the substrate saturated with resin prior to coming in contact with the pin. Limiting forms corresponding to dry substrates were also derived. This has allowed the generation of master curves expressing the above influences. The scope of the present study is to investigate the existence of a general relationship (master curve) between process parameters and the obtained extent of resin infiltration in a multi-pin pultrusion process, as well as investigate whether the predictions of such a model are in agreement with the (unfortunately limited) experimental data available in the technical literature.

5.2 Two Dimensional Model and Boundary Conditions

The flow is modeled as two-dimensional and Brinkman equation is used to model the flow within the fibrous roving. A schematic of the region of interest is shown in Fig. 5.2. The resin located in the pool is assumed to be incompressible, isothermal, Newtonian and the flow is modeled by the Stokes equation

$$0 = -\nabla p + \mu \nabla^2 \mathbf{U} \qquad (5.1)$$

where p the pressure, $\mathbf{U}$ the velocity vector and μ the viscosity of the fluid, combined with the incompressibility condition $\nabla \cdot \mathbf{U} = 0$. This is justifiable in light of the low elasticity/low processing speed and high viscosity of the resins typically used in pin-assisted pultrusion. The fibrous preform is assumed to be an isotropic homogeneous porous medium the flow in which is described by the Brinkman equation

$$\nabla p = -\mu \mathbf{K}^{-1} \mathbf{U} + \mu \nabla^2 \mathbf{U} \qquad (5.2)$$

where μ the resin viscosity (in which we have assumed $\mu_e = \mu$ [13-16]) and $\mathbf{K}$ the permeability tensor ($\mathbf{K} = K_{ij}$ for $i,j = x,y$) for which we assume that the diagonal tensor components are zero ($K_{xy} = K_{yx} = 0$) and the longitudinal permeability K_{xx} is equal to the transverse permeability K_{yy} ($K_{xx} = K_{yy} = K$); it is the value of K that varies in our analysis.

A pre-impregnated zone of thickness (L_o) is assumed to exist within the substrate, the value of which may vary. Since the size of the melt pool is much larger than that of the wedge-shaped region, the influence of boundary conditions on pressure build-up in the wedge will be minimal. The extent of resin infiltration (determined in the course of the computation) is denoted as h_f and δ is the separation between the pin surface and the

77

porous substrate. A computational domain (before the computation of h_f) along with the finite volume unstructured mesh (L_o=4 mm, δ=0.5 mm and R=5 mm) is shown in Fig. 5.3.
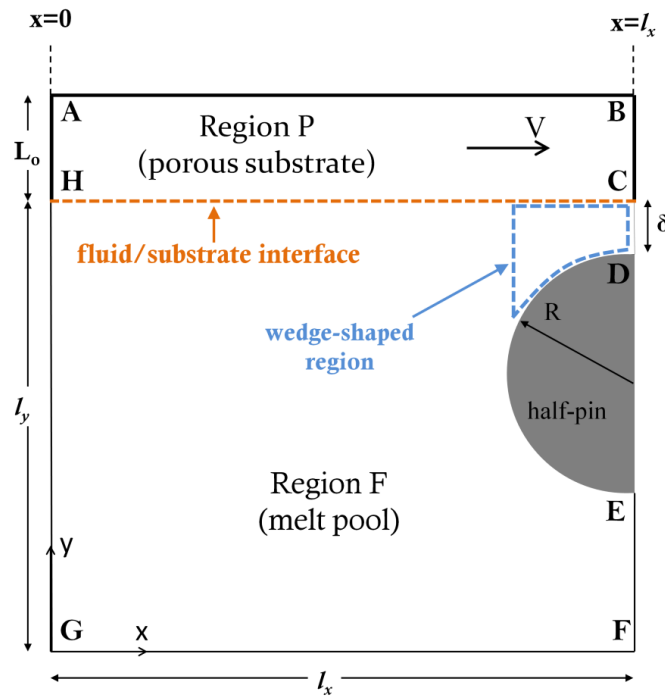
Figure 5-2: Schematic representation of the formulated model geometry. The pre-impregnated porous zone (thickness L_o) that moves with speed V is denoted by the domain ABCH and the clear fluid region (melt pool) by the domain CDEFGH. δ is the minimum distance between pre-impregnated zone and the pin of radius R. Also shown the formed wedge-shaped region. The distances l_x and l_y correspond to the size of the fluid pool for which we assume l_x=l_y>>R. Figure not to scale.
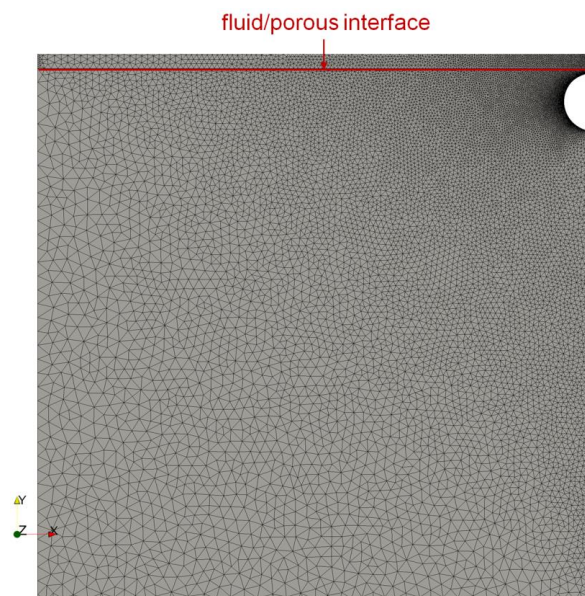
Figure 5-3: Typical computational mesh (34000 cells with edge grading near the half-pin region) for R=5 mm, L_o=4 mm and δ=0.5 mm. The horizontal red line corresponds to the interface between the clear fluid (located below the line) and the pre-impregnated zone of L_o thickness.

With reference to Fig. 5.2, the following boundary conditions apply:

i.   Boundaries EF, FG and GH: we set $\partial \mathbf{U} / \partial \mathbf{n}$, for the velocity and p=0 (ambient) for the pressure, reflecting the fact that these boundaries are located far away from the wedge-shaped region. $\mathbf{n}$ is the unit normal vector of each boundary.

ii.   Boundary DE (pin surface): no-slip condition for velocity and $\partial p / \partial \mathbf{n} = 0$ for the pressure.

iii. Boundary CD: we set $\partial p / \partial \mathbf{n} = 0$ and $\partial \mathbf{U} / \partial \mathbf{n} = 0$. These conditions imply the presence of a constant separation zone past the zero tangency point, of uniform thickness, as argued above.

For the homogeneous porous substrate we set the following boundary conditions:

i.   Pre-impregnation zone (Fig. 5.2) is assumed to move with speed V.

ii.   Boundary BC: similar to the boundary CD (see above).

iii. Boundary AH: moves with speed V ($\mathbf{U}$=V).

iv.   Boundary AB: This boundary represents the resin profile within the porous medium (see Fig. 5.2) whose shape is a priori unknown and is determined in the course of the computation. By applying $\partial \mathbf{U} / \partial \mathbf{n} = 0$ and p=0 we assume that the substrate is sufficiently thick. In other words, we do not consider the case of a thin substrate that can be fully impregnated before a pass around the pin is completed. Following the iterative procedure described in the next section for the determination of line AB shape, the velocities on that line, after convergence will satisfy $\mathbf{U} \cdot \mathbf{n} = 0$.

The governing equations (continuity equation along with the Stokes and Brinkman equations) are solved using the OpenFOAM (Open Source Field Orientation and Manipulation) software package utilizing the Finite Volume Method (FVM). In all the simulations performed, the domain was subdivided using an approximate total of 3.4×10^4 cells. Grading of the mesh density close to the wedge-shaped region was also employed.

5.3   Prediction of Resin Infiltration Profile

In the present section we describe the predictor-corrector method used to predict the shape of the boundary AB in Fig. 5.2 and thus the fluid infiltration depth h_f. The shape of

the infiltration profile AB is determined by requiring that at steady state the fluid velocity $u_n = u_y \, cos \, \theta - u_x \, sin \, \theta$ across that boundary is zero. This results in

$$tan \, \theta \cong \frac{dy}{dx} = \frac{u_y}{u_x} \qquad (5.3)$$

where dy/dx is the local slope of line AB, u_y is the velocity in the y-direction and u_x the velocity in the x-direction. To determine the shape of the infiltration profile, the continuity, Stokes (Eq. 5.1) and Brinkman (Eq. 5.2) equations are solved for an initial configuration, for example with AB as a straight line. At the end of this step (predictor), the velocity and pressure fields are known everywhere, including on line AB. The corrector step involves the correction of the shape of boundary AB, based on integration of Eq. 5.3, namely

$$y_j^{n+1} = y_o^n + \sum_{j=1}^{N_x} \left(\frac{u_y}{u_x} \right)_j^n \left(x_j^n - x_{j-1}^n \right) \qquad (5.4)$$

In Eq. 5.4 y_j corresponds to the updated y-coordinate at the corresponding nodal point at each iteration (denoted by the superscript n), y_o is the y-coordinate of point A (at $x=0$) in Fig. 5.1, x_j-x_{j-1} the distance between two successive nodal points of boundary AB in the x-direction and N_x the number of nodes in the x-direction. Having determined a new shape of
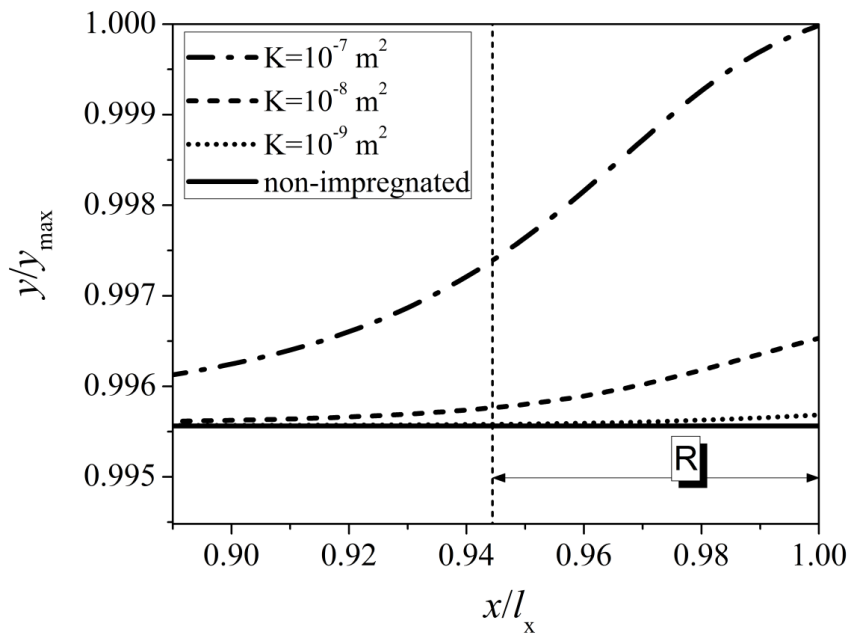
Figure 5-4: Infiltration depth profiles (convergent shapes of line AB) plotted along a 2R distance for three different permeabilities $K=10^{-7}$, 10^{-8} and 10^{-9} m^2. For the cases shown here, L_o=2 mm, R=5 mm, V=0.15 m/s and μ=1000 Pa·s. The horizontal axis is scaled with the l_x length of the computational domain and the vertical distance is scaled with the maximum y_{max} (i.e. $y_{max}=l_y+L_o+h_f$) length obtained at $x/l_x=1$ for $K=10^{-7}$ m^2. The final

penetration depth (h_f) for each K is the vertical distance of each convergent shape (at $x/l_x=1$).

boundary AB and thus a new flow domain, a new finite volume mesh is constructed and the Stokes, Brinkman and continuity equations are solved again. The new velocity field is used to correct the shape of the boundary AB through Eq. 5.4. The procedure continues until the normal velocity across boundary AB, as determined by the predictor step, is less than a prescribed tolerance (typically $\varepsilon=10^{-6}$), namely

$$\frac{1}{N_x}\sqrt{\sum_{j=1}^{N_x}u_{n\,j}{}^2} \leq \varepsilon \qquad (5.5)$$

Representative infiltration profiles are shown in Fig. 5.4 for $K=10^{-7}$, 10^{-8} and 10^{-9} m^2. The horizontal axis is non-dimensionalized with the length l_x of the computational domain and the vertical axis with y_{max} where $y_{max}=l_y+L_o+h_f$. The vertical distance of the computed curves from the initial state (at $x/l_x=1$) corresponds to the penetration depth h_f. As expected, increasing the permeability of the porous substrate facilitates resin infiltration. It is interesting to observe that for the case of a relatively permeable substrates (i.e. $K=10^{-7}$ m^2) the presence of the pin causes a larger disturbance in the flow field which results in the impregnation of the substrate commencing well ahead of the pin.

5.4   Results and Discussion

5.4.1   Velocity Profiles and Pressure Field

In this section we outline the structure of the flow field in the region of interest – that is, within the resin wedge between the pin and the moving substrate. The locations where velocity profiles are shown are given in Fig. 5.5a and Fig. 5.5b. The variation of the velocity u_x across the gap at the locations of Fig. 5.5a is shown in Fig. 5.6 where u_x is scaled with the maximum velocity $u_{x,max}$ for the four locations shown in the figure. The

81
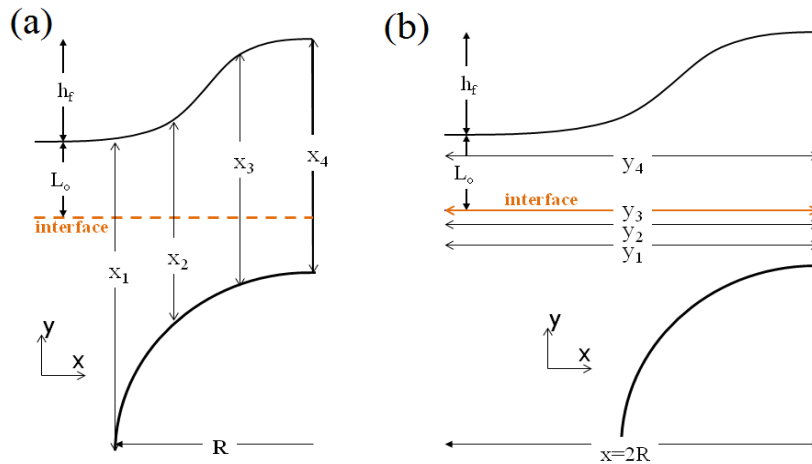
Figure 5-5: Schematic representation of different directions on which the (u_x, u_y) velocity components are plotted (a) corresponds to u_x and (b) for u_y (note: $y_1=\delta/2$). Figure not to scale.

shape of the velocity profile at $x=x_1$ is indicative of a drag flow opposed by a pressure gradient. This pressure gradient is formed as the fluid dragged by the moving substrate is squeezed to pass through the narrow gap within the wedge-shaped region. As a result of this pressure gradient, a back-flow develops which opposes the drag flow caused by the movement of the porous substrate. This effect is also present at locations far beyond the wedge-shaped region. At intermediate locations within the wedge (i.e. $x=x_2$ and $x=x_3$) the
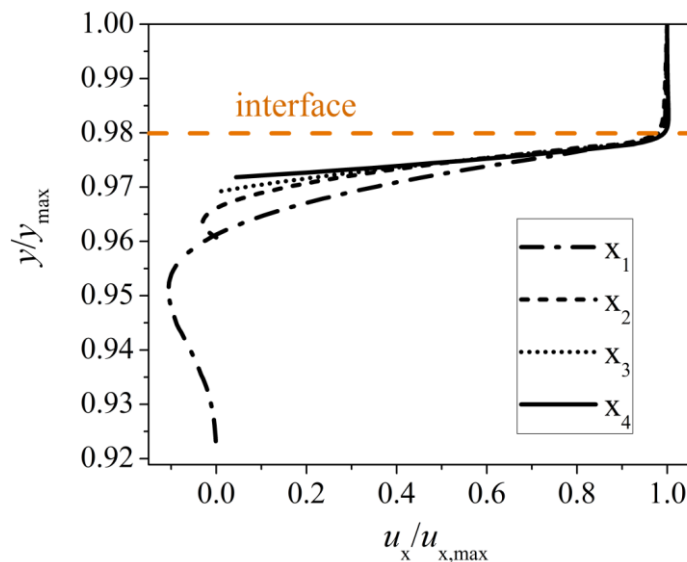
Figure 5-6: Dimensionless velocity profiles u_x along the lines denoted in Fig. 5.5a. The vertical axis is scaled with y_{max} and the horizontal axis scaled with $u_{x,max}$ (i.e. the maximum velocity in the x-direction). Towards the cylinder zero tangency point the flow becomes nearly simple shear and $u_{x,max}$ is obtained inside the porous substrate where roughly $u_{x,max}=V$ with V the substrate pulling speed. Profiles shown for $K=10^{-8}$ m^2, $R=5$ mm, $L_o=2$ mm, $V=0.15$ m/s and $\mu=1000$ Pa·s.

effect of the opposing pressure gradient becomes less pronounced, until at the point of minimum separation ($x=x_4$) the flow becomes simple shear, as expected. In Fig. 5.7 the transverse u_y velocity profiles are shown for the locations of Fig. 5.5b. At $y=y_1$ we observe negative transverse velocity values (fluid moving downwards and away from the resin/substrate interface) - this reflects the two-dimensional nature of the combined drag- and pressure-driven flow. Positive u_y values – fluid moving towards the substrate – predominate within the wedge and as we approach the zero tangency point; this eventually causes the resin to infiltrate into the substrate. Within the substrate only positive u_y velocity values are observed. These results suggest that there is a significant amount of fluid that moves away from the porous substrate and the pin as a result of the back-flow caused by the pressure build-up in the wedge. For this reason, not all fluid dragged by the substrate approaches the pin and even less will eventually penetrate into the substrate. The relative amounts – fluid dragged by the substrate vs. fluid actually penetrating into it - depend primarily on the permeability of the substrate as more permeable media imply ease
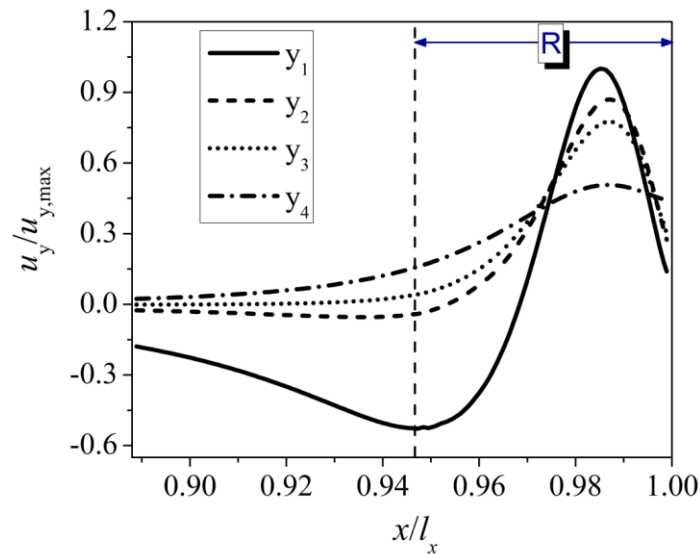
Figure 5-7: Dimensionless velocity profiles u_y along the lines denoted in Fig. 5b. The vertical axis is scaled with $u_{y,max}$ (which is obtained for the y_1 line roughly near the zero tangency point) and the horizontal axis scaled with l_x (i.e. the length of the computational domain see Fig. 2). Profiles shown for $K=10^{-8}$ m^2, $R=5$ mm, $L_o=2$ mm, $V=0.15$ m/s and $\mu=1000$ Pa·s.

of fluid penetration and therefore low tendency for back flow. This concept is important in formulating a general model for the fluid penetration process, as will be shown in section 5.4.2 below.

83

Figure 5.8 shows representative pressure profiles when both K and L_o vary. Pressures corresponding to larger values of L_o would be representative of conditions downstream in a pin array. For $K=10^{-7}$ m^2 and $L_o=1$ mm (Fig. 5.8a) or $L_o=4$ mm (Fig. 5.8b) the maximum generated pressure is observed in a region located roughly at the middle of the formed wedge. The different thicknesses of the pre-impregnated zone appear to effect the maximum pressure appreciably (for $L_o=1$ mm $P_{max}\approx0.26$ MPa while for $L_o=4$ mm $P_{max}\approx0.34$ MPa). For the same value of L_o and $K=10^{-9}$ m^2 (in Fig. 5.8c) the maximum pressure increases markedly to $P_{max}\approx1.12$ MPa from the value of $P_{max}\approx0.26$ MPa shown in Fig. 5.8a, accompanied by a shift of its location closer to the zero tangency point.
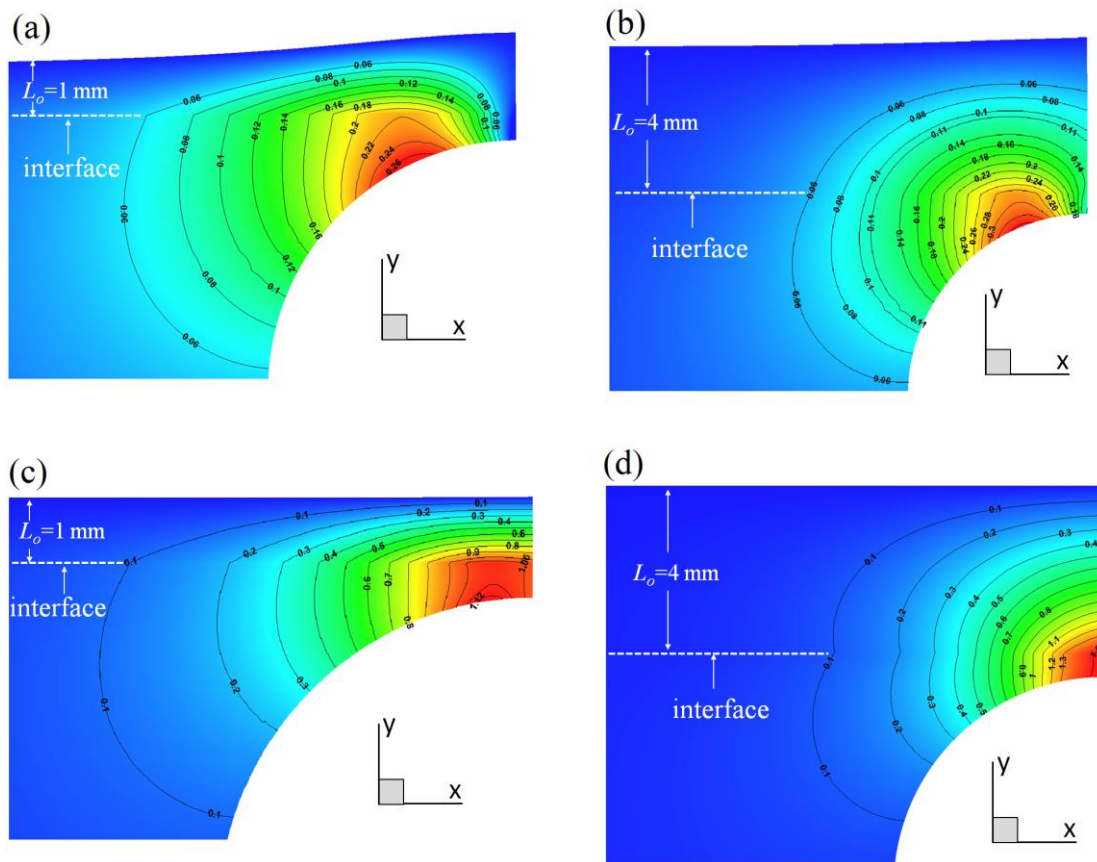
Figure 5-8: Pressure field for $K=10^{-7}$ m^2 and $L_o=1$ mm (a), $L_o=4$ mm (b). For $K=10^{-9}$ m^2 and $L_o=1$mm and $L_o=4$ mm the pressure fields are shown in (c) and (d) respectively. Results are shown for $R=5$ mm, $V=0.15$ m/s and $\mu=1000$ Pa·s.

5.4.2 A General Impregnation Model

In [12] it was rigorously shown that, in a single-pin process, the resin penetration depth is affected by different operating and geometric parameters through power-laws in terms of the dimensionless quantities $\sqrt{\delta/L_o}$, $L_o/\sqrt{K}$ and L_o/R. However, no general

84

law (expressing penetration depth in terms of the combined influence of all pertinent parameters in a single explicit model) was proposed. Further, the pressure level in the wedge was not included in the proposed correlations, which were applicable only for single-pin operations. In the present section we present a general scaling which (*i*) expresses the extent of resin infiltration as a function of one single dimensionless group and (*ii*) is applicable in multi-pin systems.

Our reasoning is based on mass balance considerations in the wedge region shown Fig. 5.1. If Q_{in} is the fluid flow rate (per unit width) entering the wedge and Q_p and Q_d the fluid flow rate (per unit width) entering the porous roving and exiting the wedge respectively, it is obviously $Q_{in}=Q_d+Q_p$. If an average pressure is assumed in the wedge (this can be computed from the pressure profile $P(x)$ as $\overline{P} = (1/L_x)\int\limits_{L_x} P(x)dx$ where $L_x=R$),

an average thickness of saturated zone (this can be $\sim L_o$) over which this is applied, and if K and μ are the permeability of the roving and the viscosity of the resin, it is $Q_p \approx K\overline{P}R/\mu L_o$. If simple shear is assumed at the zero tangency point (this is not far from reality, see Fig. 5.6), the fluid flow rate (per unit width) exiting the wedge is $Q_d \sim V\delta$. Obviously, the dimensionless group defined by the ratio Q_d/Q_p is of interest and we define it as $\Lambda=\mu V\delta L_o/\overline{P} KR$. This is not much different to the dimensionless group introduced by Ahn and Seferis [17] – the Prepreg Flow Number ($PFN= KP_{eff}/\mu VY_f$) – in which P_{eff} the effective pressure is equivalent to our average pressure, and the thickness Y_f of the fiber tows to be impregnated similar to our L_o.

In the following we will present how our computational results scale with the dimensionless quantity Λ. A large number of simulations ($\sim$250) have been carried out in which operational conditions, geometrical characteristics and fluid or porous substrate parameters varied as 0.03 m/s$<V<$0.2 m/s, 2 mm$<R<$8 mm, 0.1mm$<\delta<$0.6mm, 0.1mm$<L_o<$3mm and 10^{-7}m$^2<K<10^{-10}$ m^2 [6-11]. When the h_f results are plotted in terms of
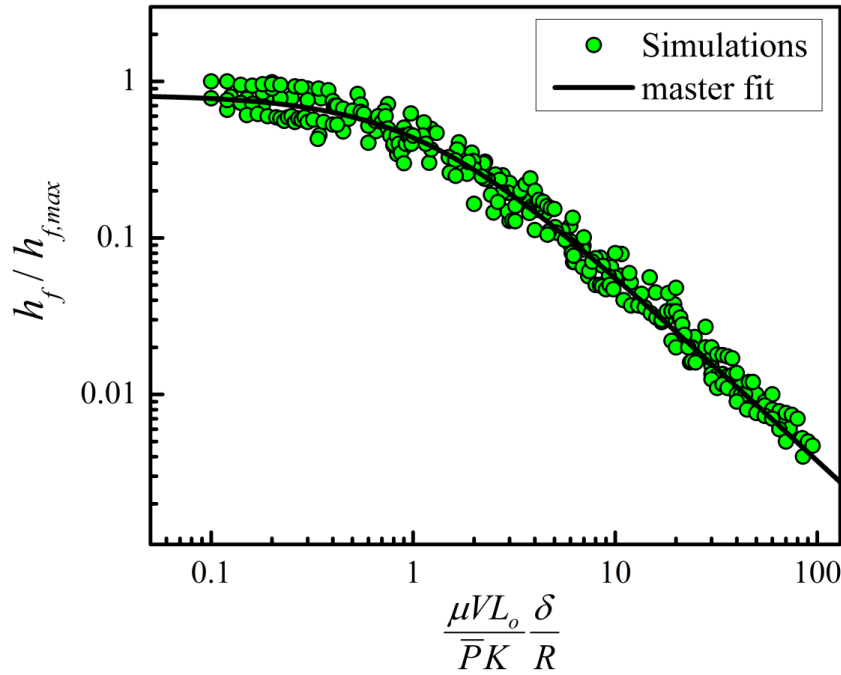
Figure 5-9: Master curve, expressing the effect of the dimensionless group $\Lambda=\mu V L_o \delta/PKR$ on the resin infiltration depth h_f. The vertical axis is scaled with $h_{f,max}$ that corresponds to the maximum infiltration depth obtained directly from the simulations for the lowest value of Λ ($\Lambda_{min}\approx0.1$).

the dimensionless group Λ, a master curve is revealed, as shown in Fig. 5.9 in which eachdata point corresponds to one simulation. Fig. 5.9 suggests that decreasing values of Λ facilitates resin infiltration up to a plateau value for roughly $\Lambda<0.1$. Qualitatively this is logical, given our definition of Λ as the ratio Q_d/Q_p – a successful impregnation process will occur when $Q_p>>Q_d$. Higher values lead to poorer resin infiltration. The data in Fig. 5.9 suggest a power-law of the form

$$\frac{h_f}{h_{f,max}} = \frac{1}{1 + A\left(\dfrac{\mu V L_o}{\overline{P}K}\dfrac{\delta}{R}\right)^B}$$

(5.6)

where the parameters $h_{f,max}$, A and B are found by standard non-linear data fitting to be $A=0.879\pm0.011$, $B=1.2\pm0.1$ and $h_{f,max}=8.21\times10^{-4}\pm0.0005$ m.

The master curve of Eq. 5.6 may be used to obtain an estimate of the penetration depth at different process conditions. Obviously, existence of a model such as Eq. 5.6 would allow for material/process conditions (μ,K,V,R) to be adjusted so that pultrusion of similar quality (i.e similar impregnation depth) can be obtained even as material properties, process conditions and pin characteristics change. However, Eq. 5.6 is still somewhat difficult to apply to a real process, because, along with δ, the average pressure in the wedge is usually unmeasurable and unknown. Instead, the tensioning force T on the

86

substrate is readily measured and typically reported in published experimental studies. Force balance arguments indicate that $T \sim \overline{P}WL_o$ where W is the width of the roving [10]. Using this, a suitable dimensionless group similar to Λ, which includes the tensioning force T is $\Pi = \mu V W L_o^2 \delta / TKR$. We will use this number in the following parametric studies and in comparing with experimental data.

5.4.3 Extension of the Impregnation Model to a multi-Pin Arrangement

Equation 5.6 above can also be used to evaluate the total resin infiltration L_f achieved in a sequential arrangement of pins. Key to this is the inclusion of the parameter L_o (see Fig. 5.2) in the simulations from the results of which Eq. 5.6 was derived/proposed. At the Nth pin, the thickness of the saturated zone L_0^N within the roving as it approaches the pin will be equal to the infiltration depth achieved at the previous pin, namely:

$$L_o{}^N = L_o{}^{N-1} + h_f{}^{N-1} \tag{5.7}$$

Additionally, the operation of the Nth pin will increase the resin infiltration depth by h_f^N, so that

$$L_f{}^N = L_0^N + h_f^N = L_0{}^N + \frac{8.21 \times 10^{-4}}{1 + 0.879\left(\dfrac{\mu V (L_o^N)^2}{TK} \dfrac{W\delta}{R} \right)^{1.2}} \tag{5.8}$$

where the superscript N indicates the Nth pin in a sequence and where Eq. 5.6 has been used and the dimensionless group Λ is substituted by the Π group discussed in the previous section. The predictions of Eq. 5.8 are shown in Fig. 5.10, where $K=10^{-9}$ m^2, $T=20$ N, $W=10$ mm, $R=5$ mm and $\delta=500$ μm and the number of pins, the fluid viscosity and the

(a)

(b)
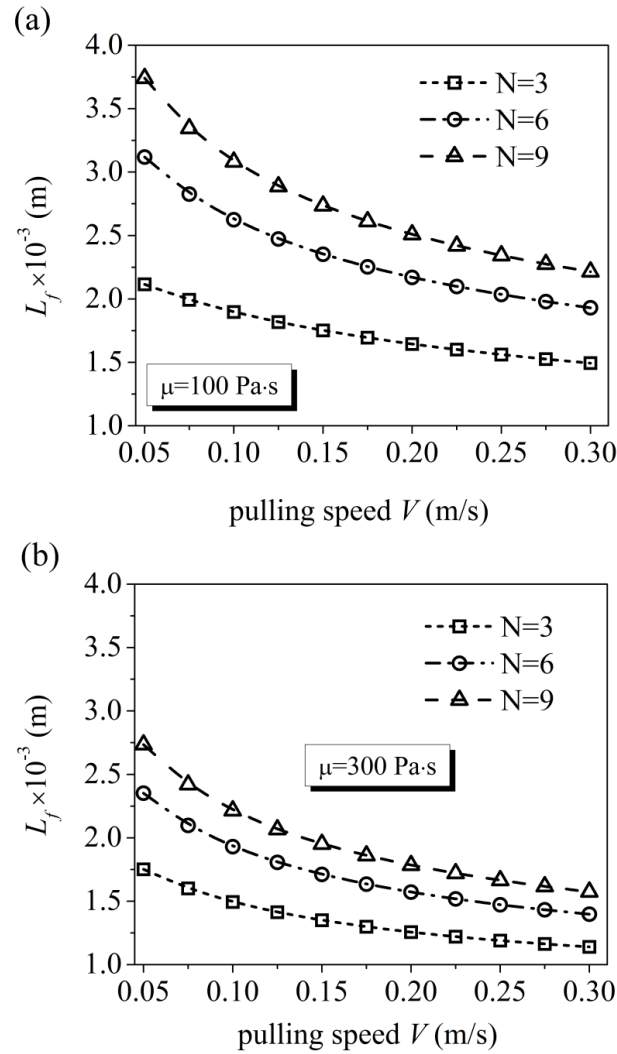
Figure 5-10: Predictions of Eq. 5.8 for the effect of pulling speed V and number of pins N on the final achieved infiltration depth L_f for arrays of N=3, 6 and 9 pins with (a) μ=100 Pa·s and (b) μ=300 Pa·s. Both cases shown for K=10^{-9} m^2, T=20 N, W=10 mm, R=5 mm and δ=500 μm.

pulling speed are variable; 3<N<9, and μ=100 Pa·s, 300 Pa·s. A first observation is that by increasing V the infiltration depth decreases, irrespective of the number of pins or the fluid viscosity. On the other side, use of more pins improves impregnation. These predictions are in total agreement with the trends of the experimental results of [6] and [9]. In Fig. 5.10 the effect of the fluid viscosity is also shown. Increasing μ from 100 Pa·s (Fig. 5.10a) to 300 Pa·s (Fig. 5.10b) decreases the infiltration depth for all pulling speeds. This behavior is also in agreement with the experimental observations reported in [9].

(a)

(b)
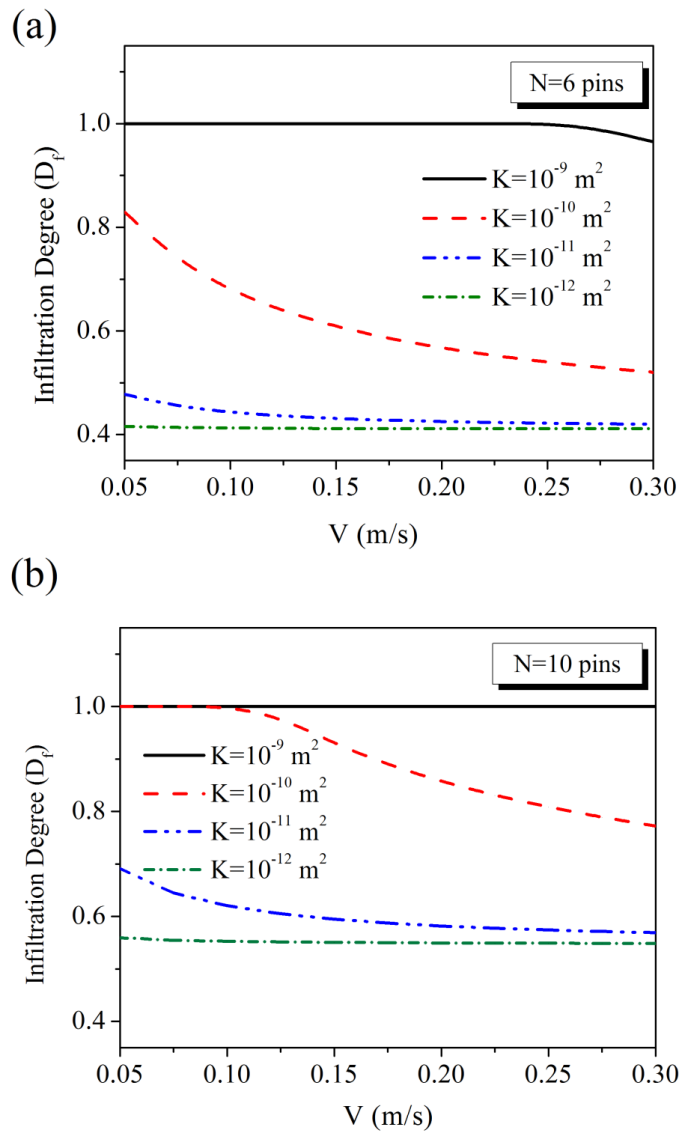
Figure 5-11: Predictions of Eq. 5.8 for the effect of the permeability on the infiltration degree D_f as a function of the pulling speed V for a substrate of thickness H=1.5 mm. (a) N=6 and (b) N=10 pins. The infiltration degree is denoted as $D_f=L_f/H$. For D_f=1 full impregnation of the substrate is accomplished. All cases are plotted for T=20 N, W=10 mm, R=5 mm and δ=500 μm.

The efficacy of resin infiltration can also be expressed through an Infiltration Degree [9], defined as $D_f=L_f/H$, where H is the total thickness of the porous substrate (D_f=1 would indicate complete saturation of the substrate). Results are shown Fig. 5.11. Two different pin arrangements are used and H=1.5 mm is assumed. For N=6 (Fig. 5.11a) and for a relatively permeable substrate (K=10^{-9} m^2) full impregnation of the substrate is predicted for V up to 0.25 m/s. As expected, the D_f decreases with decreasing K. For permeabilities low enough so that D_f<1 (e.g. K=10^{-10} m^2) D_f is predicted to decrease as V increases, in agreement with the tendencies shown in Fig. 5.10. For lower values of

permeability ($K=10^{-11}$ m^2 and $K=10^{-12}$ m^2) only about 50% impregnation is predicted. The predictions for $N=10$ are shown in Fig. 5.11b. For $K=10^{-9}$ m^2 and for low pulling speeds (V up to 0.12 m/s) a full impregnation is predicted; D_f decreases for higher pulling speeds. The results for $K=10^{-11}$ m^2 and $K=10^{-12}$ m^2 are shown to shift upwards when compared to the corresponding ones of Fig. 5.11a implying a higher degree of fluid infiltration into the substrate as the number of pins increases. The above results show that higher V lowers the achieved infiltration depth. Pulling speed is important as it impacts directly the production rate and thus the economics of a pultrusion line. The usefulness of a model such as the one expressed by Eq. 5.8 is that it can give an estimate of the combined effect of the various operating conditions and thus an option of potentially achieving both, a high production rate and the desired degree of impregnation.

5.4.4 Comparison with Experimental Data

In the following we compare the predictions of Eq. 5.8 with experimental results available in the technical literature. A direct comparison with experiment is difficult, since only a limited number of usable results are found in the open literature and, also, because in all experimental studies only some of the process parameters appearing in Eq. 5.8 are known/reported. For this reason, at best semi-quantitative or even just qualitative comparison is possible; however, this is still valuable since it will reveal whether the predictions of Eq. 5.8 follow the trends shown in experiment.

In Fig. 5.12 we compare the predicted effect of the number of pins N on the infiltration degree D_f for various values of R to the data of Bates and Zou [9]. Dashed lines represent the predictions of Eq. 5.8. In [9] $V=0.1833$ m/s and we have assumed $T=20$N, $\mu=100$ Pa·s, $W=10$ mm and $\delta=0.5$ and $K=10^{-9}$ m^2. The latter values are not reported in [9] but are typical of those used in earlier studies [8,10,11] by the same authors - thus we use them in all subsequent comparisons. Since some value for the total thickness of the substrate H has to be assumed in order to compare with the results of [9], we assume that for for $R=2.5$ mm full impregnation ($D_f=1$) is accomplished for $N=8$. In spite of all uncertainties, the predictions of Eq. 5.8 give similar trends and fall within the data range of the experimental results reported in [9]. It is interesting to observe that for R=5 mm and R=7 mm the predictions of Eq. 5.8 compare very good with the experimental results from [9].
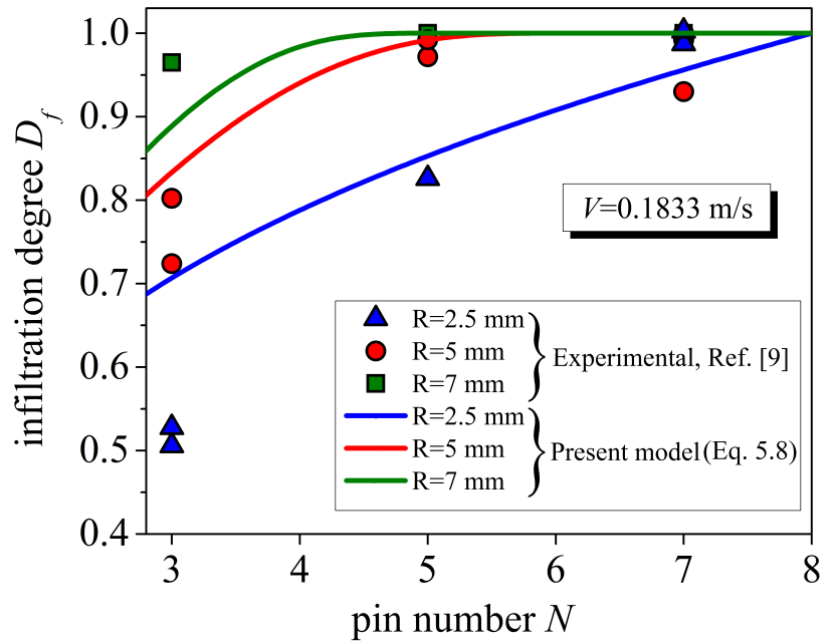
Figure 5-12: Effect of the number of pins N and pin radius R on the infiltration degree D_f. Symbols correspond to experimental results reproduced from Bates and Zou [9] and lines predictions by Eq. 5.8 for V=0.1833 m/s. Assumed parameters for the theoretical predictions of Eq. 5.8: $K=10^{-9}$ m^2, $T=20$ N, $W=10$ mm and $\delta=500$ μm.

Another parameter usually reported in experimental data is the contact (or residence) time [6,7,11], defined as $t=R/V$. This expresses the time each segment of the roving stays in contact with the wedge region (where higher pressures and thus resin infiltration occur). Comparisons are shown in Fig. 5.13 for two different pin numbers ($N=2$ and $N=7$) for V ranging similar to [9] between 0.035 m/s and 0.5 m/s and pin radii ranging from 2 mm to 7 mm. As a result the contact time takes a range of values from 0.004 sec, to 0.2 sec. We note that based on the trend of the experimental results of [9] we have assumed that the maximum infiltration degree ($D_f=1$) is achieved at a critical time $t_{cr.}=0.06$ sec. The predictions of our model appear to produce similar trends as do the experimental results of [9].

Figure 5.13.:Infiltration degree D_f as a function of the contact time ($t=R/V$) of the porous substrate with the pin. Symbols are experimental results reproduced from Bates and Zou [9]. Continuous line corresponds to predictions by Eq. 5.8 for $N=2$ and dashed line for $N=7$. Pulling speed range $V=0.035$ m/s~0.5 m/s and $R=2$ mm~7 mm. Assumed values for the model (Eq. 5.8): $K=10^{-9}$ m^2, $T=20$ N, $\mu=100$ Pa·s and $\delta=500$ μm.

Figure 5.14: Infiltration degree D_f as a function of the pin radius for two pulling speeds V and different number of pins N. Symbols are experimental results reproduced from Bates and Zou [9] for $N=3$. Continuous lines correspond to predictions by Eq. 5.8 for $N=3$ and dashed lines for $N=9$. Assumed values for the model (Eq. 5.8): $K=10^{-9}$ m^2, $T=20$ N, $\mu=100$ Pa·s and $\delta=500$ μm.

Figure 5.15: Infiltration degree D_f as a function of the pulling speed V for different number of pins. Symbols are experimental results reproduced from Bates and Zou [9] for R=5 mm. Lines correspond to predictions by Eq. 5.8 for different numbers of pins. Assumed values for the model (Eq. 5.8): K=10^{-9} m^2, T=20 N, μ=100 Pa·s and δ=500 μm.

In Fig. 5.14 we compare the predictions of our model concerning the effect of R, N and V with the experimental results of Bates and Zou [9]. Increasing R (for a specific pulling speed V) or the number of pins N or decreasing the pulling speed V increase the infiltration of the fluid into the substrate. To create a reference point in our comparisons with the data of [9] we have again assumed that complete impregnation for V=0.1166 m/s is achieved for R=5 mm and at V=0.1833 m/s complete impregnation is achieved for R= 8 mm. Clearly the trends predicted by Eq. 5.8 are similar to those of the experimental results of [9]. Good agreement of the infiltration degree as a function of the pulling speed and for different number of pins N utilized is also shown in Fig. 5.15 with experimental results from [9]. When more pins are employed variations in the pulling speed cause a small to no effect on the infiltration degree because the large number of pins is capable of fully impregnating the substrate at low pulling speeds.

5.5 Conclusions

Using the results of approximately 250 simulations for the pin-assisted pultrusion process we have derived a simple, explicit model which relates the extent of resin infiltration h_f to a dimensionless group $\Lambda=\mu V L_o \delta / \overline{P} KR$ incorporating key material and process parameters. This relationship is found to be a power function of Λ, namely

$h_f = C/(1 + A\Lambda^B)$, where A, B and C are obtained from non-linear data fitting. An alternative formulation, in which the tensioning force T is included, utilizes a modified dimensionless group, namely $\Pi = \mu V W L_0^2 \delta / TKR$. The model has been extended to multiple pin arrangements, making use of the fact that the simulations have allowed for some section of the roving (thickness L_o) to be saturated with resin prior to approaching the pin. Following this, we have presented the results of an extensive parametric analysis as well as comparisons with published experimental data. Specifically, our model predicts decreasing h_f as pulling speed V and resin viscosity increase, and increasing h_f as the number of pins or the permeability of the roving increase. To account for rovings of finite thickness, we also express our results in terms of a dimensionless infiltration degree $D_f = h_f/H$ and compare the predictions of our model concerning the effect of pin radius, number of pins and the effect of contact time to the experimental results of [9]. Our predictions are found to be at least semi-quantitatively correct, definitely showing the same trend as the experimental data, in spite of the large uncertainties in the values of some process parameters.

5.6 References

1. P. Simacek and S.G. Advani, *Compos. A*, 72, 115 (2015).

2. F.R. Phelan JR, *Polym. Compos.*, 18, 460 (1997).

3. L. Joubaud, V. Achim and F. Trochu, *Polym. Compos.*, 26, 417 (2005).

4. P. Peltonen, K. Lahteenkorva, E.J. Paakkonen, P.K. Jarvela and P. Tormala, *J. Therm. Compos. Mater.,* 5, 318 (1992).

5. P. Peltonen and P. Törmälä, *Compos. Struct.*, 27, 149 (1994).

6. H. Bijsterbosch and R.J. Gaymans, *Compos. Manuf.*, 4, 85 (1993).

7. R.J. Gaymans and E. Wevers, *Compos. A*, 29, 663 (1998).

8. P.J. Bates and J.M. Charrier, *J. Therm. Compos. Mater.*, 12, 276 (1999).

9. P.J. Bates, X.P. Zou, *Int. Polym. Process.*, 17, 376 (2002).

10. P.J. Bates and J.M. Charrier, *Polym. Compos.*, 21, 104 (2000).

11. P.J. Bates, J. Kendall, D. Taylor, and M. Cunningham, *Compos. Sci. Technol.*, 62, 379 (2002).

12. N.D. Polychronopoulos and T.D. Papathanasiou *, Compos. A*, 71, 126 (2015).

13. G.H. Neale and N.K. Nader, *AIChE J.*, 20, 530 (1974).

14. D.F. James and A.M.J. Davis, *J. Fluid Mech.*, 426, 47 (2001).

15. M.F. Tachie, D.F. James and I.G. Currie, *J. Fluid Mech.*, 493, 319 (2003).

16. J.A. Ochoa-Tapia and S. Whitaker, *Int. J. Heat Mass Transf.*, 38, 2635 (1995).

17. K.J. Ahn and J.C. Seferis, *Pol. Eng. Sci.*, 33, 1177 (1993).

Chapter 6

Fluid Penetration in a Deformable Permeable Web Moving Past a Stationary Rigid Solid Cylinder

(Submitted in: *Transport in Porous Media*)

Abstract

We present an analysis for the process of fluid infiltration into a deformable, thin and permeable web that moves in close proximity over a rigid and stationary solid cylinder. While this is a process of significant interest in a range of coating, printing and composites pultrusion processes, its hydrodynamics have received limited attention in the open literature. The flow in the film separating the web from the cylinder is described by lubrication theory, while fluid transfer into the web is governed by Darcy's law. The deformation of the web at each position is a linear function of the local gap pressure; this is consistent with the assumption of a thin and rigidly supported web. Our results indicate that the web/fluid interface is forced away from the cylinder surface as it approaches it and bounces back downstream from the minimum separation point. This behavior produces a non-symmetric gap between the adjacent surfaces, and this is shown to have critical influence on the final amount of penetrating fluid. The extent of fluid penetration is also found to be affected by the web elasticity E and permeability K where under a specific E, K combination a maximum penetration depth is obtained.

6.1 Introduction

Deformable permeable webs are frequently encountered in a broad range of industrial processes, such as in coating, printing and composites pultrusion, for the manufacturing of a diverse type of products ranging from plastic sheets, paper, filters, textiles to solar cells and electronic films. Such processes are characterized by the deposition and penetration of a thin liquid layer onto a moving deformable permeable web; this is usually achieved utilizing combinations of rotating or stationary cylinders as well as moving or stationary non-cylindrical parts. The thin liquid film during the operation of the processes is mainly situated in the small non-uniform gap formed by the flexible

permeable web that moves in close proximity to the rotating/stationary parts of the machine.

Depending upon the application, simple rotating cylinders are used in the roll-coating technology (e.g., Benkreira et al. 1981; Coyle et al. 1990), while complex ones with circumferentially engraved micro-cavities in gravure printing or gravure coating (e.g., Benkreira and Patel 1993; Kapur 2003; Hewson et al. 2011). Non-rotating parts may be also utilized such as slit dies in slot-die coating where the liquid is injected from a slit die towards a closely moving web (e.g. Romero et al. 2004; Sandström et al. 2012) or blades in blade coating (e.g. Sullivan et al. 1987). A configuration which is frequently used in the roll-coating technology may consist of a pair of solid rigid rolls or a roll pair one of which may be covered with a compliant layer (i.e. rubber band) that usually supports the flexible web (e.g. Coyle 1988). This is also a common practice in the direct gravure printing/coating technology a variation of which entails a single gravure roll in close distance with the web. Production lines with deformable roll configurations are of significant interest in the coating/printing industry since they minimize the risk of clashing the two rigid rolls and produce much thinner films compared to rigid roll systems. Thus, the need to study the liquid flow in such configurations from either a mathematical or experimental perspective becomes important.

The flow in the roll coating/printing processes with deformation of the roll supporting the flexible web has been studied theoretically (e.g., Carvalho and Scriven 1997; Carvalho 2003; Gostling et al. 2003; Yin and Kumar 2005; Yin and Kumar 2006; Lécuyer et al. 2009; Lee and Na 2009) and experimentally (e.g., Cohu and Magnin 1997; Ascanio et al. 2004; Ascanio and Ruiz 2006). A substantial amount of numerical studies regarding web deformation has been also carried out to describe the flow in coating processes where non-rotating parts are present, as for instance in slot-die coating configurations (e.g., Madasu and Cairncross 2003; Madasu 2009; Nam and Carvalho 2010). The essential tenets of lubrication approximation to describe the fluid flow in the thin gap was utilized with the deformation of the flexible web or deformable roller approximated to be directly proportional to the local pressure developed in the thin fluid film, as for instance in Yin and Kumar (2006), resulting in a non-symmetric gap. It is worth noting that the lubrication approximation along with the linear local pressure-deformation relation, finds applicability not only to modeling engineering processes, but also in various biological processes where soft biological surfaces are often in close relative motion. For instance, in Jones et. al (2008) it is utilized to describe the fluid flow

97

between the flexible eyelid wiper and ocular surface. Interesting theoretical and numerical work in Skotheim and Mahadevan (2004) and Skotheim and Mahadevan (2005) mainly for biological processes, also utilized the lubrication theory (Reynolds equation) by regarding different geometries comprised of soft materials of biological interest that can deform easily due to either geometry (e.g. shell) or constitutive properties (e.g. gel).

While the above-mentioned studies give useful insights regarding the fluid flow in the deformable gap, fluid transport into the permeable web has not been taken into account. Certain flexible web types (e.g. paper, filters and textile webs) have an inherent complex microstructure formed usually by discontinuous or continuous solid inclusions (e.g. thin fibers) which create a network of void spaces. The presence of such an architecture of free space in the web offers extra escape flow paths that the liquid during the coating process may follow. In this way an amount of liquid applied to the moving web will also penetrate and fill the formed void spaces to a certain extent due to the developed hydrodynamic pressure in the film as well as due to capillary pressure. Estimation of the fluid amount penetrating the permeable medium is a critical issue as it directly affects the properties and functionality of the final product or may aid into determining possible printability and runnability defects in coating and printing (e.g., Matilainen et al. 2012). In this context a number of numerical and experimental studies have attempted to quantify the extent of fluid penetration into a moving web, or in general a moving thin substrate, neglecting the web/substrate deformation. Hayes et al. (2000), utilized an integrated form of Darcy's equation and two dimensional Galerkin finite element method to describe color penetration into a moving paper web of a film coater. The applied pressure and the pressure to the pore scale were lumped together as an effective applied pressure which was approximated to obey an arbitrary uniform or linear non-uniform variation that forces the liquid to penetrate the web. In the studies by Farboodmanesh et al. (2005) and Yesilalan et al. (2010) an analytical approach was followed to study the penetration of neoprene latex coating and a polyurethane coating respectively, due to hydrodynamic pressure development, into a thin fibrous fabric during blade coating. In the modeling approach using lubrication approximation the pressure distribution on the permeable substrate was approximated based on the pressure distribution when coating a solid substrate and a one-dimensional Darcy's law was employed to describe the fluid infiltration to the substrate. More recently, studies regarding the penetration of a Newtonian and a non-Newtonian fluid into a rigid permeable substrate during slot die coating have been also carried out. In the study by Ding et al. (2013), an analytical penetration model for slot die coating was

98

derived based on a coupled form of lubrication equation, from which the pressure profile in the gap was obtained, and Darcy's law to describe the penetrating flow. The analysis was extended (Ding et al. 2014) by taking into account the capillary pressure in the permeable medium.

In the composites manufacturing technology flexible fibrous substrates (e.g. made up of glass or carbon fibers), such as woven textiles, may be pulled between a sequential array of solid stationary cylinders (pins) located in a liquid bath which is often a low viscosity polymer resin (Gibson and Mänson 1992). The movement of the fibrous substrate in close proximity to the cylinders results in a pressure build-up which eventually forces the fluid to convey into the permeable substrate and impregnate it (Bates et al. 2002). Some numerical studies utilized an integrated form of Darcy's law to predict the amount of liquid penetrating into the fibrous substrate (e.g., Bijsterbosch and Gaymans 1993; Gaymans and Wevers 1998). Other numerical works entailed a combination of the lubrication theory and Darcy's law to quantify liquid penetration in the substrate (Bates and Zou 2002) or a more realistic two-dimensional approach by coupled solution of Stokes and Brinkman equation (Polychronopoulos and Papathanasiou 2015). In the above-mentioned studies possible deformation of the substrate was neglected.

A numerical study followed by Chen and Scriven (1990) aimed towards the prediction of liquid penetration into a deformable permeable substrate for a nip-blade coating process by combining a modified lubrication theory and Darcy's law to describe the penetration flow. The deformable permeable substrate was assumed to be in contact with a rigid solid cylinder from one side and exposed to the liquid from the other side. It was also assumed that the substrate undergoes compression as it travels through the nip region between the rollers before reaching the blade section. In the work by Devisetti and Bousfield (2010) a numerical approach was followed to describe the fluid flow during fluid absorption in forward roll coating of a permeable porous web. The flexible permeable web was assumed to be in contact with a compliant rubber layer covering a rigid roller on the one side and exposed to the liquid from the other side. The deformation of the web was modeled using the same ideas as in Ref. 10 based on the assumption that the local web deformation is a linear function of local pressure. Results also included experimentally measured pressure distribution and final film thickness being in overall good agreement to the model predictions.

The objective of the present work is to examine the combined effects of deformability and permeability of a web moving past a rigid stationary cylinder. This is

99

carried out using a modified lubrication flow approximation with Darcy's law to describe the fluid motion into the web. The rest of the paper is structured as follows. In Sec. 6.2 we formulate the problem and the governing equations for the flow in the gap and through the web. In Sec. 6.3 we present results for i) a deformable and impermeable web, ii) a completely rigid and permeable web and iii) a web with combined deformability and permeability effects. Finally, we summarize our findings in Sec. 6.4.

6.2   Problem Formulation

We consider a rigid stationary solid cylinder of radius R, which is fully immersed in a Newtonian incompressible and isothermal fluid of viscosity μ, and in close proximity to a thin deformable permeable web moving with velocity V. Our description of the web as thin means that the web thickness H is smaller compared to other length scales in the problem
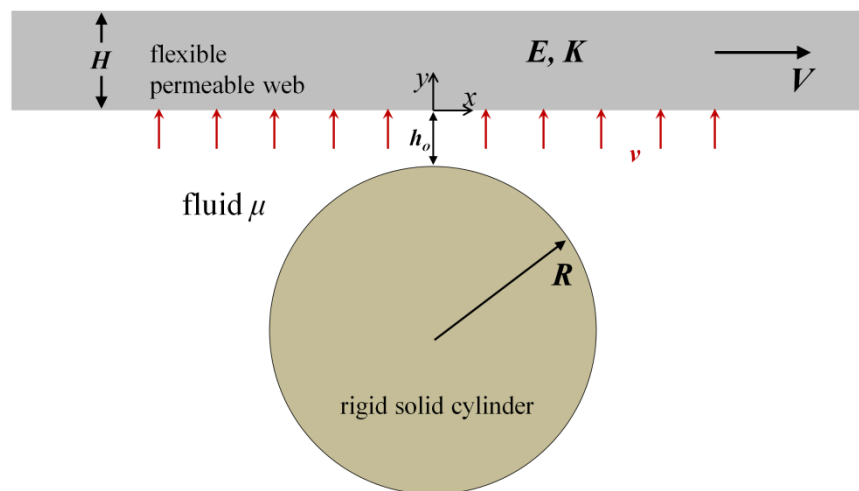
Figure 6-1: Schematic representation of the problem geometry prior to the web deformation or of the problem corresponding to a rigid web. The web with thickness H, Young modulus E and permeability K moves to the right with velocity V in close proximity h_o with a rigid solid stationary cylinder of radius R. The fluid of viscosity μ penetrates the web with penetration velocity v (denoted with the small vertical arrows). Figure not to scale.

such as the cylinder radius (i.e. $H \ll R$). The process under consideration, prior to any deformation of the web/fluid interface, is shown in Fig. 6.1 where h_o the minimum distance of the adjacent surfaces and x,y correspond to the longitudinal (web movement direction) and transverse (gap-wise) coordinates respectively. For the hydrodynamic description of the system we assume that the minimum gap length scale h_o is much smaller

than the cylinder radius ($h_o/R \ll 1$); this allows to use the classical lubrication approximation (Leal 2007) for the velocity field (u,v) in the gap. Under the above approximations the conservation of momentum equation reduces to

$$\frac{\partial p}{\partial x} = \mu \frac{\partial^2 u}{\partial y^2}, \quad \frac{\partial p}{\partial y} = 0 \tag{6.1}$$

and the continuity equation is

$$\frac{\partial u}{\partial x} + \frac{\partial v}{\partial y} = 0 \tag{6.2}$$

where $p=p(x)$ the pressure and u,v the velocity components in the x and y directions respectively. We use the no-slip condition at both the cylinder and web surface for the u velocity component

$$u(y = h) = 0, \, u(y = 0) = V \tag{6.3}$$

where $h=h(x)$ is the gap between the cylinder and the web. Since we confine the analysis to values of x such that $x \ll R$, a good approximation to $h(x)$ is

$$h(x) = h_o + \frac{x^2}{2R} + D(x) \tag{6.4}$$

where $D(x)$ in Fig. 6.2 is the gap change due to the web deformation. To model the deformation we follow an approach based on the coating/printing studies by Coyle (1988) and Yin and Kumar (2005) for deformable and non-permeable rolls, namely that the local deformation $D(x)$ is directly proportional to the local pressure of the fluid in the gap as

$$D(x) = \frac{H}{E} p(x) \tag{6.5}$$

where H the web thickness and E the Young modulus of the web. Obviously, in the limit of $E \to \infty$ the web behaves as rigid (i.e. $D(x)=0$) and the gap $h(x)$ is symmetric around the minimum separation point (see Fig. 6.1). For the v velocity component on the cylinder surface we set

$$v(y = h) = 0 \tag{6.6}$$

and on the web/fluid interface we apply Darcy's law (Bear 1988), which may be written as

$$v(y = 0) = -\frac{K}{\mu} \frac{dp}{dy} = -\frac{K}{\mu} \frac{p_{y=L} - p_{y=0}}{L} \tag{6.7}$$

where K the permeability of the web, $L=L(x)$ the penetration depth (see Fig. 6.3) at any position along the x direction in the web, $p_{y=0}$ corresponds to the hydrodynamic pressure at

the web/fluid interface and $p_{y=L}$ is the pressure within the void space of the porous medium right ahead of the penetrating fluid front (Chen and Scriven 1990). Following Hayes et al.

Figure 6-2: Schematic representation (near the region of minimum gap h_o) of the variation of the web/cylinder gap h(x). H is the web thickness and E and K its Young modulus and permeability respectively. The horizontal broken line corresponds to the web's surface in undeformed state (or rigid web, $E \rightarrow \infty$). The fluid of viscosity μ penetrates the web with penetration velocity v (denoted with the small vertical arrows). Figure not to scale.

Figure 6-3: Schematic representation (near the region of minimum gap h_o) of the fluid penetration depth $L(x)$ in the flexible web. The final penetration depth L_f corresponds to the accomplished depth of the penetrated fluid at some location away from the minimum gap h_o as the web moves to the right and leaves the cylinder behind. E Young modulus and K the permeability of the web.

(2000) the contribution of capillary pressure to $p_{y=L}$ may be neglected in light of the much higher hydrodynamic pressure developing in the gap. Under the assumption of lubrication approximation that the hydrodynamic pressure does not vary in the y direction we set $p_{y=0}=p$. Based on the above Eq. 6.7 takes the form

102

$$v(x, y = 0) = \frac{K}{\mu} \frac{p(x)}{L(x)} \tag{6.8}$$

which denotes that the fluid penetration is induced by the developed hydrodynamic pressure in the gap. In agreement with a number of relevant published works (e.g., Yesilalan et al. 2010; Ding et al. 2013), we treat the web as isotropic.

Following Ramon et al. (2013), we integrate Eq. 6.1 twice using the boundary conditions described in Eq. 6.3. We then substitute the result in Eq. 6.2 and integrating across the gap using the boundary conditions of Eq. 6.6 and 6.8 we obtain

$$\frac{d}{dx}\left(-\frac{h^3}{12\mu} \frac{dp}{dx} + \frac{Vh}{2} \right) + \frac{K}{\mu} \frac{p}{L} = 0 \tag{6.9}$$

where the gap h is given in Eq. 6.4 and for $K=0$ (i.e. non-permeable web) the classical lubrication equation may be recovered. As in Yin and Kumar (2005) the term in the parentheses of Eq. 6.9 corresponds to the fluid flow rate q through the gap per unit width. In Eq. 6.9 the penetration depth L on each x position is not known a priori and needs to be determined. Following Ding et al. (2013) we write the penetration velocity as $v=dL/dt=(dL/dx)(dx/dt)=(dL/dx)V$ so that Eq. 6.8 takes the following form upon rearrangement

$$\frac{dL}{dx} - \frac{K}{\mu V} \frac{p}{L} = 0 \tag{6.10}$$

In this way Eq. 6.9 and Eq. 6.10 form a system of differential equations the solution of which will give the gap pressure and penetration depth on each x position. To solve the system the following boundary conditions are imposed

$$p(-\infty) = p(+\infty) = 0 \quad \text{and} \quad L(-\infty) = 0 \tag{6.11}$$

for the pressure, which corresponds to setting the pressure far upstream and downstream equal to the baseline pressure of the system, and the penetration depth respectively. For convenience, we non-dimensionalize the variables using a length scale h_o, a velocity scale V and pressure scale $\mu V/h_o$ as

$$\hat{x} = \frac{x}{h_o}, \quad \hat{p} = \frac{h_o}{\mu V} p, \quad \hat{h} = \frac{h}{h_o}, \quad \hat{q} = \frac{q}{Vh_o} \quad \hat{K} = \frac{K}{h_o^2}, \quad \hat{L} = \frac{L}{h_o} \tag{6.12}$$

Equation 6.9 in scaled form may then be written as

$$\frac{d}{d\hat{x}}\left(-\frac{\hat{h}^3}{12} \frac{d\hat{p}}{d\hat{x}} + \frac{\hat{h}}{2} \right) + \hat{K} \frac{\hat{p}}{\hat{L}} = 0 \tag{6.13}$$

where the dimensionless gap flow rate per unit width is given by

103

$$\hat{q} = -\frac{\hat{h}^3}{12}\frac{d\hat{p}}{d\hat{x}} + \frac{\hat{h}}{2} \tag{6.14}$$

where

$$\hat{h} = 1 + S\hat{x}^2 + Ne\hat{p} \tag{6.15}$$

with

$$S = \frac{h_o}{2R} \tag{6.16}$$

and

$$Ne = \frac{\mu V H}{E h_o^2} \tag{6.17}$$

and Eq. 6.10 in scaled form

$$\frac{d\hat{L}}{d\hat{x}} - \hat{K}\frac{\hat{p}}{\hat{L}} = 0 \tag{6.18}$$

subjected to the scaled boundary conditions (Eq. 6.11) of

$$\hat{p}(-\infty) = \hat{p}(+\infty) = 0 \quad \text{and} \quad \hat{L}(-\infty) = 0 \tag{6.19}$$

The S parameter in Eq. 6.16 is the dimensionless minimum distance of the undeformed web from the cylinder surface. In Eq. 6.15 Ne is a dimensionless number that represents the ratio of viscous to elastic forces; increasing Ne results in a more deformable web while the limit $Ne \rightarrow 0$ (i.e. $E \rightarrow \infty$) corresponds to rigid web behavior.

We solve the system of Eqs. 6.13 and 6.18 subject to boundary conditions of Eq. 6.19 numerically using the bvp4c module from Matlab, for the different S, Ne and K values. The module is based on a finite difference method code that carries out a collocation method to obtain the solution of the boundary value problem. A key step for the implementation is to reduce Eq. 6.13 into a system of first-order differential equations and then supply the code with an initial guess for an initial mesh that reveals the behavior of the desired solution. The code subsequently adapts the mesh to obtain an accurate numerical solution with a modest number of mesh points. Mesh selection and error control are based on the residual of the continuous solution. The approximate solution is a cubic polynomial on each subinterval of the mesh, satisfies the boundary conditions and the differential equations at both ends and the mid-point of each subinterval and is fourth-order accurate (Shampine et al. 2000). We set the relative error tolerance to 10^{-6}. For rapid convergence of the solution we choose the function $\hat{p}_i(\hat{x}) = -2\hat{x}/(1 + S\hat{x}^2)^2$ as the initial guess for the pressure in the gap, which is the closed-form solution of Eq. 6.13 when the

104

web is rigid (Ne=0) and non-permeable ($\hat{K} = 0$). Since it is of physical interest to obtain the solution of the system of Eqs. 6.13 and 6.18, for a range of the parameter values, the continuation technique is used with Ne or $\hat{K}$ as continuation parameters.

6.3   Results and Discussion

6.3.1   Deformable and Non-Permeable Web

To gain a first insight of the process we regard the limiting case of a deformable and non-permeable ($\hat{K} = 0$) web. Certain aspects of this problem have been treated by Skotheim and Mahadevan (2005) for the deformation of a thin elastic layer coating a cylinder that moves over a rigid surface. Here, we assume that the cylinder is stationary and rigid and the moving surface (thin web) is deformable based on the fact that both
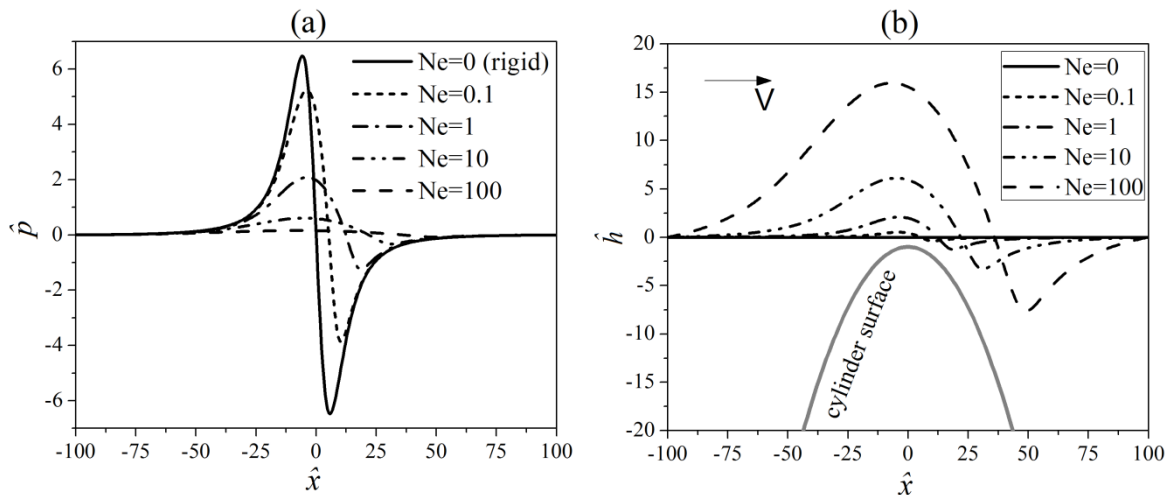
Figure 6-4. (a) Dimensionless pressure and (b) dimensionless gap for different values of Ne. S=0.01, $\hat{K}$ =0. The impermeable flexible web is assumed to move with velocity V to the right.

problems are mathematically equivalent as reported in Skotheim and Mahadevan (2005). For the pressure boundary conditions away from the minimum gap we assume $\hat{p}(-\hat{x}_a) = \hat{p}(\hat{x}_a) = 0$ where $\hat{x}_a$ =100. The $\hat{x}_a$ location is chosen so that further increasing its value will not alter significantly our numerical solution, in agreement with Yin and Kumar (2005). In Fig. 6.4 the pressure profiles and the gap profiles are shown for different Ne and S=0.01. The obtained pressure profile in Fig. 6.4a for Ne=0 (rigid web) attains an antisymmetric form while the formed gap is symmetric around the minimum separation point, as shown in Fig. 6.4b. By increasing web elasticity Ne, in Fig. 6.4b (i.e. making the

105

web more compliant) the gap is increasing and notably loses its symmetric form. This suggests that the web surface in contact with the fluid is forced away from the cylinder as it approaches it and tries to come closer as it moves downstream. As the gap increases due to increasing *Ne*, the pressure profile in Fig. 6.4a also loses its anti-symmetric form, with the difference between the magnitudes of the upstream maximum and downstream minimum increasing as *Ne* increases. The absolute values of the maximum/minimum pressures also decrease with increasing *Ne*.
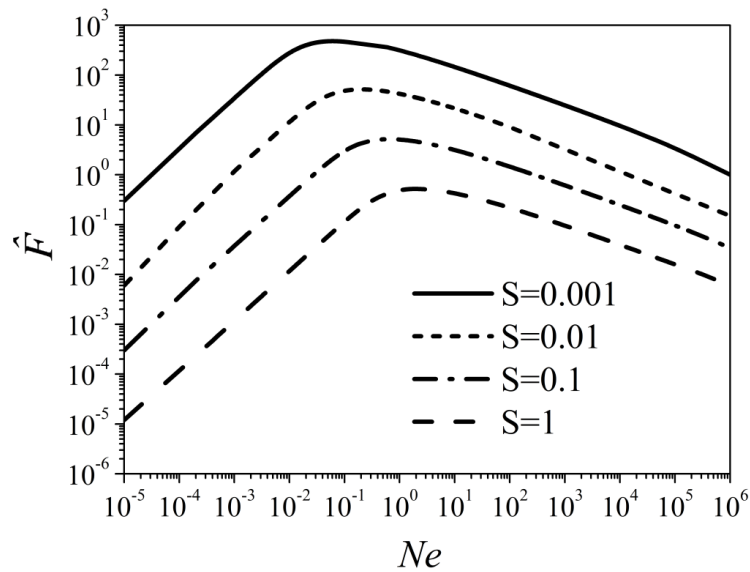
Figure 6-5. Dimensionless lift force per unit width $\hat{F}$ as a function of *Ne* for different *S* values for a non-permeable web ($\hat{K} = 0$).

The asymmetric pressure profiles in Fig. 6.4a resemble those of an inclined slider bearing configuration which is known to generate a lift force (Skotheim and Mahadevan 2004; Skotheim and Mahadevan 2005; Yin and Kumar 2005). The dimensionless lift force $\hat{F}$ per unit width in dimensionless form can be defined as

$$\hat{F} = \int_{-x_a}^{x_a} \hat{p} d\hat{x} \tag{6.20}$$

Plotting the lift force as a function of *Ne* shown in Fig. 6.5 indicates that for each cylinder/web separation (expressed by the dimensionless minimum distance *S*) the lift force increases as *Ne* increases, obtains a maximum value and then decreases for higher *Ne*. According to Skotheim and Mahadevan (2005) this maximum value may be viewed as the result of competition between symmetric gap breaking, which is dominant for low *Ne* values, and pressure decrease which is dominant for high *Ne* values. By increasing the

106

value of the dimensionless gap S the fluid has more space to flow which results in a decrease of the maximum lift force and a displacement of the location of the maximum towards higher Ne numbers. For instance, for $S=0.001$ we observe $F_{max}=479$ at $Ne=0.06$ whereas for $S=1$ the maximum lift force attains the value of $F_{max}=0.51$ at $Ne=1.5$.

6.3.2 Rigid and Permeable Web

In this section we restrict our interest to another limiting case, namely that of a rigid ($Ne=0$) permeable web (see Fig. 6.1). As in the previous section we set $\hat{p}(-100)=\hat{p}(100)=0$ and assume $S=0.01$. The calculated pressure profiles are shown in Fig. 6.6 for different dimensionless $\hat{K}$ values. It is evident that for increasing $\hat{K}$ the maximum/minimum pressure magnitudes decrease. The anti-symmetric shape of the pressure profile is not affected by variations of web permeability. Due to the symmetry of the pressure profile, no net lift force is computed here. Since this is a permeable web, it is of interest to predict the fluid penetration profile. Representative profiles are shown in Fig. 6.7, for various $\hat{K}$. The shape of the profiles is observed to be symmetric around $\hat{x}=0$ at which location the maximum penetration depth occurs. This is predicted to decay close to zero far upstream and downstream. This behavior is a direct result of the symmetric pressure profile (Fig. 6.6). This suggests the significant conclusion that although the rigid web is permeable, the final penetration depth $\hat{L}_f$ (where we assume that $\hat{L}_f=\hat{L}(\hat{x}=100)$) is zero.
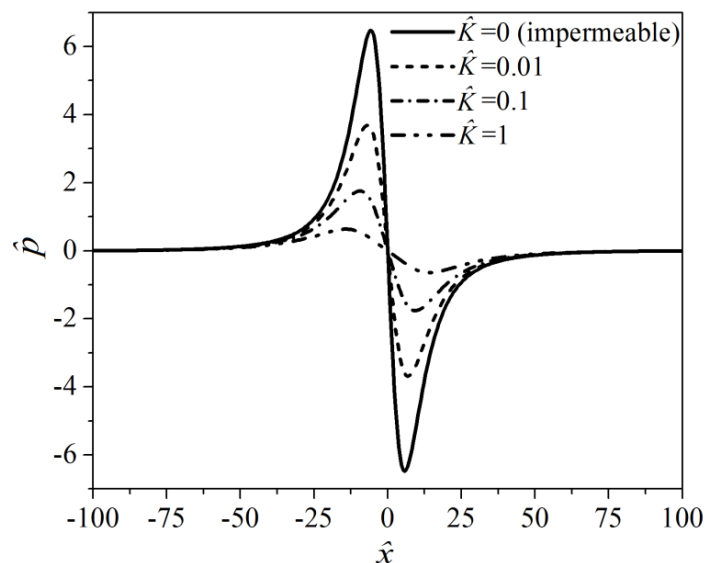
Figure 6-6: Dimensionless pressure for a permeable web with varying $\hat{K}$. $Ne=0$ (rigid web) and $S=0.01$.
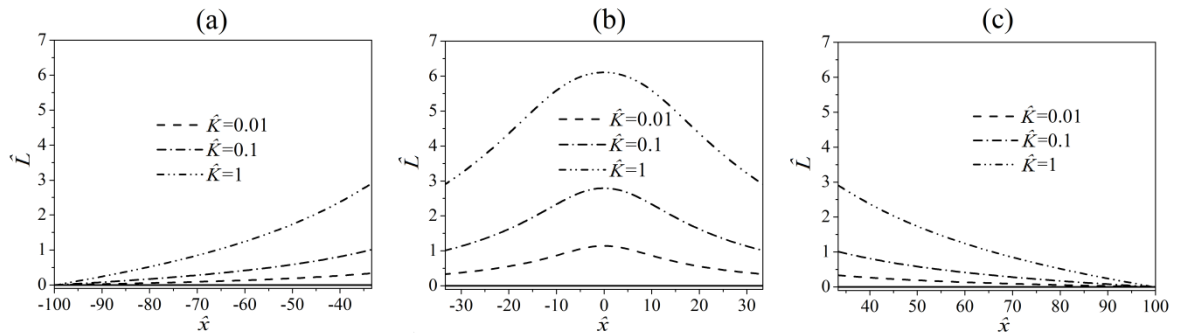
Figure 6-7: Penetration depth profiles of a permeable and rigid (*Ne*=0) web moving to the right for different $\hat{K}$ values with *S*=0.01. For clarity, results are shown for three equidistant regions in the *x*-direction for the range (a) $-100 \le \hat{x} \le -33.3$, (b) $-33.3 < \hat{x} < 33.3$ and (c) $33.3 \le \hat{x} \le 100$.

In Fig. 6.8a we present results regarding the gap flow rate profiles, based on Eq. 6.14, for different $\hat{K}$ values of the web. For $\hat{K}=0$ the gap flow rate is constant. By increasing $\hat{K}$ the profiles indicate that flow rate within the gap decreases, reflecting the fact that some fluid has penetrated into the substrate. Downstream from the minimum gap, the process is reversed; fluid exits the porous web and re-enters the main fluid zone. This process is amplified as $\hat{K}$ increases. It is also interesting to examine how the final fluid
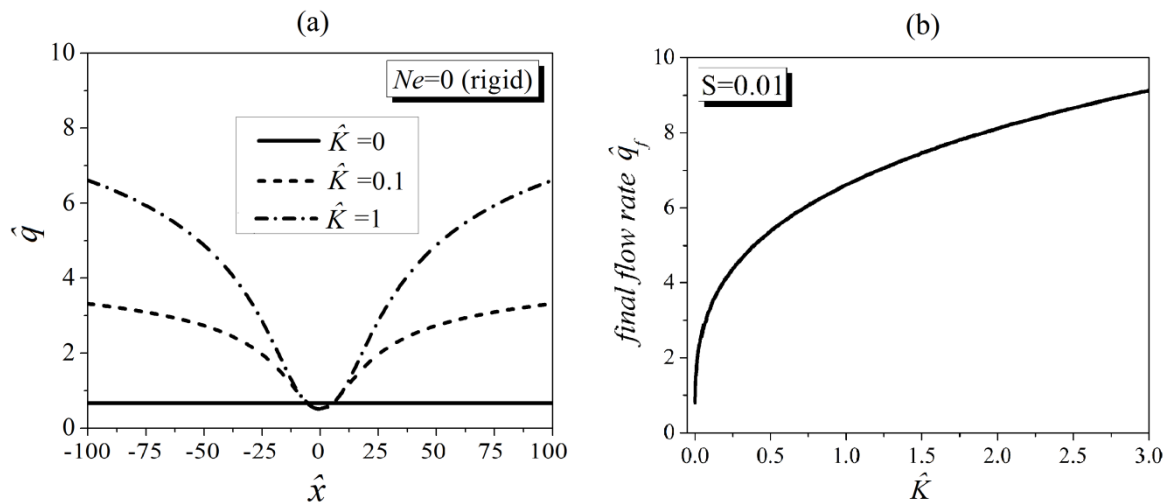
Figure 6-8: (a) Dimensionless gap flow rate profiles for a rigid (*Ne*=0) permeable web for different $\hat{K}$ values with *S*=0.01 and (b) final flow rate $\hat{q}_f$ through the gap showing the flow enhancement effect with increasing $\hat{K}$ for *S*=0.01.

flow rate $\hat{q}_f$ (where we assume that $\hat{q}_f = \hat{q}(\hat{x}=100)$) through the gap behaves and we plot it as a function of $\hat{K}$ as shown in Fig. 6.8b. The result appears to be counterintuitive. We

108

observe that for increasing $\hat{K}$ the amount of fluid entrained by the moving web increases, even for relatively low $\hat{K}$. The above described higher outflow behavior is in accordance with observations by Middleman (1995) for pressure driven flow in a leaky (permeable) tube, where it is stated: "...that for a given pressure gradient a leaky tube will exhibit a higher outflow than an impermeable tube".

6.3.3 Flexible and Permeable Web

The current section presents results for the combined effect of permeability and deformability on pressure build up and fluid infiltration in a web, which are now affected by both $\hat{K}$ and Ne. Representative pressure and gap profiles are shown in Fig. 6.9 for a $0{\leq}Ne{\leq}100$, with $\hat{K}=0.1$ (Fig. 6.9a and 6.9b) and $\hat{K}=10$ (Fig. 6.9c and 6.9d). The results indicate that either by increasing *Ne* (for a specific $\hat{K}$) or $\hat{K}$ (for a specific *Ne*) the magnitude of the pressure maximum/minimum has the tendency to decrease. A similar behavior is observed for the gap profiles shown in Fig. 6.9b and 6.9d. It is clear that the
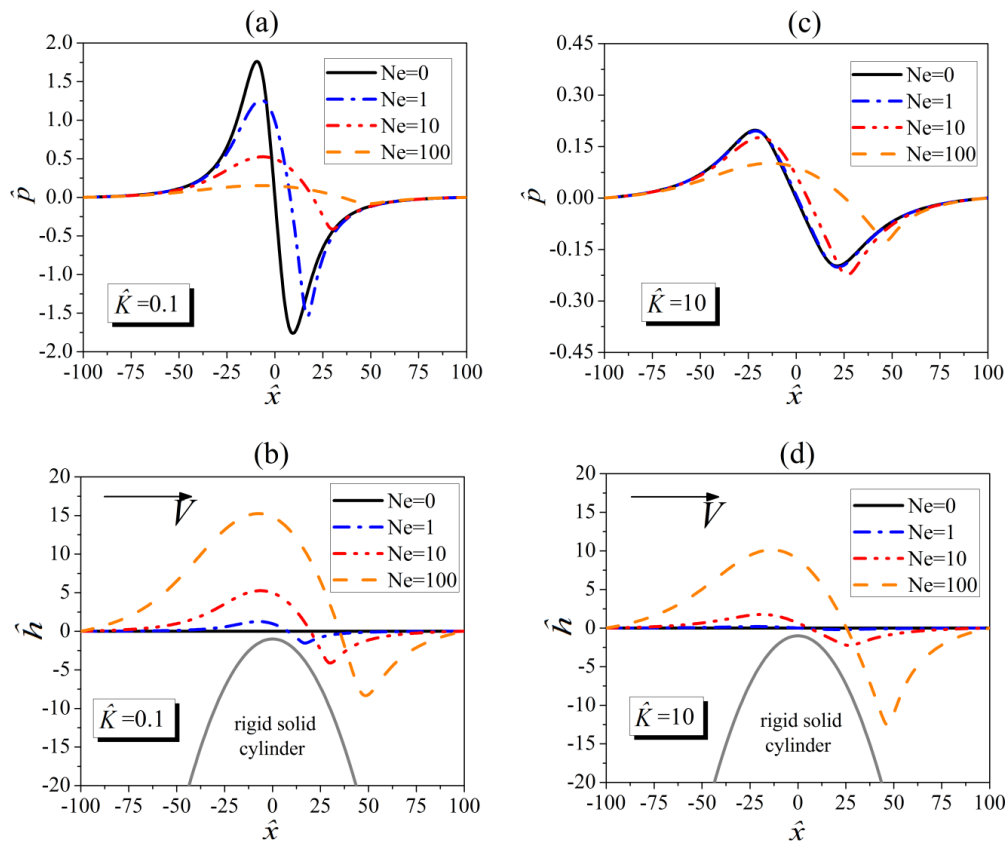
Figure 6-9: (a) Pressure and (b) gap profiles for different *Ne* values with $\hat{K}=0.1$. (c) Pressure and (d) gap profiles for different *Ne* values for $\hat{K}=0.1$. Results shown for *S*=0.01. *Ne*=0 corresponds to a rigid web. *V* denotes the web moving speed.

109

more compliant the web, the larger and more asymmetric is the gap forming between it and the cylinder.

It is meaningful to also investigate how the lift force per unit width $\hat{F}$ (Eq. 6.20) behaves. The results are shown in Fig. 6.10 for S=0.01, where for comparison we have added the lift force results for K=0 of Section 6.3.1. For low Ne, a web with $\hat{K}=0$ will develop the highest lift force, which decreases as $\hat{K}$ is increasing as a result of the pressure decrease. Reduction of the maximum lift force is also evident, for increasing $\hat{K}$, which is also shown to be shifted towards higher Ne values as compared to $\hat{K}=0$. For high Ne values the curves collapse to a single one which suggests that the lift force is affected only by the web deformability.
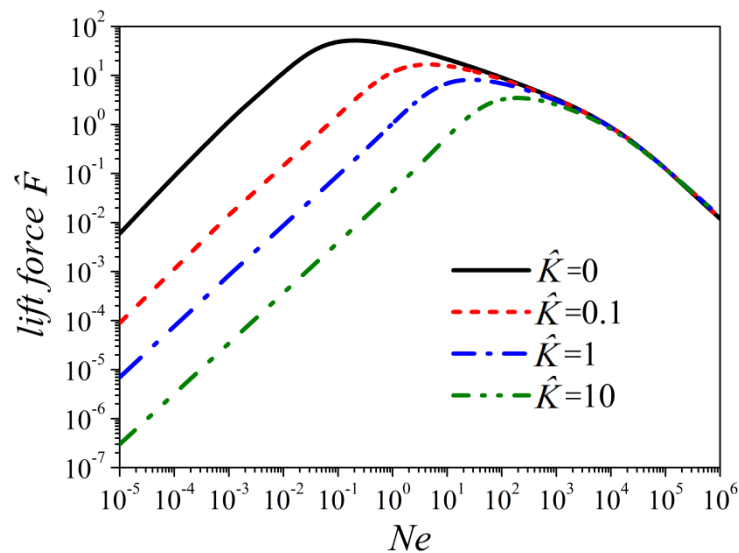
Figure 6-10: Dimensionless lift force per unit width as a function of Ne for different $\hat{K}$ values. S=0.01.

In Fig. 6.11a we plot the gap flow rate profiles for a deformable web with $\hat{K}=0.1$. Also shown is the profile for Ne=0 which is symmetric around $\hat{x}=0$. Increasing Ne, increases the asymmetry of the profiles, with the minimum becoming progressively shallower as Ne increases. We next turn our interest on how $\hat{q}_f$ behaves with $\hat{K}$ and Ne and we plot this in Fig. 6.11b. At very low and very high Ne there are two asymptotic regions, suggesting that for a "almost" rigid or very deformable web, $\hat{q}_f$ is independent of Ne. For $\hat{K}=0$ the two plateaus appear to have an almost linear connection fully in agreement with results of Yin
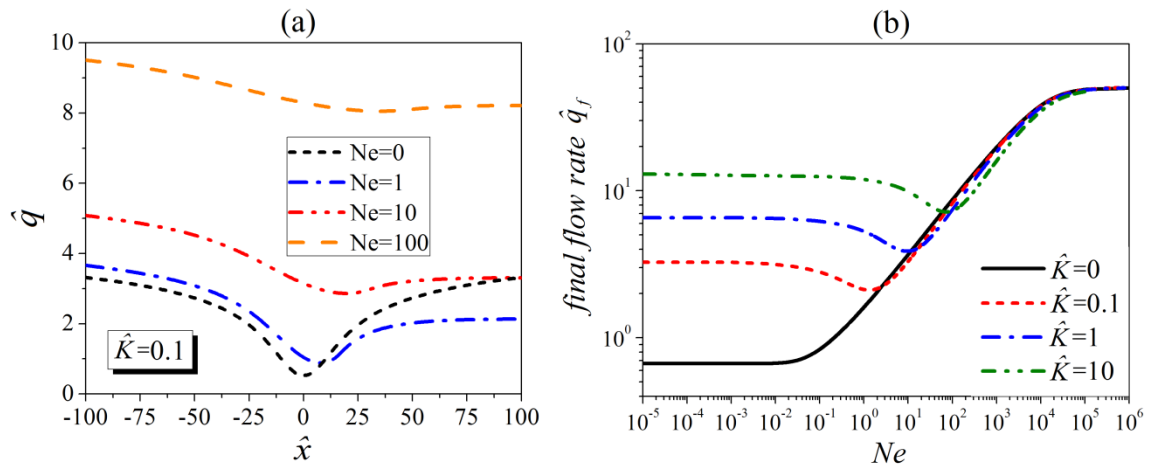
Figure 6-11: Dimensionless gap flow rate per unit width $\hat{q}$ profiles of a permeable web ($\hat{K} = 0.1$) for different *Ne* values in (a) and dimensionless final gap flow rate $\hat{q}_f$ as a function of *Ne* for different $\hat{K}$ values in (b). All cases for *S*=0.01.
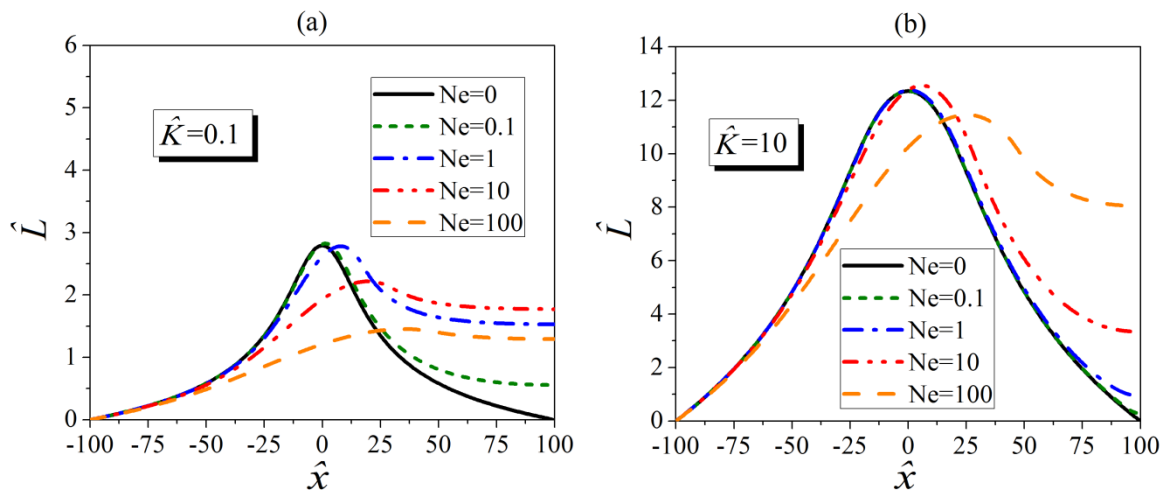
Figure 6-12: Penetration depth profiles for different *Ne* for a web with (a) $\hat{K} = 0.1$ and (b) $\hat{K} = 10$. Both cases are for *S*=0.01. Note that *Ne*=0 is for a rigid web which gives $\hat{L}_f = 0$ due to the symmetric gap. The web moves to the right.

and Kumar (2005) for a flexible impermeable wall. However, when the web is permeable the transition between the two asymptotes becomes non-linear, with $\hat{q}_f$ dropping to a minimum and then increasing to the high *Ne* asymptote. This is a direct consequence of the amount of fluid penetrating the web, as discussed in the following section.
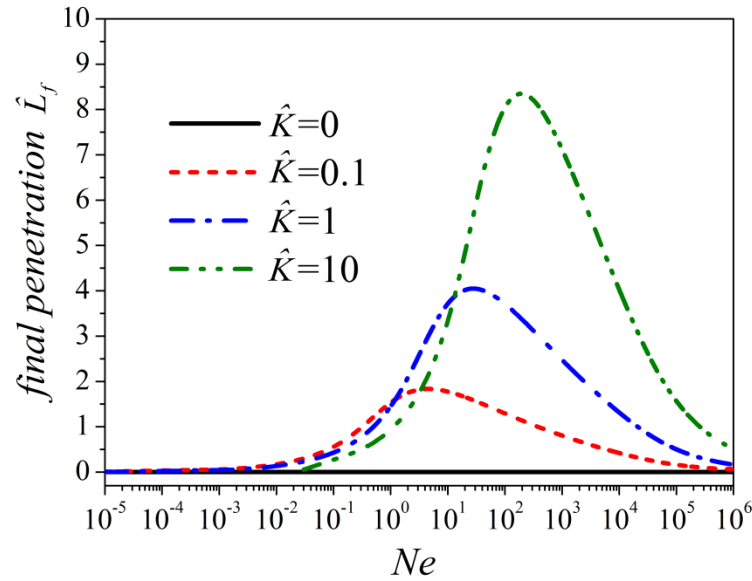
Figure 6-13: Dimensionless final penetration depth $\hat{L}_f$ as a function of Ne for different $\hat{K}$ values. S=0.01.

In Fig. 6.12a the penetration depth profiles for $\hat{K} = 0.1$ are shown. In contrast to a rigid web (Ne=0) of zero net fluid penetration, in a deformable there will be a final, residual, non-zero liquid penetration $\hat{L}_f$. Similar trends are shown in Fig. 6.12b when we increase the permeability to $\hat{K} = 10$. The combined effect of $\hat{K}$ and Ne on the final penetration depth $\hat{L}_f$ is shown in Fig. 6.13. The shape of the curves indicates that a very rigid or a very deformable permeable web will be infiltrated by the fluid only to a small extent – which is largely unaffected by variations in $\hat{K}$. On the other hand, for intermediate web deformability, variations in $\hat{K}$ cause a large effect on $\hat{L}_f$ which lead to a maximum final penetration depth the magnitude of which is susceptible to Ne and $\hat{K}$ variations. The presence of this maximum may explain the existence of the minimum in the final flow rate shown in Fig. 6.12 under specific Ne and $\hat{K}$ conditions.

6.4   Concluding Remarks

In the present work we utilize a modified approach of the classical lubrication equation to model the flow between a thin compressible flexible permeable web that moves in close proximity over a rigid solid stationary cylinder. We assume that the web deformation is locally proportional to the developed pressure in the gap between the web and the cylinder surface. The fluid penetration into the web is determined by Darcy's law.

Our results indicate that in the presence of web deformability, the web/fluid interface has the tendency to move away from the cylinder surface as it approaches it and tries to come closer as it leaves. We elucidate that this pushing from and pulling towards the cylinder behavior breaks the symmetry of the gap and results in a final fluid penetration which is not possible when the web behaves as completely rigid and permeable. Under specific deformability and permeability conditions of the medium the final amount of fluid that infiltrates is maximized. This may aid into optimization of relevant coating/printing processes as well as in the pultrusion of composites, where the fluid penetration depth essentially defines the final product properties.

6.5   References

Ascanio G., Carreau P.J., Brito-de la Fuente, E., Tanguy, P.A.: Forward deformable roll coating at high speed with Newtonian fluids. Chem. Eng. Res. Des. 82, 390-397 (2004)

Ascanio, G., Ruiz, G.: Measurement of pressure distribution in a deformable nip of counter-rotating rolls. Meas. Sci. Technol. 17, 2430-2436 (2006)

Bates, P.J., Kendall, J., Taylor, D., Cunningham, M.: Pressure build-up during melt impregnation. Compos. Sci. Technol. 62, 379-384 (2002)

Bates, P.J., Zou, X.P.: Polymer melt impregnation of glass roving. Int. Polym. Proc. 27, 376-386 (2002)

Bear, J.: Dynamics of Fluids in Porous Media. Courier Dover Publications, New York (1988)

Benkreira, H., Edwards, M.F., Wilkinson, W.L.: A semi-empirical model of the forward roll coating flow of Newtonian fluids. Chem. Eng. Sci. 36, 423-427 (1981)

Benkreira, H., Edwards, M.F., Wilkinson, W.L.: Roll coating of purely viscous liquids. Chem. Eng. Sci. 36, 429-434 (1981)

Benkreira, H., Patel R.: Direct gravure roll coating. Chem. Eng. Sci. 48, 2329-2335 (1993)

Bijsterbosch, H., Gaymans, R.J.: Impregnation of glass rovings with a polyamide melt. Part 1: Impregnation bath. Compos. Part A-Appl. S. 4, 85-92 (1993)

Carvalho, M.S., Scriven, L.E.: Deformable roll coating flows: steady state and linear perturbation analysis. J. Fluid Mech. 339, 143-172 (1997)

Carvalho, M.S., Scriven, L.E.: Flows in forward deformable roll coating gaps: comparison between spring and plane-strain models or roll cover. J. Comput. Phys. 138, 449-479 (1997)

Carvalho, M.S.: Effect of thickness and viscoelastic properties of roll cover on deformable roll coating flows. Chem. Eng. Sci. 58, 4323-4333 (2003)

Chen, K.S.A., Scriven, L.E.: Liquid penetration into a deformable porous substrate. Tappi J. 73, 151-161 (1990)

Cohu, O., Magnin, A.: Forward roll coating of Newtonian fluids with deformable rolls: an experimental investigation. Chem. Eng. Sci. 52, 1339-1347 (1997)

Coyle, D.J.: Forward roll coating with deformable rolls: a simple one dimensional elastohydrodynamic model. Chem. Eng. Sci. 43, 2673-2684 (1988)

Coyle, D.J., Macosko, C.W., Scriven, L.E.: The fluid dynamics of reverse roll coating. AIChE J. 36, 161-174 (1990)

Devisetti, S.K., Bousfield, D.W.: Fluid absorption during forward roll coating on porous webs. Chem. Eng. Sci. 65, 3528-3537 (2010)

Ding, X., Fuller, T.F., Harris, T.A.L.: Predicting fluid penetration during slot die coating onto porous substrates. Chem. Eng. Sci. 99, 67-75 (2013)

Ding, X., Ebin, J.P., Harris, T.A.L., Li, Z., Fuller, T.F.: Analytical models for predicting penetration depth during slot die coating onto porous media. AIChE J. 60, 4241-4252 (2014)

Farboodmanesh, S., Chen, J., Mead, J.L., White, K.D., Yesilalan, H.E., Laoulache, R., Warner, S.B.: Effect of coating thickness and penetration on shear behavior of coated fabrics. J. Elastom. Plast. 37, 197-227 (2005)

Gaymans, R.J., Wevers, E.: Impregnation of a glass fibre roving with a polypropylene melt in a pin assisted process. Compos. Part A-Appl. S. 29, 663-670 (1998)

Gibson, A.G., Månson, J.A.: Impregnation technology for thermoplastic matrix composites. Compos. Part A-Appl. S. 3, 223-233 (1992)

Gostling, M.J., Savage, M.D., Young, A.E., Gaskell, P.H.: A model for deformable roll coating with negative gaps and incompressible compliant layers. J. Fluid Mech. 489, 155-184 (2003)

Hayes, R.E., Bertrand, F.H., Tanguy P.A.: Modeling of fluid/paper interaction in the application nip of a film coater. Transport Porous Med. 40, 55-72 (2000)

Hewson, R.W., Kapur, N., Gaskell, P.H.: A two-scale model for discrete cell gravure roll coating. Chem. Eng. Sci. 66, 3666-3674 (2011)

Jones, M.B., Fulford, G.R., Please, C.P., McElwain, D.L.S., Collins M.J.: Elastohydrodynamics of the Eyelid Wiper. Bull. Math. Biol. 70, 323-343 (2008)

Kapur, N.: A parametric study of direct gravure coating. Chem. Eng. Sci. 58, 2875-2882 (2003)

Leal, L.: Advanced Transport Phenomena: Fluid Mechanics and Convective Transport Properties. Cambridge University Press, New York (2007)

Lécuyer, H.A., Mmbaga, J.P., Hayes, R.E., Bertrand, F.H., Tanguy, P.A.: Modeling of forward roll coating flows with a deformable roll: Application to non-Newtonian industrial coating formulations. Comput. Chem. Eng. 33, 1427-1437 (2009)

Lee, S., Na, Y.: Effect of roll patterns on the ink transfer in R2R printing process. Int. J. Precis. Eng. Man. 10, 123-130 (2009)

Madasu, S., Cairncross, R.A.: Effect of substrate flexibility on dynamic wetting: A finite element model. Comput. Methods Appl. Mech. Engrg. 192, 2671-2702 (2003)

Madasu, S.: Effect of soluble surfactants on dynamic wetting of flexible substrates: A finite element study. Phys. Fluids 21, 122103 (2009)

Matilainen, K., Hämäläinen, T., Savolainen, A., Sipiläinen-Malm, T., Peltonen, J., Erho, T., Smolander, M.: Performance and penetration of laccase and ABST inks on various printing substrates. Colloids Surf. B 90, 119-128 (2012)

Middleman, S.: Modeling Axisymmetric Flows: Dynamics of Films, Jets and Drops. San Diego (1995)

Nam, J., Carvalho, M.S.: Flow in tensioned-web-over-slot die coating: Effect of die lip design. Chem. Eng. Sci. 65, 3957-3971 (2010)

Polychronopoulos, N.D., Papathanasiou T.D.: Pin-assisted resin infiltration of porous substrates. Compos. Part A-Appl. S. 71, 126-135 (2015)

Ramon, G.Z., Huppert, H.E., Lister, J.R., Stone, H.A.: On the hydrodynamic interaction between a particle and a permeable surface. Phys. Fluids 25, 073103 (2013)

Romero, O.J., Suszynski, W.J., Scriven, L.E., Carvalho, M.S: Low-flow limit in slot coating of dilute solutions of high molecular weight polymer. J. Non-Newt. Fluid Mech. 118, 137-156 (2004)

Sandström, A., Dam, H.F., Krebs, F.C., Edman, L.: Ambient fabrication of flexible and large-area organic light-emitting devices using slot-die coating. Nat. Commun. 3, 1-5 (2012)

Shampine, L., Kierzenka, J., Reichelt, M.: Solving Boundary Values Problems for ordinary Differential Equations in MATLAB with bvp4C. The MathWorks Inc. (http://www.mathworks.com/bvp_tutorial) (2000)

Skotheim, J.M., Mahadevan, L.: Soft lubrication. Phys. Rev. Lett. 92, 245509 (2004)

115

Skotheim, J.M., Mahadevan, L.: Soft lubrication: The elastohydrodynamics of nonconforming and conforming contacts. Phys. Fluids 17, 092101 (2005)

Sullivan, T., Middleman, S., Keunings, R.: Use of a finite element method to interpret rheological effects in blade coating. AIChE J. 33, 2047-2056 (1987)

Yesilalan, H.E., Warner, S.B., Laoulache, R.: Penetration of blade-applied viscous coatings into yarns in a woven fabric. Text. Res. J. 80, 1930-1941 (2010)

Yin, X., Kumar, S.: Lubrication flow between a cavity and a flexible wall. Phys. Fluids 17, 063101 (2005)

Yin, X., Kumar, S.: Two-dimensional simulations of flow near a cavity and a flexible solid boundary. Phys. Fluids 18, 063103 (2006)

Chapter 7

Conclusions and Recommendations for Future Work

7.1   Conclusions

Conclusion 1: Investigation of the calendering process with a fully 3D numerical framework shows that a film/sheet becomes wider (spreads) in the lateral direction due to pressure build-up in this direction. The amount of spreading increases due to either increase of the material's thickness at the entrance of the cylinders or due to increase in the feeding speed. The material is forced to the sides through a spiraling motion involving a remarkable flow redistribution.

Conclusion 2: Investigation of extrudate swell in film casting shows that the maximum swell of a viscoelastic polymer decreases rapidly as the drawing speed of the chill roll increases.

Conclusion 3: The polymer penetration depth in the pin-assisted pultusion process is found to be affected by a large number of process and material parameters. A scaling analysis based on the possible flow directions the fluid may follow, reveals that the process and material parameters may be lumped together into a single dimensionless number which is related to the penetration depth via power-law type dependence. When this number increases the fluid prefers to travel through the formed gap between the composite porous substrate rather than through the substrate, leading to decrease in the penetration depth.

Conclusion 4: A deformable permeable web moving past a solid rigid stationary cylinder is shown to pull away from the cylinder as it approaches it and pushes towards it as it leaves. This behavior is affected by both web deformability and permeability. The analysis indicates that the amount of fluid penetrating the web is maximized under specific deformability and permeability conditions.

7.2   Contributions to Knowledge

The following constitute the novel contributions to knowledge made by the present thesis:

Contribution 1: <u>The first fully 3D numerical study for calendering including spreading.</u> The analysis gives how: (i) the pressure build-up, (ii) the amount of spreading and (iii) the sideways spiral motion of the material, are related. Simultaneous knowledge of these three distinct features may lead to improved engineering designs and possible reduction of defects of the edges of the film or sheet produced.

Contribution 2: <u>First numerical study of the film casting process that takes into account extrudate swell and the effect of drawing</u>. It is discussed that taking into account the velocity at the point of maximum swell, rather than the average velocity in the extrusion die will result in a more realistic definition of the drawing ratio (*DR*), which is frequently used in process characterization and control.

Contribution 3: <u>Described for the first time the complex fluid penetration dynamics in a porous substrate of the pin-assisted pultrusion based on a 2D approach and using a realistic model for flow within the porous medium</u>. We have shown, for the first time, how the achieved penetration depth scales with related process and material parameters. We have also shown that the polymer is conveyed via a complex two-dimensional flow, in which a drag flow caused by the moving substrate is resisted by a pressure gradient which develops in the narrow gap separating substrate and pin.

Contribution 4: <u>A novel fluid penetration model involving a new dimensionless number for the pin-assisted pultrusion is proposed.</u> The predictive power of the proposed model is reflected by the fact that it produces results which are in good overall agreement with earlier experimental works. This novel scaling allows for rational experimental design, estimation of the sensitivity of the achieved result on the various process/material parameters and, when calibrated for an actual production process, for rational process optimization.

Contribution 5: <u>For the first time the penetration depth into a deformable and permeable web moving past a cylinder was determined, using the lubrication approximation and</u>

118

Darcy's law. The results are important not only in pultrusion of composite tapes but also in the similar processes of roll coating and printing.

7.3   Recommendations for Future Work

The results from this research could be extended in the future into the following areas:

Recommendation 1: (i) Fully 3D calendering analysis including spreading and a melt bank with free surface. (ii) Study of roll reflection or roll crowning on lateral spreading.

Recommendation 2: (i) Numerical study of cast film extrusion involving extrudate swell in combination with necking (narrowing of the width) and edge-beading (thickening of the edges) and (ii) Study of the above in combination with heat transfer and the resulting orientation and crystallization.

Recommendation 3: Use of anisotropic permeability to investigate the fluid infiltration dynamics of a porous substrate in pin-assisted pultrusion. Taking into account the different flow resistances in various directions of the medium, will extend the proposed novel fluid penetration model of the process that may refine the control of architecture and thus the properties of the final pultruded product.

Recommendation 4: Investigate the fluid penetration dynamics in a deformable permeable composite web using different deformation models such as the elastic half space, thin shell approximation and viscoelastic fluid.

Appendices

Appendix A

Calendering: Lubrication Approximation and Sheet Spreading Validation

A.1   Lubrication Approximation

It may be assumed that the most important effect in the calendering process occur in the region of the minimal cylinder separation. In that region and extending to either side (in the $\pm x$ direction) by a distance of the order of x_f as shown in Fig. 2.1, the roll surfaces are nearly parallel if, as is usually the case, $H_o << R$. Then it is reasonable to assume that the flow is nearly parallel, so that

$$\frac{\partial}{\partial x} << \frac{\partial}{\partial y} \qquad \text{and} \qquad v << u \tag{A.1.1}$$

where u is the x velocity component and v the y velocity component. For a Newtonian fluid and under the above assumptions Eq. 2.2 and Eq. 2.3 become respectively

$$0 = -\frac{dp}{dx} + \frac{\partial \tau_{xy}}{\partial y} \tag{A.1.2a}$$

$$\frac{dp}{dy} = 0 \tag{A.1.2b}$$

$$\tau_{xy} = \mu \frac{\partial u}{\partial y} \tag{A.1.3}$$

where τ_{xy} is the shear stress at the cylinder surface. Substituting Eq. A.1.3 to Eq. A.1.2a we obtain

$$0 = -\frac{dp}{dx} + \mu \frac{\partial^2 u}{\partial y^2} \tag{A.1.4}$$

The process of transforming a problem from Eq. 2.2 to Eq. A.1.4, under the assumptions of Eq. A.1.1, is often referred to as *making the usual lubrication approximations* (the reference to lubrication approximation comes from the fact that lubrication problems themselves typically involve a geometry such that Eq. A.1.1 is valid).

Equation A.1.4 is easily integrated using the following boundary conditions at the cylinder surface and the centerline (with reference to Fig. 2.1 in Chapter 2) respectively

$$u = U_R \text{ on } y = H(x) \quad \text{and} \quad \frac{\partial u}{\partial y} = 0 \text{ on } y = 0 \tag{A.1.5}$$

121

to give

$$u = U_R + \frac{y^2 - H^2(x)}{2\mu}\frac{dp}{dx} \tag{A.1.6}$$

Using the conservation of mass for the x-direction

$$q_x = 2\int_0^{H(x)} u\,dy \tag{A.1.7}$$

where we substitute Eq. A.1.6, we obtain

$$\frac{dp}{dx} = \frac{3\mu}{H^2(x)}\left(U_R - \frac{q_x}{2H(x)}\right) \tag{A.1.8}$$

where $H(x)$ is the gap between the cylinder and the centerline, given by Eq. 2.8. However, introducing Eq. 2.8 into Eq. A.1.6 complicates the algebra. Since it is likely that we will confine the analysis to values of x such that $x<<R$, a good approximation to $H(x)$ is

$$H(x) = H_o\left(1 + \frac{x^2}{2H_o R}\right) \tag{A.1.9}$$

Introducing the dimensionless x′ given by Eq. 2.9 we have

$$\frac{H(x)}{H_o} = 1 + x' \tag{A.1.10}$$

If we assume that the sheet leaves the rolls with a thickness H_f (see Fig. 2.1) and a speed U_R we have

$$q_x = 2U_R H_f \Rightarrow \frac{H_f}{H_o} = \frac{q_x}{2URH_o} \tag{A.1.11}$$

Letting $x'=x'_f$ for $H(x)=H_f$ we have

$$\frac{H_f}{H_o} = \frac{q_x}{2URH_o} = 1 + x'^2_f \tag{A.1.12}$$

Substituting q_x with $(1+x'^2_f)2U_R H_o$ in Eq. A.1.8 and inserting the dimensionless pressure given in Eq. 2.9 for $n=1$, upon rearrangement we obtain

$$\frac{dp'}{dx'} = \sqrt{\frac{18R}{H_o}}\frac{x'^2 - x'^2_f}{(1+x'^2)^2} \tag{A.1.13}$$

Equation A.1.13 give a zero pressure gradient at $x' = \pm x'_f$ which upon integration with $p'(x'=x'_f)=0$ the downstream pressure distribution is obtained. If we further assume that $p\rightarrow 0$ as $x'\rightarrow -\infty$ we get

$$x'_f = 0.475 \tag{A.1.14}$$

122

Upon substitution of Eq. A.1.14 in Eq. A.1.12 we obtain the maximum sheet thickness to minimum gap width ratio

$$\frac{H_f}{H_o} = 1.226 \tag{A.1.15}$$

For a shear-thinning fluid, Eq. A.1.3 takes the following form

$$\tau_{xy} = m \left| \frac{\partial u}{\partial y} \right|^{n-1} \frac{\partial u}{\partial y} \tag{A.1.16}$$

where the absolute value sign on the velocity gradient term (which is really $\sqrt{\frac{1}{2} II_D}$, see Eq. 2.6 in section 2.2) avoids the problem of taking a fractional root of a negative number.

From the Newtonian solution presented above we can see that we should anticipate two flow regions, a region where the pressure gradient is positive $x' < x'_f$ and a region where the pressure gradient is negative $x' > -x'_f$. Thus, integrating Eq. A.1.2a, using Eq. A.1.16, separately for each region we have

$$u = U_R \pm \frac{1+n}{n} \left(\pm \frac{1}{m} \frac{dp}{dx} \right)^{\frac{1}{n}} \left[y^{\frac{n}{1+n}} - H(x)^{\frac{n}{1+n}} \right] \tag{A.1.17}$$

Introducing either form of Eq. A.1.17 into the conservation of mass (Eq. A.1.7) and then solving for the pressure gradient, Eq. 2.10 (see Chapter 2) is obtained

$$\frac{dp'}{dx'} = -\left(\frac{2n+1}{n} \right)^n \sqrt{\frac{2R}{H_o}} \frac{\left(x'^2_f - x'^2 \right) \left| x'^2_f - x'^2 \right|^{n-1}}{\left(1 + x'^2 \right)^{2n+1}} \tag{A.1.18}$$

which upon integration we obtain the pressure profile in the machine direction.

A.2   Sheet Spreading Validation

Below a two-dimensional approach for the sheet spreading, similar to the work by Levine et al. (Ref. [26] in Section 2.5), is described, the results of which are compared to the 3D simulations. Making the usual lubrication assumptions previously discussed, we restrict the flow kinematics description in the x and z directions (see Fig. 2.1 in section 2.2). Noting that the velocity of the fluid in the z-direction is denoted as w and using flow rates instead of velocities, the continuity equation (Eq. 2.1) takes the following form

$$\frac{\partial q_x}{\partial x} + \frac{\partial q_z}{\partial z} = 0 \tag{A.2.1}$$

123

where

$$q_x = \int_0^{H(x)} u\,dy \qquad (A.2.2)$$

which is half the flow rate given by Eq. A.1.7 due to the problem symmetry we assume here, and q_z is given by

$$q_z = \int_0^{H(x)} w\,dy \qquad (A.2.3)$$

The equations of motion integrated across the half of the thickness yield

$$q_x = U_R H(x) - s\frac{\partial p}{\partial x} \qquad (A.2.4)$$

$$q_z = -s\frac{\partial p}{\partial z} \qquad (A.2.5)$$

where s is given by

$$s = \int_0^{H(x)} \int_y^{H(x)} \frac{t}{\eta}\,dt\,dy \qquad (A.2.6)$$

with t a dummy variable. Due to the double integration the variable s is independent of y and depends only on the fluid viscosity function $\eta(II_D)$ given by Eq. 2.6 where

$$\frac{1}{2}II_D = \left(\frac{\partial u}{\partial y}\right)^2 + \left(\frac{\partial w}{\partial y}\right)^2 \qquad (A.2.7)$$

By rearrangement of Eq. 2.6 and A.2.7 and using the velocity profiles u and w we obtain

$$\eta = m^{\frac{1}{n}} y^{\frac{n-1}{n}} |\nabla p|^{\frac{n-1}{n}} \qquad (A.2.8)$$

which replaced into Eq. A.2.6 provides an expression for the variable s as a function of the material rheology, the film thickness and the pressure field

$$s = \frac{n}{2n+1}\frac{H(x)^{\frac{2n+1}{n}}}{m^{\frac{1}{n}}}|\nabla p|^{\frac{1-n}{n}} \qquad (A.2.9)$$

In the downstream (machine) direction we set $p(x=x_f)=p(x=x_i)=0$. For the cross-machine direction, at the sheet spreading side (see Fig. 2.1) at $z=z(x)$ we set

$$\frac{dz(x)}{dx} = \frac{q_z}{q_x} \qquad (A.2.10)$$

124

This condition states that there must be no cross flow normal to the sheet side edge (i.e. **u·n**=0, where **n** unit vector normal to the side edge of the sheet), which is similar to Eq. 2.11 we used for the 3D computations.

Substituting Eq. A.2.4 and Eq. A.2.5 in Eq. A.2.1 and using Eq. 2.9 we render Eq. A.2.4 dimensionles

$$\sqrt{\frac{H_o}{2R}}\frac{dH'(x')}{dx'} - \nabla \cdot \left(s'\nabla p'\right) = 0 \qquad (A.2.11)$$

where the operator ∇ is now defined as

$$\nabla \equiv \begin{bmatrix} \sqrt{\dfrac{H_o}{2R}}\dfrac{\partial}{\partial x} \\ \dfrac{2H_o}{W_i}\dfrac{\partial}{\partial z} \end{bmatrix} \qquad (A.2.12)$$

and the parameter s' is given by

$$s'(p') = \frac{n}{2n+1}H'(x')^{\frac{2n+1}{n}}\left|\nabla p'\right|^{\frac{1-n}{n}} \qquad (A.2.13)$$

Solution of Eq. A.2.11 provides the pressure field across the spreading sheet. The dimensionless boundary condition (Eq. A.2.10) at the spreading side takes the form

$$\frac{dz'}{dx'} = \frac{\sqrt{R/2H_o}}{W_i/2H_o}\frac{q_x'}{q_z'} \qquad (A.2.14)$$

where $q_x'=q_x/U_R H_o$ and $q_z'=q_z/U_R H_o$.
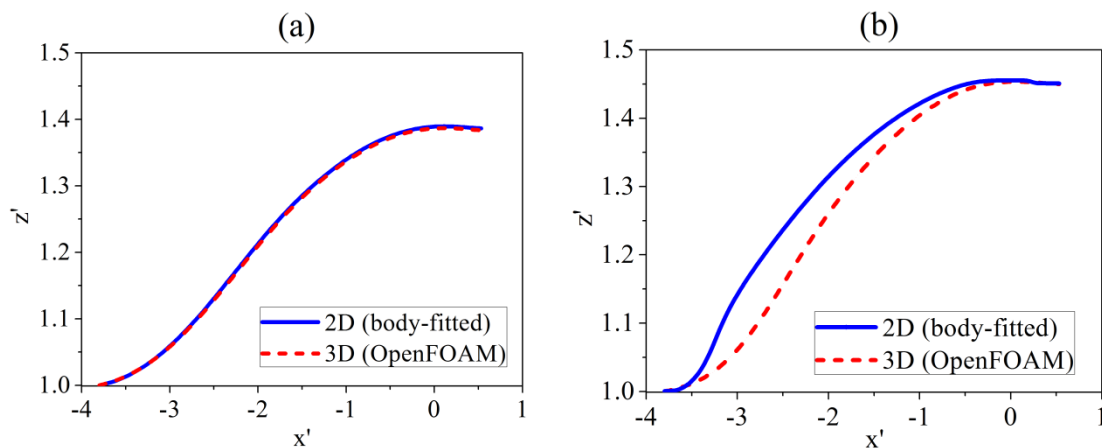
Figure-A.2.1: Half-width sheet spreading results for (a) a Newtonian fluid with μ=5000 Pa·s (2D: 3600 cells, 3D: 8×10^5 cells) and (b) for a shear-thinning fluid with n=0.35 and m=50000 Pa·s$^{0.35}$ (2D: 8100 cells, 3D: 2.4×10^6 cells). Typical process parameters used: V=0.1 m/s, R=0.125 m, H_o=5×10^{-4} m and W_i=0.1 m.

Equation A.2.11 with the dimensionless associated boundary conditions expressed via Eq. A.2.14 (for cross-machine direction) and $p'(x'=x'_f)= p'(x'=x'_i)$=0 (for the machine

125

direction), is solved numerically employing a body-fitted coordinates method with finite differences scheme [communication from Dr. T.D. Papathanasiou].
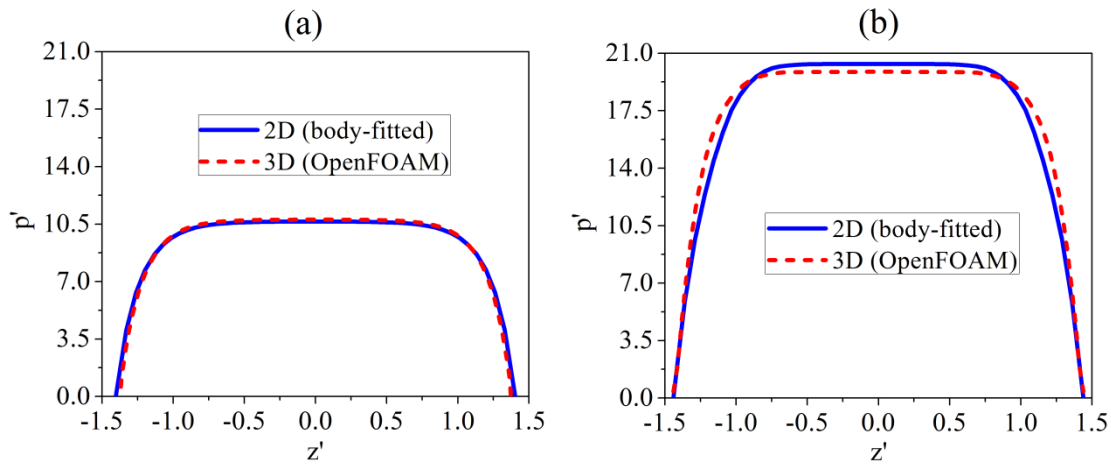

Figure-A.2.2: Pressure distribution in the z-direction at $x'=-0.475$ for (a) a Newtonian fluid with μ=5000 Pa·s (2D: 3600 cells, 3D: 8×10^5 cells) and (b) for a shear-thinning fluid with n=0.35 and m=50000 Pa·s$^{0.35}$ (2D: 8100 cells, 3D: 2.4×10^6 cells). Typical process parameters used: V=0.1 m/s, R=0.125 m, H_o=5×10^{-4} m and W_i=0.1 m.

Number of cells	z'_{max} (Newtonian)
8×10^3	1.363
8×10^4	1.387
8×10^5	1.393

Table-A.2.1: Mesh sensitivity analysis for the Newtonian case of the 3D computations based on the maximum half-width.

Number of cells	z'_{max} (n=0.35, m=50000 Pa·s$^{0.35}$)
2.4×10^3	1.404
2.4×10^4	1.433
2.4×10^6	1.44

Table-A.2.2: Mesh sensitivity analysis for the shear-thinning fluid of the 3D computations based on the maximum half-width.

The comparison between the 2D sheet spreading with the 3D simulations, for a half-width sheet corresponding to the Newtonian case, is shown in Fig. A.2.1a. For a shear-thinning fluid the spreading is shown in Fig. A.2.1b. For both cases the 3D results compare well with the spreading predictions of the 2D case. In Table A.2.1 mesh

126

sensitivity results of the 3D computations are shown for the Newtonian and in Table A.2.2 for the shear-thinning case, based on the maximum half-width $z'_{max}=z'(x'=x'_f)$ of the sheet. In Fig. A.2.2a the pressure distribution in the z-direction at $x'=-0.475$ for the Newtonian case is shown and in Fig. A.2.2b for the shear thinning material. Both cases are for the convergent mesh sizes and the results are in good agreement.

Appendix B

General Validation of OpenFOAM Porous Solver

Below we present an approach to assess the behavior of the OpenFOAM porous solver used in Chapters 4 and 5 for the pin-assisted pultrusion process. We focus on a typical flow problem frequently encountered in modeling dual scale polymer composites: the flow in periodic fiber tows (bundles). The main objective is to estimate the effective (overall) permeability of the system. The results of the solver are compared to the results of a semi-analytical method which is based on the lubrication approximation. Following the work of Phelan and Wise[1], we assume a square unit cell of half-lengths L_x and L_y in x
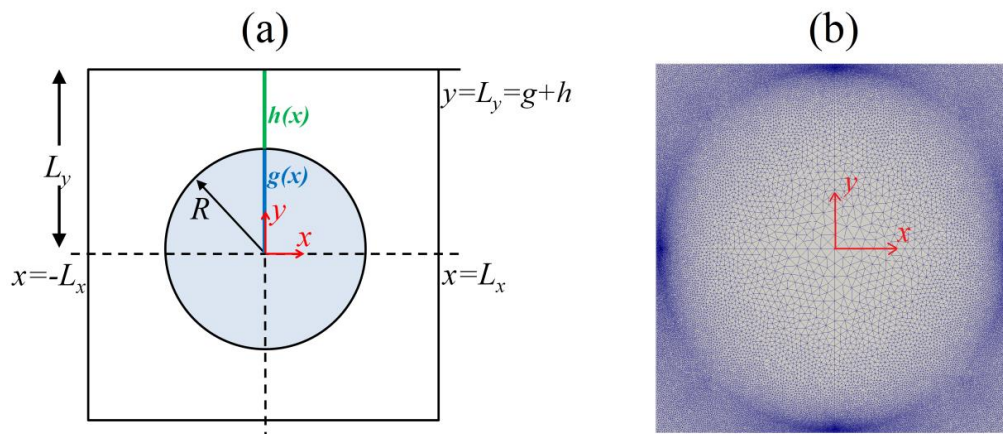

Figure-B.1: (a) Schematic representation of the problem two-dimensional geometry. The square corresponds to the unit cell and the circle of radius R to the cross-section of the fiber bundle (figure not to scale). (b) A typical computational mesh used with 7×10^4 cells.

and y directions respectively, inside of which there exists a fiber tow with circular cross section of radius R and specific tow permeability denoted K_{tow} as shown in Fig. B.1a. The volume fraction of the tow in the unit cell is given by

$$\phi = 1 - \varepsilon = \frac{\pi}{4}\frac{R^2}{L_x L_y} \tag{B.1}$$

where ε corresponds to the porosity of the system. We note that K_{tow} is assumed to be the transverse permeability (i.e. permeability in the y-direction) of the tow.

[1]Phelan F.R., Wise G., Composites Part A, 27A, 25-34 (1996)

The governing equations of the OpenFOAM porous solver, including the continuity equation, in compact form are written as

$$\nabla p = -\alpha \frac{\mu}{\mathbf{K}} \mathbf{U} + \mu \nabla^2 \mathbf{U} \tag{B.2}$$

$$\nabla \cdot \mathbf{U} = 0 \tag{B.3}$$

where $\mathbf{U}$ is the velocity in the porous region or outside this region, μ the viscosity, $\mathbf{K}$ is the permeability tensor given by

$$\mathbf{K} = \begin{bmatrix} K_{xx} & K_{xy} & K_{xz} \\ K_{yx} & K_{yy} & K_{yz} \\ K_{zx} & K_{zy} & K_{zz} \end{bmatrix} \tag{B.4}$$

and α is a quantity equal to 0 for open media (Stokes equation) and equal to 1 for porous media (Brinkman/extended Darcy equation). For the two-dimensional geometry shown in Fig. B.1., with $K_{yy}=K_{tow}$ and the rest components of the permeability tensor to be zero (since we have assumed only transverse permeability), Eqs. B.2 and B.3 reduce to

$$\frac{\partial p}{\partial x} = -a \frac{\mu}{K_{tow}} u + \mu \left(\frac{\partial^2 u}{\partial x^2} + \frac{\partial^2 u}{\partial y^2} \right) \tag{B.5a}$$

$$\frac{\partial p}{\partial y} = -a \frac{\mu}{K_{tow}} v + \mu \left(\frac{\partial^2 v}{\partial x^2} + \frac{\partial^2 v}{\partial y^2} \right) \tag{B.5b}$$

$$\frac{\partial u}{\partial x} + \frac{\partial v}{\partial y} = 0 \tag{B.6}$$

A typical 2D computational mesh where the above equations are solved, simultaneously for $\alpha=0$ and $\alpha=1$, is shown in Fig. B.1b. We use an unstructured mesh with triangular cells and employ necessary mesh refinement near the tow/fluid interface as well as in the tight gaps between the unit cell and the tow, so that the maximum aspect ratio of each cell will not exceed the value of 10. A typical velocity field as obtained by the computation is shown in Fig. B.2a and in Fig. B.2b a typical pressure profile is shown. For the computations we have chosen: $\phi=0.75$, $\mu=100$ Pa·s, $K_{tow}=10^{-8}$ m^2, $L_x=L_y=0.01$ m, $R=9.772\times10^{-3}$ m and an arbitrary pressure drop (since we assume pressure-driven flow in the x-direction) of $\Delta p=100$ kPa.
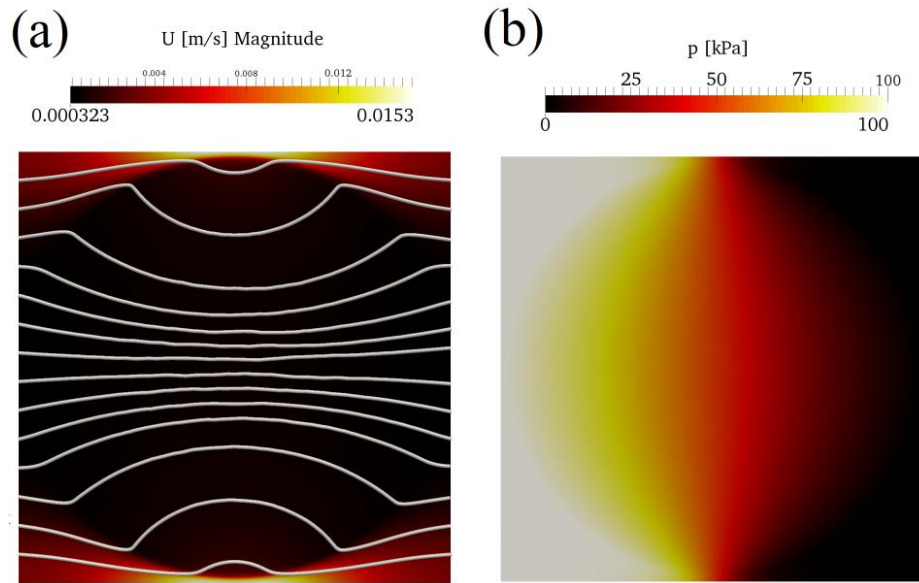
Figure-B.2: Results of the OpenFOAM 2D computations. (a) the velocity field with streamlines originating from the left boundary and (b) the pressure field.

The nature of the flow solution shown in Fig. B.2a and Fig. B.2b allows for considerable simplification of the governing equations using the lubrication theory assumptions discussed in Appendix A. With these simplifications, in the porous region of the flow, the governing equation based on Eq. B.5a above reduces to

$$\frac{\partial p}{\partial x} = -\frac{\mu}{K_{tow}} u_p + \mu \frac{\partial^2 u_p}{\partial y^2} \tag{B.7}$$

where u_p is the x-direction velocity in the porous region. Outside the porous region Eq. B.5a reduces to

$$\frac{\partial p}{\partial x} = \mu \frac{\partial^2 u_f}{\partial y^2} \tag{B.8}$$

where u_f is the x-direction velocity out of the porous region. Due to the problem symmetry, with reference to Fig. B.1a we focus on the half-cell geometry ranging from $y=0$ to $y=L_y$. For the boundary conditions, the normal procedure is to match the tangential components of the velocity and shear stress at the interface. Thus the boundary conditions of the flow domain may be written as

$$\left. \frac{\partial u_p}{\partial y} \right|_{y=0} = 0 \tag{B.9a}$$

$$u_p \big|_{y=g} = u_f \big|_{y=g} \tag{B.9b}$$

130

$$\left.\frac{\partial u_p}{\partial y}\right|_{y=g} = \left.\frac{\partial u_f}{\partial y}\right|_{y=g} \tag{B.9c}$$

$$\left.\frac{\partial u_f}{\partial y}\right|_{y=h+g} = 0 \tag{B.9d}$$

Applying the above boundary conditions set to Eqs. B.7 and B.8 we obtain the velocity profiles for both the porous and the fluid regions

$$u_p = -\frac{1}{\mu}\frac{\partial p}{\partial x}\left[K_{tow} + \frac{h}{c}\frac{e^{cy} + e^{-cy}}{e^{cg} - e^{-cg}}\right] \tag{B.10}$$

$$u_f = -\frac{1}{\mu}\frac{\partial p}{\partial x}\left[-\frac{y^2}{2} + (g+h)y - g\left(\frac{g}{2}+h\right) + K_{tow} + \frac{h}{c}\frac{e^{cy} + e^{-cy}}{e^{cg} - e^{-cg}}\right] \tag{B.11}$$

where c=$K_{tow}^{-0.5}$. Given the velocity field, the flow rate per unit width through any cross-section is calculated as

$$Q = \int_0^g u_p dy + \int_g^{g+h} u_f dy \tag{B.12}$$

This yields the solution

$$Q = -\frac{1}{\mu}f\frac{\partial p}{\partial x} \tag{B.13}$$

where

$$f = \frac{h^3}{3} + K_{tow}\left[g + 2h + ah^2 \coth(ag)\right] \tag{B.14}$$

The pressure drop across the cell is calculated by integrating Eq. B.13 in the x-direction

$$\Delta p = \int_{-Lx}^{Lx} \frac{\mu Q}{f} dx \tag{B.15}$$

To obtain the effective (overall) permeability K_{eff} of the system we use Darcy's law which for the present problem may be written as

$$u_{fp} = \frac{K_{eff}}{\mu}\frac{\Delta p}{2L_x} \tag{B.16}$$

where u_{fp} is the average velocity across the right boundary of the unit cell. We then multiply both sides of Eq. B.16 with the L_y distance

$$u_{fp} \times L_y = \frac{K_{eff}}{\mu}\frac{\Delta p}{2L_x} \times L_y \tag{B.17}$$

The left side of the above equation is simply the flow rate per unit width Q at the cell's right boundary, so that upon rearrangement we obtain

131

$$K_{eff} = \frac{2L_x}{L_y}\frac{\mu Q}{\Delta p} \qquad (B.18)$$

Substituting Eq. B.15 in Eq. B.18 we have

$$K_{eff} = \frac{2L_x}{L_y}\frac{1}{\int_{-Lx}^{Lx}\frac{1}{f}dx} \qquad (B.19)$$

Equation B.19 is a semi-analytical model for predicting the transverse permeability of rectangular unit cell arrays of circular porous fiber tows. It is very simple to evaluate numerically as the function f, which appears in the integral, depends only upon the geometry of the flow domain and the tow permeability.
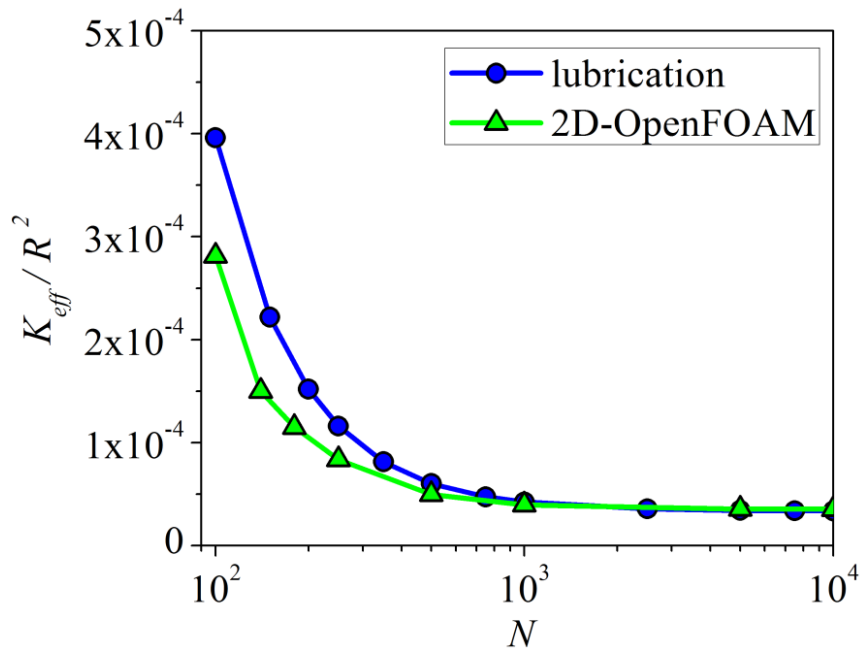

Figure-B.3: Comparison of the OpenFOAM results with the model predictions (Eq. B.19) for the effective permeability K_{eff} scaled with R^2 under different dimensionless geometry sizes N of the unit cell. 2D results obtained for a 8×10^4 cells domain.

Number of cells	K_{eff}/R^2
2.5×10^3	2.784×10^{-4}
2×10^4	2.8062×10^{-4}
8×10^4	2.8133×10^{-4}

Table-B.1. Mesh sensitivity analysis for $N=10^2$.

132

Number of cells	K_{eff}/R^2
2.5×10^3	3.9281×10^{-5}
2×10^4	3.945×10^{-5}
8×10^4	3.9582×10^{-5}

Table-B.2. Mesh sensitivity analysis for $N=10^3$.

We validate the OpenFOAM results with the semi-analytical model (Eq. B.19). The validation is performed in the context of estimating the dimensionless effective permeability K_{eff}/R^2 under different dimensionless sizes N of the unit cell (for specific K_{tow}), where we assume to be given by $N = L_y / \sqrt{K_{tow}}$. We note that the effective permeability K_{eff} from the 2D computations it obtained via Eq. B.18 where we evaluate Q by integrating the computed velocity profile in the x-direction across the right boundary of the 2D computational domain. The results of the comparison are shown in Fig. B.3. We have also performed a mesh sensitivity analysis of the 2D computations for two representative N values. In Table B.1 the mesh sensitivity is shown for $N=10^2$ and in Table B.2 for $N=10^3$.

APPENDIX C

Pin-Assisted Pultrusion: Comparison of 2D simulations with the Darcy modified lubrication approximation

The results obtained with the OpenFOAM 2D simulations for the pin-assisted pultrusion process in Chapters 4 and 5 are compared to a model based on lubrication equation modified with Darcy's law to account the flow in the porous substrate. We note that this modified model is extended to account for the substrate deformation in Chapter 6. With reference to Fig. 4.1, assuming that the permeable porous substrate moves in close proximity to the cylinder (pin) with $\delta_o \ll R$ (here we denote the minimum separation as δ_o), the Reynolds lubrication equation utilized to describe calendering applies also here.

The flow between the porous substrate and the cylinder may be described by Eq. A.1.4 and the continuity equation is given by

$$\frac{\partial u}{\partial x} + \frac{\partial v}{\partial y} = 0 \tag{C.1}$$

where v is the fluid velocity component in the y-direction. The following boundary conditions for the u velocity component are used for the porous/fluid interface and the cylinder surface respectively

$$u[y = 0] = V \tag{C.2a}$$

$$u[y = H(x)] = 0 \tag{C.2b}$$

where V is the pulling speed of the porous substrate and $H(x)$ is given by Eq. A.1.9. For the v velocity component on the cylinder surface we set

$$v(y = h) = 0 \tag{C.3}$$

and on the web/fluid interface we apply Darcy's law which may be written as

$$v(y = 0) = -\frac{K}{\mu}\frac{dp}{dy} = -\frac{K}{\mu}\frac{p_{y=L_f} - p_{y=0}}{L_f} \tag{C.4}$$

where v the penetration velocity, where K the permeability of the porous substrate, $L_f = L_f(x)$ the final penetration depth profile at any position along the x direction in the web, $p_{y=0}$ corresponds to the hydrodynamic pressure at the substrate/fluid interface and $p_{y=Lf}$ is the pressure within the void space of the porous medium right ahead of the penetrating fluid front. In accordance to the 2D computations, we assume that in the porous medium right

134

above the interface a pre-impregnated zone of uniform thickness L_o exists (see Fig. 4.1). The final penetration depth $L_f(x)$ will then be given by

$$L_f(x) = L_o + h_f(x) \qquad (C.5)$$

where $h_f(x)$ is the penetration profile right above the pre-impregnated zone. The contribution of capillary pressure to $p_{y=L}$ may be neglected in light of the much higher hydrodynamic pressure developing in the gap. Under the assumption of lubrication approximation that the hydrodynamic pressure does not vary in the y direction we set $p_{y=0}=p$. Based on the above and by substitution of Eq. C.5 in Eq. C.4 we obtain

$$v(x, y = 0) = \frac{K}{\mu} \frac{p(x)}{L_o + h_f(x)} \qquad (C.6)$$

Integrating Eq. A.1.4 twice using Eq. C.2a and C.2b we obtain the velocity profile

$$u(y) = \frac{1}{2\mu} \frac{dp}{dx}\left(y^2 - yH\right) - V\left(\frac{y}{h} - 1\right) \qquad (C.7)$$

Integrating the above velocity profile from the surface of the cylinder to the porous/fluid interface we obtain the gap flow rate

$$q_x = -\frac{H^3}{12\mu} \frac{dp}{dx} + \frac{VH}{2} \qquad (C.8)$$

By integration of Eq. C.1 across the gap $H(x)$

$$\int_0^{H(x)} \frac{\partial u}{\partial x} dy + \int_0^{H(x)} \frac{\partial v}{\partial y} dy = 0 \qquad (C.9)$$

we obtain

$$\frac{dq_x}{dx} + v(y = H) - v(y = 0) = 0 \qquad (C.10)$$

Substituting Eq. C.3, C.6 and C.8 in Eq. C.10 we obtain

$$\frac{d}{dx}\left(-\frac{H^3}{12\mu}\frac{dp}{dx} + \frac{VH}{2}\right) + \frac{K}{\mu}\frac{p}{L_o + h_f} \qquad (C.11)$$

We note that for $K=0$ (non-permeable substrate) the Reynolds lubrication equation is recovered. Next we write the penetration velocity v at the interface as

$$v = \frac{dL_f}{dt} = \frac{dL_f}{dx}\frac{dx}{dt} = \frac{dL_f}{dx}V \qquad (C.12)$$

so that Eq. C.6 takes the following form upon substitution

$$\frac{dL_f}{dx} = \frac{K}{\mu V}\frac{p(x)}{L_o + h_f(x)} \qquad (C.13)$$

135

Following the boundary conditions described in the Chapter 4, the following boundary conditions apply

$$p(-\infty) = 0, \quad \left.\frac{dp}{dx}\right|_{x=0} = 0 \quad \text{and} \quad L_f(-\infty) = L_o \tag{C.14}$$

We render Eq. C.11 and Eq. C.13 dimensionless using a length scale δ_o, a velocity scale V and pressure scale $\mu V/\delta_o$

$$x' = \frac{x}{\delta_o}, \quad p' = \frac{p\delta_o}{\mu V}, \quad H' = \frac{H}{\delta_o}, \quad K' = \frac{K}{\delta_o{}^2}, \quad L_f' = \frac{L_f}{\delta_o}, \quad L_o' = \frac{L_o}{\delta_o}, \quad h_f' = \frac{h_f}{\delta_o} \tag{C.15}$$

so that

$$\frac{d}{dx'}\left(-\frac{H'^3}{12}\frac{dp'}{dx'} + \frac{H'}{2}\right) + K'\frac{p'}{L_o' + h_f'} \tag{C.16}$$

and

$$\frac{dL_f'}{dx'} = K'\frac{p'}{L_o' + h_f'} \tag{C.17}$$

where the dimensionless gap H' is given by

$$H' = 1 + Ax'^2 \tag{C.18}$$
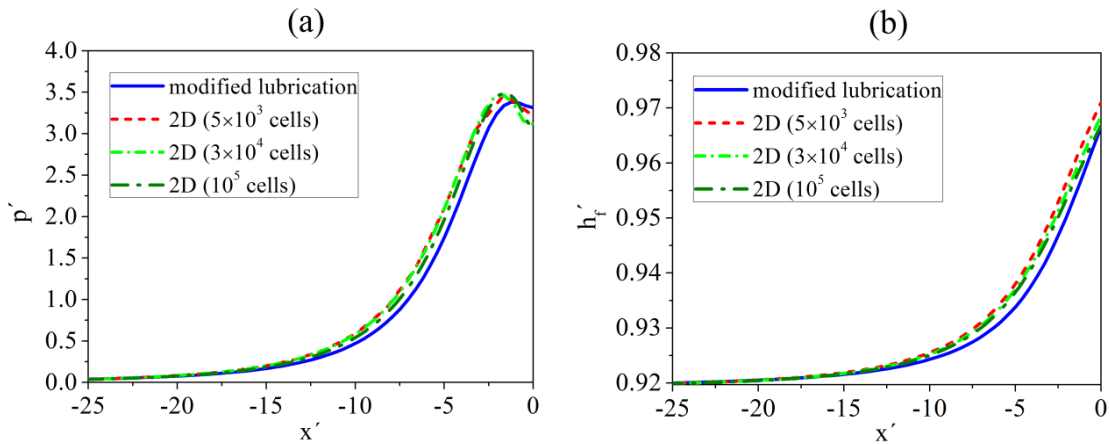
with

$$A = \frac{\delta_o}{2R} \tag{C.19}$$

Figure-C.1: Comparison of the 2D OpenFOAM simulations, for three typical mesh sizes, with the modified Reynolds lubrication equation. (a) dimensionless pressure distribution p' and (b) dimensionless final penetration depth L_f'. Dimensionless parameters: $K'=3.379\times10^{-3}$, $A=5.44\times10^{-2}$ and $L_o'=0.29$.

The boundary conditions in dimensionless form are given by

$$p'(-\infty) = 0, \quad \left.\frac{dp'}{dx'}\right|_{x'=0} = 0 \quad \text{and} \quad L_f'(-\infty) = L_o' \qquad (C.20)$$

We solve numerically the system of Eq. C.16 and Eq. C.17 with the boundary conditions expressed in Eq. C. 20, with Matlab's module bvc4p. The solution gives simultaneously the pressure profile in the gap and the fluid penetration profile.

In Fig. C.1a we compare the pressure distribution $p'(x)$ in the gap calculated via the method described above with the 2D OpenFOAM simulations and in Fig. C.1b the final penetration depth $L_f'(x)$ profile. We choose a set of typical values for the process: $K=10^{-9}$ m^2, $\mu=1000$ Pa·s, $V=0.15$ m/s, $\delta_o=5.44\times10^{-4}$m and $L_o=5\times10^{-4}$m. A mesh sensitivity analysis is also shown with the 2D results being in good agreement with the ones obtained by the modified Reynolds lubrication equation.

Appendix D

Deformable and Non-Permeable Web:
Asymptotic Solution for Small Web Deformation (*Ne*<<1)

We compare the numerical results of a deformable and non-permeable ($\hat{K} = 0$) web presented in Chapter 6 with a closed-form solution which may be obtained to the limit of *Ne*<<1. The comparison is based on evaluation of the dimensionless lift force $\hat{F}$ as a function of *Ne*.

We seek for an asymptotic solution for *Ne*<<1 using a regular perturbation expansion for the pressure and the gap as

$$\hat{p} = \hat{p}_o + Ne \cdot \hat{p}_1 + O(Ne^2) \tag{D.1}$$

$$\hat{h} = \hat{h}_o + Ne \cdot \hat{h}_1 + O(Ne^2) \tag{D.2}$$

where $\hat{p}_o$ and $\hat{h}_o$ are the leading order terms (Reynolds lubrication equation), $O(Ne^2)$ corresponds to the higher order terms and

$$\hat{h}_o = 1 + A\hat{x}^2 \quad \text{and} \quad \hat{h}_1 = \hat{p}_o \tag{D.3}$$

The pressure boundary conditions up to first order expansion are given by

$$\hat{p}_o(-\infty) = \hat{p}_o(\infty) = \hat{p}_1(-\infty) = \hat{p}_1(\infty) = 0 \tag{D.4}$$

To leading order the pressure distribution can be readily calculated from Eq. 6.13 (for $\hat{K} = 0$) to give

$$\hat{p}_o = -\frac{2\hat{x}}{\left(1 + A\hat{x}^2\right)^2} \tag{D.5}$$

Proceeding to the next order upon substitution in Eq. 6.13 we have

$$\frac{d}{d\hat{x}}\left(-\frac{d\hat{p}_1}{d\hat{x}}\hat{h}_o^3 - 3\frac{d\hat{p}_o}{d\hat{x}}\hat{h}_o^2\hat{h}_1 + 6\hat{h}_1\right) = 0 \tag{D.6}$$

which gives

$$\hat{p}_1 = \frac{9 - 15S\hat{x}^2}{5S\left(1 + S\hat{x}^2\right)^5} \tag{D.7}$$

Then upon substitution of $\hat{p}_o$ and $\hat{p}_1$ in Eq. D.1 we obtain a closed-form solution of the pressure profile

$$\hat{p} = -\frac{2\hat{x}}{\left(1+S\hat{x}^2\right)^2} + Ne\left[\frac{9-15S\hat{x}^2}{5S\left(1+S\hat{x}^2\right)^5}\right] \tag{D.8}$$

Upon integration of Eq. D.8 we obtain an exact expression of the dimensionless lift force

$$\hat{F} = \frac{3\pi}{8S^{3/2}}Ne \tag{D.9}$$

or in dimensional form

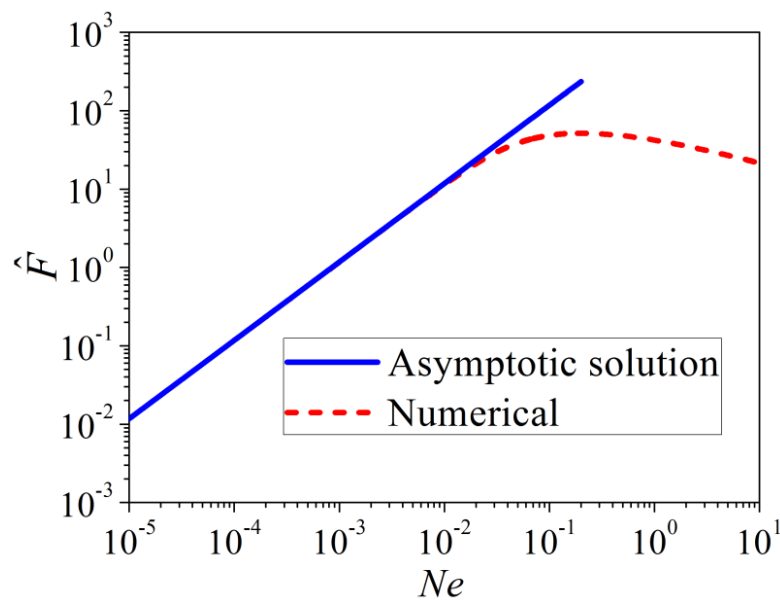$$F = \frac{3\sqrt{2}\pi}{4}\frac{\mu^2 V^2}{E}\frac{R^{3/2}H}{h_o^{7/2}} \tag{D.10}$$

Figure-D.1: Dimensionless lift force $\hat{F}$ as a function of Ne for S=0.01.

We note that the leading order term does not contribute to the lift force due to the antisymmetric form the pressure profile attains (i.e. $\hat{p}_o(-\infty) = -\hat{p}_o(\infty)$). The comparison of the dimensionless force as obtained from the perturbation expansion with the numerical results is shown in Fig. D.1. The numerical solution matches the closed form solution for up to $Ne\approx0.01$.

End of Thesis

139